# Bioinspired materials

Non-covalent modification of nanofibrillated cellulose and chitin via genetically engineered proteins and multilayered graphene

Jani-Markus Malho

VTT

Bioinspired materials

Non-covalent modification of nanofibrillated cellulose and chitin via genetically engineered proteins and multilayered graphene

Jani-Markus Malho

Aalto University School of Science
Department of Applied Physics

Abstract

Biological nanocomposites such as nacre, bone and wood synergistically combine strength, stiffness and toughness with lightweight structure, whereas most man-made engineering materials with higher densities follow the rule-of-mixtures, according to which strength and toughness are mutually exclusive properties. Biomimetic approaches study and mimic nature's concepts and material structures with the aim of developing high-performance bioinspired materials. Recent studies have shown that many of the properties of natural nanocomposites arise from their hierarchical structures from multiple length scales. Molecular level control and design are known to be crucial for the performance of the natural materials especially at the interfaces of the softer matrix and the harder reinforcing elements.

In this work, examples of biopolymer matrices were studied from the mechanical perspective in order to understand how biological components, such as genetically engineered proteins and graphene flakes, could be used to design an organic matrix at the molecular level and to control its macroscopic material properties. The results indicated that the biopolymer networks can be functionalized non-covalently in aqueous and mild conditions directly via self-assembly in order to influence the mechanical properties.

In Publications I and II, genetically engineered fusion proteins, incorporating hydrophobin - double cellulose binding domain or plain double cellulose binding domain, were used to tune the nanofibrillar cellulose network under conditions of controlled humidity.

In Publication III, another genetically engineered fusion protein, chitin binding domain - aspein, was used to modify nanofibrillated chitin matrix through ionic interactions and biomimetic mineralization of calcium carbonate.

In Publication IV, multilayered graphene flakes were exfoliated directly into native nanofibrillated cellulose networks in order to create nanocomposites with improved mechanical properties.

Non-covalent modification of the colloidal biopolymer matrices is an efficient route to construct and study multifunctional nanocomposite materials by engineering the interfaces between the soft and hard phases. Importantly, genetically engineered proteins could pave the way towards new functional components for biomimetic structural nanocomposite materials while Nature's materials continue to provide the constructing principles and inspiration for the development of biomimetic materials.

Tiivistelmä

Luonnon nanokomposiittimateriaalit, kuten helmiäissimpukan kuori, luu ja puu, omaavat synergisiä mekaanisia ominaisuuksia, joissa yhdistyvät jäykkyys, vahvuus ja sitkeys kevyessä rakenteessa. Suurin osa ihmisen tekemistä synteettisistä materiaaleista noudattaa "rule-of-mixtures"-sääntöä, jossa jäykkyys ja sitkeys ovat toisen pois sulkevia ominaisuuksia. Biomimeettiset lähestymistavat tutkivat ja pyrkivät jäljittelemään luonnon luomia konsepteja ja materiaalirakenteita tavoitteena kehittää uusia biomimeettisia ja parempia ominaisuuksia omaavia materiaaleja. Viime vuosien tutkimukset ovat osoittaneet, että monet toivottavat materiaali-ominaisuudet perustuvat useiden eri kokoluokkien yli ulottuviin itsejärjestäytyneisiin hierarkkisiin rakenteisiin. Molekyylirakennetason suunnittelun ja hallinnan tiedetään olevan erityisen tärkeää luonnon nanokomposiittimateriaalien rajapinnoilla, joissa pehmeämpi matriisi yhdistyy jäykempien vahvistavien rakenteiden kanssa.

Tässä työssä tutkittiin, kuinka biopolymeerimatriiseja voidaan suunnitella ja muokata molekyylitasolla käyttäen hyväksi geneettisesti luotuja proteiineja sekä grafeiinihiutaleita. Tavoitteena on makroskooppisten mekaanisten ominaisuuksien molekyylitason hallinta. Tulokset osoittavat, että biopolymeeriverkostoja voidaan funktionalisoida ei-kovalenttisesti miedoissa vesipohjaisissa ympäristöissä mekaanisiin ominaisuuksiin vaikuttaen.

Julkaisuissa I ja II käytettiin geneettisesti luotuja fuusioproteiineja. Fuusioproteiinit muodostuivat joko hydrofobiinista yhdistettynä kaksinkertaiseen selluloosa-sitoutumisdomeeniin tai pelkästä kaksinkertaisesta selluloosasitoutumisdomeenista. Fuusioproteiineilla muokattiin nanofibrilloituja selluloosan verkostoja eri kosteus-tiloissa.

Julkaisussa III muokattiin nanofibrilloitua kitiiniverkostoa ei-kovalenttisesti geneettisesti luodun fuusioproteiinin avulla. Kyseinen proteiini sisälsi kitiinisitoutumis-domeenin ja aspeiinin, joka mahdollisti ionisten vuorovaikutusten hyödyntämisen sekä kalsiumkarbonaatin kiteyttämisen.

Julkaisussa IV kuoritiin monikerroksia grafeiinihiutaleita suoraan nano-fibrilloituun selluloosamatriisiin, josta valmistetuilla nanokomposiittimateriaaleilla oli parannettuja mekaanisia ominaisuuksia.

Ei-kovalenttinen ja kolloidaalinen biopolymeerimatriisien modifiointi on tehokas menetelmä tutkia ja luoda uusia monitoiminnallisia nanokomposiittimateriaaleja muokkaamalla pehmeiden ja vahvistavien rakenteiden rajapintoja. Geneettisesti

muokattuja proteiineja voidaan pitää lupaavina toiminnallisina komponentteina tulevaisuuden biomimeettisiin ja rakenteellisiin materiaaleihin. Luonnon materiaalit ja systeemit tulevat jatkossakin toimimaan inspiraation lähteenä sekä tarjoamaan toimintaperiaatteita uusien biomimeettisten materiaalien luomiseen.

Preface

I never planned to do a doctoral thesis. Yet, I ended up doing one, and got the privilege to work with incredibly talented people. The upsides of this journey are too numerous to list, though it would probably be the understatement of the year to say that things got slightly hectic and chaotic at times. This work was done with the help of several people, whom I want to acknowledge.

Academic dissertation

List of publications

This thesis is based on the following three original publications and one manuscript which are referred to in the text as Publications I–IV. The publications are reproduced with kind permission from the publishers

I   Jani-Markus Malho, Claudine Ouellet-Plamondon, Markus Rüggeberg, Päivi Laaksonen, Olli Ikkala, Ingo Burgert, Markus B. Linder, Enhanced Plastic Deformations of Nanofibrillated Cellulose Film by Adsorbed Moisture and Protein Mediated Interactions, Biomacromolecules, 2015, 16 (1), pp 311–318 DOI: 10.1021/bm501514w

II   Jani-Markus Malho, Suvi Arola, Päivi Laaksonen, Géza R. Szilvay, Olli Ikkala, Markus B. Linder, Modular tuning of the supracolloidal interactions between nanocellulose fibrils with genetically engineered protein binding units, Manuscript, Submitted to Angewandte Chemie International Edition.

III Jani-Markus Malho, Hanna Heinonen, Inkeri Kontro, Ngesa Ezekiel Mushi, Ritva Serimaa, Hans-Peter Hentze, Markus B. Linder, Géza R. Szilvay, Formation of ceramophilic chitin and biohybrid materials enabled by a genetically engineered bifunctional protein, Chemical Communication 2014, 50 (55), 7348–7351, DOI: 10.1039/C4CC02170C

IV Jani-Markus Malho, Päivi Laaksonen, Andreas Walther, Olli Ikkala, Markus Linder, Facile Method for Stiff, Tough, and Strong Nanocomposites by Direct Exfoliation of Multilayered Graphene into Native Nanocellulose Matrix, Biomacromolecules 2012, 13 (4), pp 1093–1099 DOI: 10.1021/bm2018189

Author's contributions

Publication I:
The author prepared all of the samples for the measurements. The protein was engineered by Professor Markus Linder, produced by Michael Bailey and purified by Riitta Suihkonen. The NFC nanofibres were produced by Panu Lahtinen. The author planned all the experiments and conducted all mechanical tensile measurements and cryo-TEM imaging. The FT-IR, sorption and TGA measurements were conducted by Claudiane Ouellet-Plamondon. All the measurements were performed at the ETHZ lab of Professor Ingo Burgert with the exception of cryo-TEM imaging which was performed at the Nanomicroscopy Centre of Aalto University. The author interpreted the results, wrote the first version of the article and finalized the article together with the co-authors.

Publication II:
The author planned and conducted all the experiments. All of the samples for the experiments were prepared by the author. The NFC nanofibres were produced by Panu Lahtinen. The proteins were engineered by Suvi Arola, produced by Michael Bailey and purified by Riitta Suihkonen. The author interpreted the results, wrote the first version of the article and finished the article together with the co-authors.

Publication III:
The author planned all the experiments, interpreted the results, wrote the first version of the article and completed the article together with the co-authors. The author carried out all the mechanical tensile measurements, SEM-EDX and cryo-TEM imaging. In addition, the author prepared the samples for the ionically modified freestanding films and for the mechanical tensile measurements, SEM-EDX and cryo-TEM. The author also took part also in the biomineralization synthesis, which was coordinated by Hanna Heinonen. The protein and its binding isotherm were designed and performed by Geza Szilvay, the protein was produced by Riitta Suihkonen and the WAXS measurements were performed by Inkeri Kontro. The nanofibrillated chitin was produced and provided by Ngesa Ezekiel.

Publication IV:
The author planned all the experiments, interpreted the results, wrote the first version of the article and finished the article together with co-authors. The author

prepared all the samples and performed all the experiments with the exception of the Raman spectroscopy, which was performed by Päivi Laaksonen. The NFC nanofibres were provided by Panu Lahtinen.

Contents

1. Introduction

Nature has inspired scientists over many decades to develop novel (bio)synthetic materials via biomimetic approaches to the study of natural systems and materials [1]. Importantly, the biomimetic studies have revealed many crucial roles that biopolymers and proteins fulfil in matrices of hierarchically structured biological materials [1, 2]. One of the main motivations for biomimetics in materials science has been the urge to find sustainable replacements for environmentally unsustainable synthetic materials such as many plastics. Thus, efforts to apply biological building blocks via bioinspired concepts have gained much attention. The development of bioinspired materials has encountered many problems in mimicking the structures and functions of natural materials. One major problem has been utilization of the full potential of biopolymers. Poor success in utilizing biological molecules may result from approaches that include structural modifications of the source materials, which are considerably more sensitive to harsh (chemical) processing conditions than many synthetic materials. There is still a significant lack of understanding concerning the properties of the biological building blocks. Many biological materials, such as biopolymers and proteins, are usually isolated and produced in aqueous environment (their native environment), which often means that they are poorly soluble in non-polar and organic solvents causing problems in many conventional processing methods. Therefore, their direct exploitation in aqueous media is desirable. In addition, industrial applications prefer aqueous processing media to reduce the amount of waste streams, the number of processing steps and the overall costs.

Biological materials possess often renewable, non-toxic and sustainable characteristics, which can be considered essential for future applications. The exploitation of renewable materials has grown within recent decades into a promising field, especially for biopolymers such as cellulose [3]. There are number of reasons to utilize biological materials, one of the most important being their lightweight character in combination with excellent mechanical properties. Low density can provide a platform for energy efficiency in e.g. transportation applications. However, most of the industrially established man-made (biomimetic) materials are still based mainly on synthetic source materials that are non-renewable.

The rise of nanotechnology has furthered the trend in materials science towards nano and molecular level studies. Nano and molecular level understanding should ideally allow control of material properties from the smallest length scales up to macroscopic scales, eventually resulting in material properties that can exceed even the properties of current man-made synthetic materials, and even Nature's materials. On another note, progress in (nano)technological equipment and methods has only recently allowed scientists to study natural systems at their lowest structural and hierarchical levels, thus enabling exploitation of Nature's construction principles in the smallest scales [4].

1.1   Natural nanocomposites

Scientifically the motivation to use biological components is based on the structure-property relationships of biological materials that are constructed via self-assembly in mild aqueous conditions [1, 5]. Most of the natural composite materials are nanocomposites, the definition of which requires that one of the phases must have at least one (often more) dimension that is less than 100 nm [6]. The basic idea to construct nanocomposites is to combine two (or more) structural elements together to take advantage of (both of) the elements and preferably to generate properties that neither of the elements possess alone [7]. Most of the man-made engineering materials (>98%) fit to a so-called banana curve, where strength and robustness are mutually exclusive properties [8, 9] and the materials follow the rule-of-mixtures [10]. In rule-of-mixtures composites the properties depend on the amount of reinforcing particles. When the amount of such particles is increased the composite material becomes stiffer, but also more brittle, which is a common trade-off for composite materials. The ultimately desired combination of stiffness and toughness is found only in very few types of man-made materials (>2%), whereas many biological materials possess high stiffness in combination with toughness, thus demonstrating that material structures can provide a basis for performance that is beyond the rule-of-mixtures composites [8, 11]. Figure 1 displays a material properties chart, in which biological nanocomposite materials such as bone, enamel and mollusc shell are visualized in relation to the properties of their building blocks.
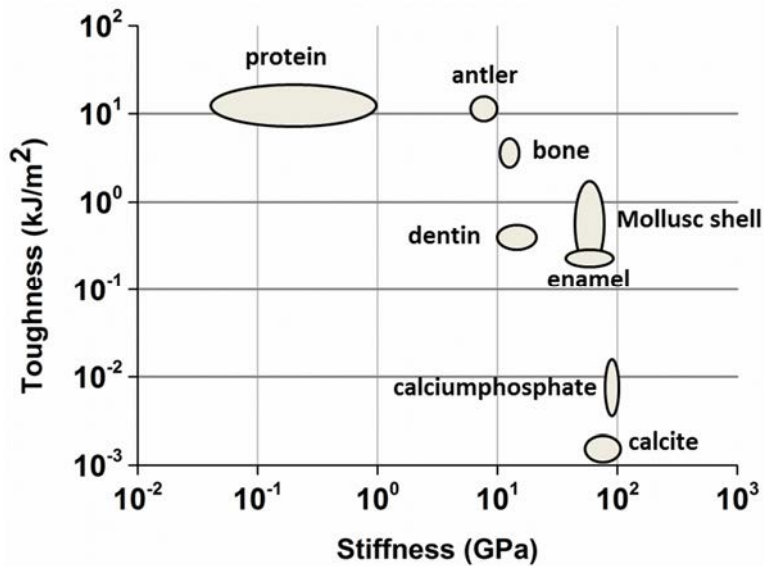
Figure 1. A material properties chart for biological materials, in which toughness is shown as a function of stiffness. The chart exhibits how biological composite materials such as bone, enamel, dentin, antler and mollusc shell combine high toughness (robustness) with high stiffness. The properties arise from hierarchical structures that have evolved naturally over millions of years. The chart is adapted from Fratzl et al. [12] with permission from the Centre National de la Recherche Scientifique (CNRS) and The Royal Society of Chemistry.

Natural nanocomposite materials are based on hierarchical structures, in which separate building blocks work cohesively over several length scales [1]. Interestingly, weak but relatively tough components are tailored together with stiff and brittle components to create multifunctional nanocomposite materials with synergistic properties [1, 12, 13]. The biological nanocomposite materials can be divided into two classes: mineralized and non-mineralized [14]. The mineralized materials rely on ceramics for stiffness and compressive strength, whereas the organic components provide a basis for the toughness [14]. The non-mineralized materials gain their stiffness and strength from fibrous and often semi-crystalline biopolymers, while softer polymers and/or proteins function as a "glue" between the reinforcing fibres [2, 14]. Wood and plant cell walls are examples of non-mineralized biological nanocomposite materials, in which the strength and stiffness are derived from the semi-crystalline cellulose nanofibres while hemicellulose and lignin form the continuous soft phase that glues the cellulose nanofibres together, laying the grounds for the mechanical performance of the plant cell wall [2, 15]. Obviously the cell wall (and other natural nanocomposite materials) has several other functions in addition to the mechanical properties, such as transfer of nutrients and water to the intracellular structures making them

multifunctional. Mineralized biological nanocomposite materials such as nacre [16] and bone [17] are prime examples of natural materials that combine minerals with softer fibrous biopolymers and proteins in order to provide mechanical strength. Mollusc shells have several levels of hierarchy in their structures, in which the macroscopic shell itself is constructed from two separate layers: the outer layer is a prismatic calcite and the inner layer is the nacre [16, 18]. Mother-of-pearl and its inner nacreous layer is one of the most mimicked natural nanocomposite materials due to its mechanical properties, which are based on multiple hierarchical structures and functions [19-22]. Thus, we will explore next the nacreous layer in more detail in order to elucidate its structure-property relationships.

1.2   Nacre

Nacre represents a near-perfect marriage of brittle but stiff $CaCO_3$ platelets and a soft but tough organic phase of chitin nanofibres and proteins, which results in a stiff, tough and strong nanocomposite material [5]. The elastic modulus of nacre is around 50–70 GPa and the tensile strength circa 130–170 MPa both depending on the state of hydration [5]. Importantly, the mineralized nanocomposite material of nacre exhibits over 3000-fold higher toughness than that of mineral platelets, with only slightly reduced stiffness [5], which is considered to result from extremely well naturally engineered/evolved interfaces between the soft and reinforcing phase and hence from their effective interplay [4]. A photograph of natural nacre and an SEM image of a cross-section of a nacre fracture surface are displayed in Figures 2a and b, respectively. The mechanical properties of nacre have evoked much discussion concerning structure-property relationships, especially regarding the high toughness that is attained with such a small amount of organic phase (around 5% of the whole mass). The $CaCO_3$ minerals that constitute 95% of the nacre are expected to carry the load due to the higher stiffness of the reinforcing platelets in relation to the organic matrix, whereas the toughness is believed to be based on the cohesive interplay of organic matrix components and the mineral platelets [4].

1.3   Toughening mechanisms in nacre

Nacre has been shown to possess several different toughening and crack deflecting mechanisms [5]. The cohesive interactions of the components in the organic phase and adhesion to the $CaCO_3$ platelets via multifunctional proteins have been suggested to provide the basis for the controlled crack growth, energy dissipation and homogenous stress transfer across the mineral platelets in nacre [4, 23]. The organic framework has been shown to behave viscoelastically under hydration, mediating the stress transfer among the mineral platelets and thus to generate toughness while chitin nanofibres provide the structural integrity of the organic matrix [24, 25]. Hidden length scales and sacrificial bonds have also been proposed to exist in the organic matrix of nacre and to contribute to its toughness

[4, 26]. Sacrificial bonds are weak interactions, such as hydrogen bonds and salt bridges, that can be formed within the structures of a single molecule (e.g. proteins) or between different molecules [27]. The sacrificial bonds can create loops within a single or multiple molecule structures, thus providing hidden length scales [27]. The sacrificial bonds are broken during e.g. tensile tension with some energy consumption, after which the loops are straightened, consuming significantly more energy than the breaking of the sacrificial bonds [28]. These loops are called hidden length scales, because they are concealed within the structures by the sacrificial bonds. The hidden length scales become effective only when the material is strained and deformations take place within the structures. The organic framework is known to be continuous throughout the mineralized structures of nacre and therefore to be one (if not the main) of the key components for the high toughness of nacre [29, 30]. In addition to the above-mentioned toughening mechanisms, mineral bridges (physical connections), nanoasperities on the $CaCO_3$ platelets and the waviness of the mineral platelets are known to have major effects on the strength and toughness of the nacre by affecting the platelet pull-out mechanism with increased friction and mechanical interlocking [30-35]. Some studies have questioned the relevance of the organic matrix in the mechanical properties by suggesting that the organic matrix might mainly be a scaffold for the construction of the hierarchical structures and that the physical connections (the mineral bridges) could account for the high toughness of nacre [36]. However, the effect of induced friction from the mechanical interlocking of platelets is known to be dependent on the "gluing components" of the organic matrix, which keep the reinforcing blocks in close proximity [27].

Figures 2c and d illustrate the basic idea of combining stiff and strong reinforcing components with a soft (and tough) phase in natural nanocomposites. In addition to nacre, many other biological materials such as bone [12] and wood cell wall [2] are known to derive their toughness from the interplay between the reinforcing phase and the soft phase through the adhesive model illustrated in Figures 2c and d. The model suggests that efficient adhesion between the reinforcing particles (mineral platelets, fibres or mineralized fibres) is mandatory for the mechanical performance (namely for high toughness), whether it is attained via the continuous organic phase or through physical connections such as mineral bridges in nacre. The model serves as an inspiration for the designing of the biomimetic materials described in this thesis.
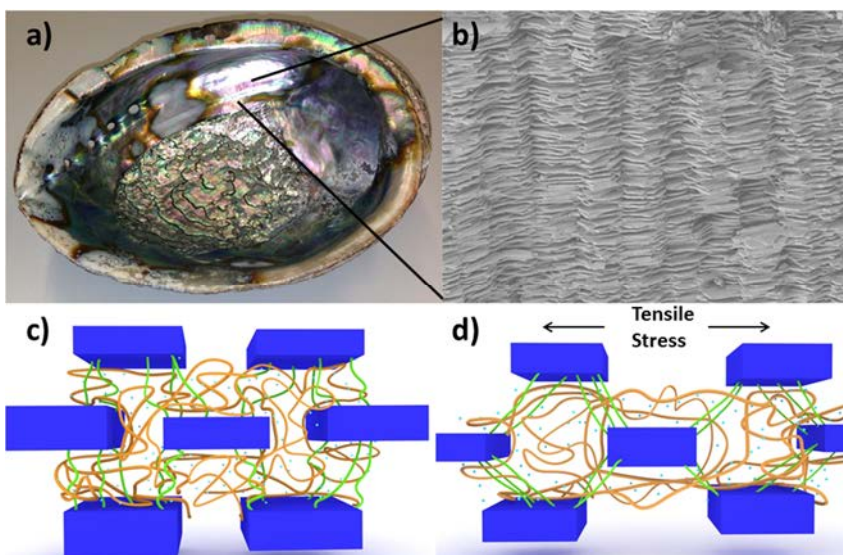
Figure 2. Simplified scheme of the structure of the nacreous layer of mollusc shell. a) Image of a natural nacre. b) SEM image of a cross-section of natural nacre showing the brick-and-mortar type of structure. c) Schematic illustration of the organic matrix (green and orange components) connecting the reinforcing phase (blue components) in relaxed state. The blue reinforcing particles are drawn as platelets in this image but (nano)fibres are utilized as reinforcing components in several natural nanocomposites. d) Illustration of a tensile stress induced behaviour within the nanocomposite structure. The mechanical behaviour of many biological nanocomposites (nacre, bone, wood) is based on the interplay between soft and hard phases, where the hard reinforcing particles need to be properly connected with cohesive interactions. The reinforcing components can be connected via the organic matrix (as in bone [12], wood [2] and nacre [5]) and/or directly like in nacre through mineral bridges [36]. The green particles illustrate the adhesive connections that transfer the stress directly between reinforcing components and via the organic matrix (orange and green components). The light blue spheres represent randomly placed water molecules within the matrix. The amounts, sizes and shapes of different phases are simplified and not drawn to scale.

1.4   Non-covalent interfaces

Most biological materials (mineralized and non-mineralized) are based on organic matrices, which control the materials construction and provide functionalities to the interfaces between different phases [1]. The realization of the importance of molecular level control at the interfaces of soft and hard phases has resulted in attention being directed more and more towards interfaces rather than attempting to find the ultimate building blocks [37]. The interfaces have been shown to control many structure-function relationships in many biological materials and thus to

affect their overall properties [27, 38]. Chemical modification is a conventional route to engineer material interfaces, although nature uses mostly proteins and other non-covalent interactions to tailor material interfaces [39]. Thus, non-covalent modification can be considered as an attractive approach. Another important reason to exploit non-covalent interactions is that they enable preservation of the original structures of the source materials and hence presumably their natural properties. However, non-covalent interactions can provide challenges when systems are crucially dependent on them. One of the major problems is the weak character of non-covalent binding, which is susceptible to interference by water molecules or other impurities and it can be outcompeted completely. Many methods of preventing hydration-induced softening are based on the introduction of covalent bonds via crosslinking agents, wherein the domination of weak interactions such as hydrogen bonds, as in the native NFC matrix, can be overridden with the introduction of stronger bonds. However, several drawbacks arise from covalent bonds that are superior in strength to the non-covalent weak interactions. Covalent bonds limit and reduce the ductility, making materials often more brittle and more susceptible to crack growth, which is highly undesirable from the mechanical perspective, although covalent bonds can provide enhancements in the elastic properties by stiffening the material. To avoid brittleness, reversible non-covalent interactions are sought. Evolution has overcome the problem of weak interactions by creation of specific binding domains (among other solutions) that work as adhesives in multifunctional proteins in natural systems. In addition to the production of biological adhesives, all biological modification and synthesis is carried out in mild and aqueous conditions, thus emphasizing the importance of the processing conditions as well as the nature of the interactions [4]. Consequently, understanding and mimicking of the interfaces and the synthesizing conditions of biological materials are considered to be of crucial importance in biomimetics [40].

1.5   Multifunctional proteins in nacre

Interfaces in natural materials are often controlled by weak interactions, which are mediated mostly by multifunctional proteins in biopolymer networks [41]. The multifunctionality in proteins is often derived from modular structures [42], in which different functional motifs can operate simultaneously or separately. Several studies have revealed some extremely intricate proteins that appear to play a role at the interfaces of biological materials by completing different tasks [43, 44]. Initially multifunctional proteins may affect many complex self-assembly-based construction processes and later on the performance of the complete structures [27, 41]. Aspein is one of the most acidic naturally occurring proteins and it was first found in pearl oyster [45]. Later, aspein has been connected to $CaCO_3$ biomineralization in the formation of prismatic calcite layer [46], while another protein called Lustrin A has been shown to take part in $CaCO_3$ mineralization in the nacreous layer of nacre [42]. Another multifunctional and acidic protein called

PIF was also found in the nacreous layer of mollusc shell, where at least two specific binding domains (BD or BM as binding module) were identified among other presumably functional amino acid motifs [47]. The roles of the binding domains are not fully understood, but their functions include affinities to specific substrates. For example, in PIF one of the binding domains is a chitin binding domain (ChBD) that adheres to chitinous substrates and the other is an aragonite binding domain, which has an affinity to aragonite crystals [47] (and possibly also to other forms of calcium carbonate). Moreover, in nacre the multifunctional proteins (mostly within the other organic framework) are believed to promote biomineralization by controlling the construction of the material and possibly by conferring cohesion between the reinforcing minerals ($CaCO_3$) and chitin nanofibres within the organic framework, hence influencing the mechanical properties of nacre [13, 42, 48].

1.6   Carbohydrate binding domains

Binding domains are generally found in many different systems in nature, where they presumably perform several different tasks that are often based on self-assembly [49]. The binding domains have an ability to bind materials non-covalently and thus often reversibly [50]. Recent studies have been able to visualize the movement of proteins that contain both carbohydrate binding domain and catalytic domain, which are natively connected in series in many enzymes [51, 52]. The character of binding domains has been studied with several enzymes, in which the catalytic domains degrade (natively) biopolymers after the binding domains have brought the multifunctional protein into proximity of the degradable biopolymer [49, 53]. Importantly, binding domains work in an aqueous environment and demonstrate an ability to outcompete hydrogen bonding of the water molecules via the binding domains, making them interesting candidates for nanotechnological applications, in which hydration and the overall effect of water can be of great concern. The reason for their ability to outcompete hydrogen bonding of water molecules may lie in their explicit structures, which allow multiple site binding onto surfaces [54]. The behaviour of different binding domains is rather complex and the binding itself is not completely understood, although their structures are known and some studies have shown that the aromatic amino acids have a crucial role in the binding function [55]. Figure 3a and b display structural representations of a cellulose binding domain (CBD) and a chitin binding domain (ChBD), respectively. Binding domains represent a category of proteins that perform important tasks, many of them still unknown [50]. However, in this thesis we will focus exclusively on exploiting the binding function of different carbohydrate binding domains.
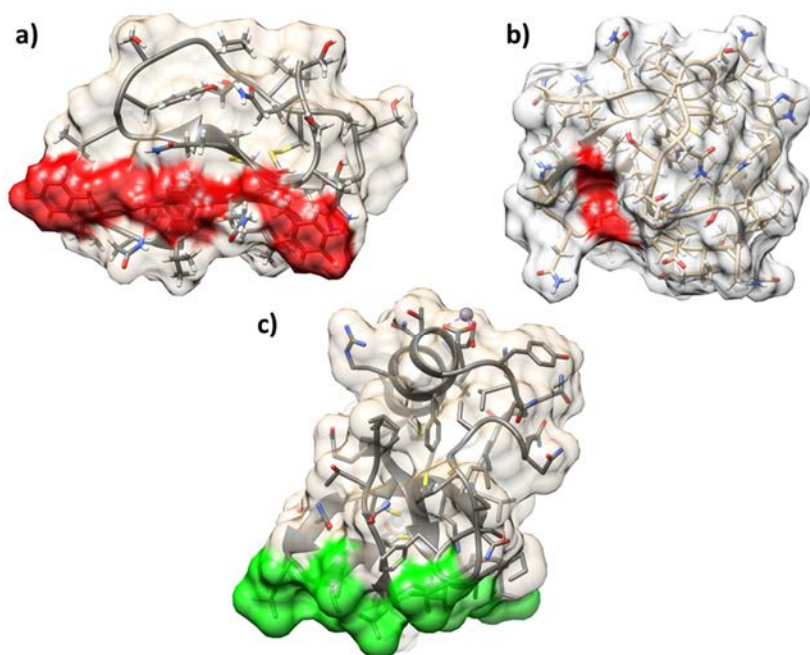
Figure 3. Schematic presentation of a) cellulose binding domain (CBD), b) chitin binding domain (ChBD) and c) a class two hydrophobin (HFBI). The molecules are not drawn to scale. The expected binding sites of the CBD and the ChBD are highlighted with red, while the hydrophobic site of HFBI is shown with green colour.

1.7 Class II hydrophobin HFBI

Another interesting protein with a very different set of properties is the class II hydrophobin HFBI [56]. The molecular structure of HFBI is exhibited in Figure 3c. HFBI has presumably several tasks in its native environment (like many proteins), one of them being lowering of the surface tension at air-water interfaces to allow a certain fungus (*Trichoderma reesei*) to grow out from water [57]. *T. reesei* secretes HFBI molecules into the surrounding aqueous medium, where the molecules self-assemble to the air-water interface due to their amphiphilic character [57]. Recent studies have also shown that the HFBI multimerizes in aqueous media to form dimers and tetramers, and also that it self-assembles on different (hydrophobic) surfaces in aqueous environment, making it an interesting candidate for scientists to exploit in novel systems [58, 59]. Consequently, naturally occurring proteins with and without modular structure can possess several different functions making them promising candidates for future applications but also more difficult to fully understand.

1.8 Genetic engineering

Nature provides a wide variety of multifunctional proteins and utilizes them in very precise and effective ways [13, 44]. In order to exploit functional domains such as CBD, ChBD and HFBI, the means to tailor them are needed. Genetic engineering allows the design and development of novel proteins with tailored structures and functionalities [44]. Hence, different protein domains that are found in nature can be genetically tailored together to add more complexity into a single recombinant protein with multi-domain structure. Genetic engineering provides scientists with extensive possibilities to design recombinant proteins. However, large scale production can generate bottleneck especially for industrial applications.

1.9 Carbohydrate biopolymers

Proteins control interfaces and consequently they form the structural and functional basis for many natural materials together with biopolymers and other reinforcing components [44]. Carbohydrate biopolymers are another interesting class of renewable and sustainable materials, of which the most abundant biopolymers are cellulose and chitin. Both of them have attracted wide attention due to their excellent mechanical properties in combination with their low density [3, 60].

1.10 Nanofibrillated cellulose

Cellulose is a semi crystalline homopolymer that is constructed from repeating units of β-(1-4)-D-glucopyranose [3]. The glucose molecules pack together to form cellulose nanofibres that contain both crystalline and amorphous regions [3]. Crystalline regions refer to ordered regions and amorphous regions to disordered non-crystalline regions. The cellulose nanofibres are glued together with lignin and hemicellulose to form macro sized cellulose fibres [3]. Cellulose is found in different polymorphs in nature, where cellulose-Iα and -Iβ are the most commonly appearing forms. Cellulose can be found in e.g. wood and plant cell walls, where the stiff and strong cellulose fibres function as the reinforcing molecules providing the cell wall with its structural integrity and mechanical properties [2].

The rise of nanotechnology generated a need for more homogenous and smaller sized cellulose (nano)fibres, which led to the development of a new set of methods that resulted in production and isolation of nanofibrillated cellulose (NFC, nanocellulose; CNF, cellulose nanofibres or MFC, microfibrillated cellulose) in aqueous dispersion, in which lignin is removed and the cellulose nanofibres are separated from each other (to some extent) [61-63]. NFC nanofibres are typically 5-20 nm in width and several micrometres in length, and thus they have a relatively high aspect ratio and surface area [3]. Importantly, they are known to have an elastic modulus of around 140 GPa and are expected to have a tensile strength within a few GPa [64-66], although the reported absolute values vary and

depend on the study and the measurement method. The long NFC nanofibres form natively a percolating network in aqueous environment, which makes them an attractive source material especially for structural purposes for biomimetic materials and nanocomposites [3].

1.11 Nanofibrillated chitin

Chitin is a close relative to cellulose. Yet, it has received less attention, partly because of its lower mechanical properties in comparison to cellulose [67]. Chitin is also a semi-crystalline biopolymer and an analogue to cellulose, being a poly (β-(1,4)-N-acetyl-D-glucosamine that exists in different polymorphic forms [68]. α-Chitin is the most abundantly occurring polymorph of chitin [69] and is found e.g. in the shells of crabs and prawns [70], whereas β-chitin is found in nacre [43]. Methods have been developed to disintegrate chitin nanofibres from many biological sources to provide more suitable sized biopolymer fibres for (nano)technological applications with high aspect ratio and surface area [67, 71]. The preparation of chitin nanofibres often causes some deacetylation [72]. Depending on the amount of deacetylation chitin can be called chitosan, which is the N-deacetylated derivative of chitin [72]. The elastic modulus of chitin nanofibres has been measured to be within the range of 40-60 GPa depending on the method and study [73, 74], whereas the tensile strength of chitin is still unknown. Figure 4 exhibits cryo-transmission electron microscopy (cryo-TEM) images of vitrified aqueous dispersions of nanofibrillated cellulose (a) and nanofibrillated chitin (b).
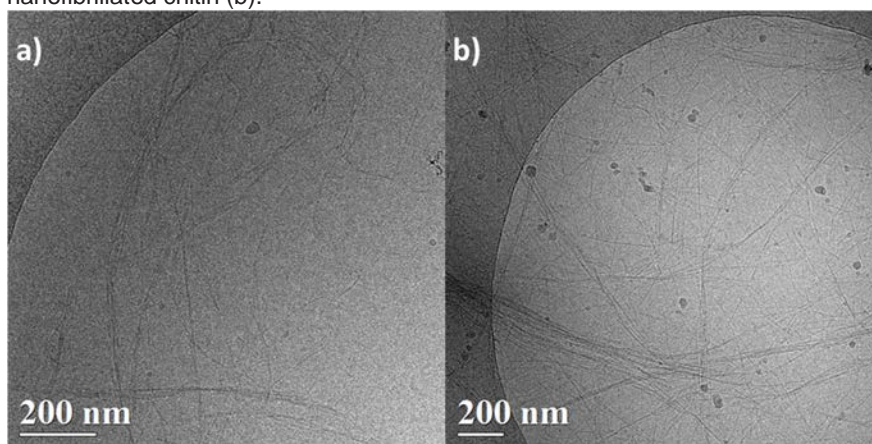
Figure 4. Cryo-TEM micrographs from vitrified aqueous dispersions of unmodified native a) NFC and b) chitin nanofibres. Both of the biopolymers can be dispersed into aqueous media, although they can also aggregate as can be seen (qualitatively) in the images. In general, the native NFC nanofibres are more dispersable in aqueous media than the chitin nanofibres.

1.12 Fibrous biopolymer matrices

Chitin and cellulose have many notable properties in addition to their mechanical properties, but this thesis focuses solely on exploiting their role as structural matrix components in biomimetic nanocomposite materials. The role of the biopolymer may be in reinforcing or in the soft phase of a natural composite material. In addition to the high mechanical properties of biopolymer nanofibres, flaw tolerance has been suggested to be significantly higher for nanoscale building blocks, which can be considered as a huge advantage for many applications [38]. Chitin and cellulose are part of hierarchical structures in biological nanocomposite materials, in which all components probably have an important role in mechanical properties as well as in other functions [1]. For example, NFC is known to be the reinforcing part of wood and plant cell walls [15], whereas the chitin nanofibres work with proteins in the stress transfer and energy-dissipating matrix of the shells of crustaceans and bivalves, where the mineral platelets form the stiff reinforcing phase [1, 16]. This categorization is far from universal, but these two examples demonstrate Nature's versatility in utilizing two biopolymers that differ only slightly in structure for very different tasks. The nature and behaviour of these fibrous biopolymers is not yet fully understood, which makes their effective exploitation difficult.

In this work the fibrous biopolymers often dominate the behaviour of the materials since they function as the major component that is modified by additional molecules. When the excess amount of water or solvent is extracted from fibrous semi-crystalline biopolymer dispersion the entangled nanofibres are jammed in a state that resembles colloidal glasses [75]. Rubber elasticity theory has been used for the designing of biopolymers in the past, but it does not fit the long entangled fibrous materials, which are unable to relax under tension due to the entanglements, and thus the interpretation of mechanical behaviour deviates for the biopolymers [76]. The long entangled biopolymers are visualized schematically in Figure 5. In addition to the length and amorphous regions of the long nanofibres, chitin and cellulose have several hydroxyl groups on their surface, which makes them sensitive to the surrounding moisture. Importantly, the role of water in applications can rarely be completely excluded making it one of the main parameters to be followed, because it can significantly affect nanocomposite properties [77, 78]. Water is visualized as randomly placed light blue spheres in Figure 5. Consequently, the water and the inter-fibre interactions provide a basis for the percolating biopolymer matrices.
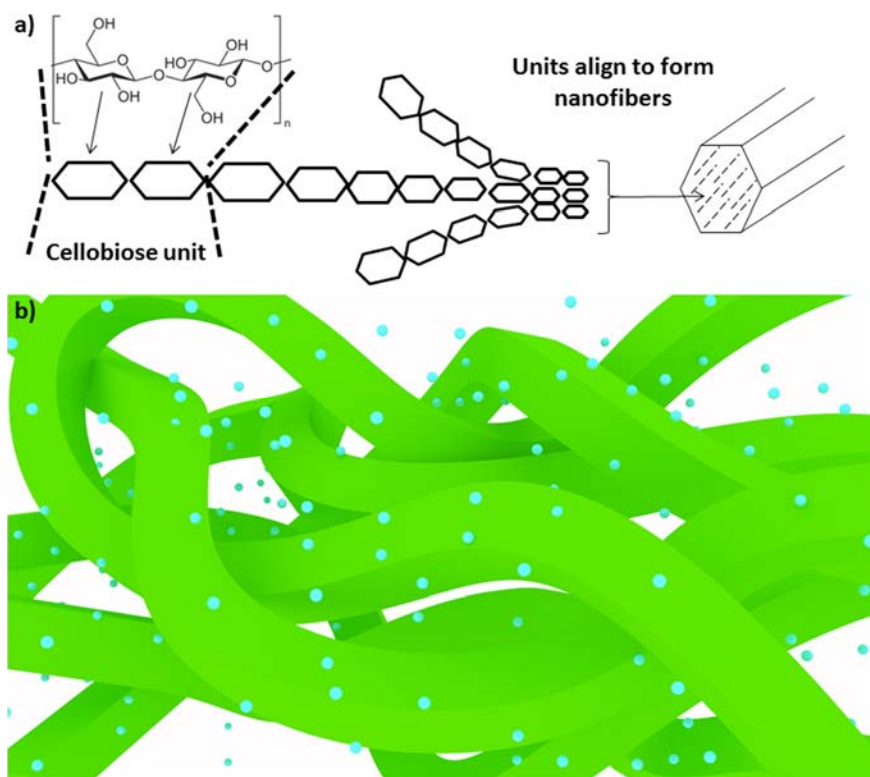
Figure 5. Cellulose nanofibres. a) Cellulose backbone structure and schematic illustration of how cellobiose building blocks assemble to form cellulose nanofibres. b) Schematic illustration of long biopolymer nanofibres consisting of crystalline and amorphous regions. The nanofibres entangle in aqueous environment due their nature, aspect ratio and the hydroxyl groups. The amorphous regions provide freedom for the long biopolymers to bend and entangle.

1.13 Biopolymer based applications

Much work has been carried out in recent years to develop NFC- and chitin-based biomimetic hybrid and nanocomposite materials [60, 64], although chitin has been less utilized mainly due to its poorer mechanical properties in comparison to NFC [79]. However, chitin has many other properties that make it an attractive source material for a wide range of applications, e.g. for biomedical applications such as wound dressing [60]. Many recent nanocellulose-based biomimetic studies handle TEMPO-oxidized NFC, in which the NFC has been chemically modified to generate charges on the NFC nanofibre surfaces [80, 81]. A similar possibility exists with chitin, in which the charged deacetylated form of chitin, chitosan, has been applied more often in various applications than the native chitin nanofibres

[79]. The charged forms of NFC and chitin are often used because of the enhanced dispersity of the nanofibres, which is known to be crucial for reliable sample preparation and improved properties. However, other factors are known to affect the dispersity and stability of NFC nanofibres such as the hemicellulose content, which can comprise over 25% of the total biopolymer mass depending on the source and processing history of the NFC [82]. Some fundamental studies on NFC nanopapers have been carried out to investigate the effect of the degree of polymerization (DP) [83], porosity [84] and the orientation of the nanofibres by cold drawing [85]. In these experiments, the longer chains exhibit somewhat higher strength and toughness, while the orientation has a more complex effect, enhancing the elastic modulus at the cost of reduced strain-to-failure and toughness [83, 85]. Many of fundamental studies can be considered highly useful for the future designing of NFC-based materials, even though they may not always result in improved material properties. Biomimetics has also led to various combinations of cellulose and clay platelets with relatively high mechanical, fire shielding and gas barrier properties [86-88]. In general, the NFC nanocomposite field has been highly active with promising results [3, 64]. Nevertheless, the studies are often focused on developing the elastic properties and the ultimate tensile strength of the materials, whereas only a few studies have explored new ways to improve the energy dissipation and crack growth control during the plastic deformation and thus to enhance the toughness [89-91].

The studies discussed above did not include proteins in structural biopolymer-based materials, which represent a rather new field in structural nanocomposites materials. However, novel biosynthetic nanocomposites with genetically engineered proteins have been developed. A significant precursor for the work carried out in this thesis treated NFC nanofibres, fusion proteins and graphene flakes in order to develop a nacre mimetic material [92]. The work was preceded by a study, in which the recombinant protein was developed via genetic engineering by connecting cellulose binding domains with hydrophobin [93]. The bifunctional protein had two CBDs in tandem (double cellulose binding domain, DCBD) to enhance the binding affinity on cellulosic materials in comparison to a single CBD [94]. The fusion protein was first utilized in exfoliation of graphene [95] before the nacre mimetic composite was developed. Laaksonen et al. used the HFBI domain to self-assemble on graphene flakes [92] as they are highly hydrophobic and do not disperse in aqueous media without chemical modification or surfactants. The protein functioned as a molecular glue binding the reinforcing and extremely stiff graphene flakes together with the strong and flexible NFC nanofibres that provided the continuous organic framework for the nanocomposite together with the fusion protein [92]. Although NFC is known to possess a remarkable combination of stiffness and lightweight character as discussed above, its role in the study was to act as the continuous and energy-dissipating/transferring matrix while graphene flakes would carry the load. The results demonstrated nacre-like properties, where stiffness did not reach the level of natural nacre but the nacre-mimetic nanocomposite displayed significantly higher toughness and relatively high ultimate tensile strength [92]. The work

demonstrated how the model of soft gluing matrix [96] can be utilized to design biomimetic nanocomposites through molecular engineering using sustainable source materials and non-covalent interactions.

2. Aims of this work

This work focused on understanding and designing biomimetic nanocomposite materials from biopolymer matrices. The nanocomposite materials were studied by experimental methods. The essential question for all the studies was to ascertain what can be learned from biopolymer matrices through macroscopic (mechanical) properties via molecular and nano-level engineering and designing. In this thesis the development of the material structures was based on non-covalent and biological interactions and thus on self-assembly. The nanocomposite materials were constructed in mild and aqueous conditions, thus bringing the constructing principles closer to nature's own design principles. Genetically engineered proteins were designed on the molecular level, and both functional and non-functional parts were tailored, depending on the study, in order to modify the interactions within the nanocomposites.

Many structure-property relationships and construction principles of natural materials remain unresolved to date. Thus, the understanding of biopolymer matrices as structural and functional matrices will aid the designing and construction of novel multifunctional materials. This work aimed ultimately to create new multifunctional nanocomposite materials using bioinspired approaches, although an efficient exploitation of novel multifunctional molecules (such as recombinant proteins) requires solid understanding of their behaviour in native and non-native environments. In this work the (once) dried biopolymer (nanofibre) matrices were non-native environment for proteins, although all the material preparations were performed for never-dried native biopolymers. The studies mainly handled fundamental questions and tried to explain structure-property relationships through molecular architecture and macroscopic material properties, with tensile mechanical measurements as the main method of study.

The results of this thesis are based on four publications. Publications I, II and III focused on biosynthetic genetically engineered proteins and their interactions within the biopolymer matrices. Publication IV examined physically exfoliated graphene multilayers and their non-covalent interactions with the NFC matrix.

3. Materials and methods

3.1 Nanofibrillated cellulose

NFC (1.90–1.64% of solid contents depending on the batch) was processed by mechanical disintegration of bleached birch Kraft pulp by ten passes through an M7115 Fluidizer (Micro fluidics Corp.), essentially according to previous reports [97], before utilization in Publications I, II and IV. The NFC nanofibres were 5–20 nm in width and several micrometres in length. Bacterial cellulose (Nata de Coco, solid content 2.55 gl^{-1}) was used for the binding studies in Publication II together with nanofibrillated cellulose, as bacterial cellulose was easier to separate from the dispersion in the binding assay.

3.2 DCBD-HFBI (Publication I)

The bifunctional fusion protein, DCBD-HFBI, consisted of a hydrophobin part, which was connected to two different CBDs. The hydrophobin, HFBI, was from *Trichoderma reesei* [56] and the two CBDs were from enzymes Cel7A (previously CBHI) [98] and Cel6A (previously CBHII) [99] both from *T. reesei*. Polypeptide linkers were used to connect the domains together as reported previously [93]. The abbreviation DCBD-HFBI is used for the fusion protein, although it is structurally almost the same as the HFBI-DCBD-24mer used in Publication II. The proteins were purified using aqueous two phase extraction and reverse-phase high-performance liquid chromatography (RP-HPLC) as described in Linder et al. [100] followed by lyophilisation.

3.3 HFBI-DCBD-12-mer, -24-mer, -48-mer (Publication II)

Three fusion proteins were produced in *T. reesei* (Publication II), which are referred to here as HFBI-DCBD-12-mer, -24-mer and -48-mer (see Figure 11). The proteins are structurally identical with the exception of the length of the polypeptide linker in between the two CBDs. The HFBI-DCBD-12-mer had 12,

HFBI-DCBD-24-mer 24 and HFBI-DCBD-48-mer 48 amino acids in the DCBD-linker. The proteins were purified using aqueous two phase extraction and reverse-phase high-performance liquid chromatography (RP-HPLC) as described in Linder et al. [100] followed by lyophilisation.

3.4   DCBD-12-mer, -24-mer and -48-mer (Publication II)

The HFBI-DCBD-12-mer, -24-mer and -48-mer fusion proteins were digested with sequencing grade modified trypsin (Promega) in 25mM Tris-HCl 150mM NaCl buffer for 2 hours in room temperature. The trypsin cleavage was followed by reverse-phase ultra-performance liquid chromatography (RP-UPLC). The proteins were purified using aqueous two phase extraction and reverse-phase high-performance liquid chromatography (RP-HPLC) followed by lyophilisation.

3.5   ChBD-aspein (Publication III)

The bifunctional protein ChBD-aspein was engineered by utilizing a ChBD from a bacterial chitinase enzyme [101] and an aspein fragment from pearl oyster *Pinctada fucata* [102] (Publication III). Fractions containing the protein were pooled and further purified with reverse-phase high-performance liquid chromatography (RC-HPLC) and subsequently lyophilized.

3.6   Chitin production and isolation

Fresh frozen lobsters were obtained from a market in Stockholm city (CoopExtra, Sweden) as the starting material to isolate and produce chitin nanofibres. Tissues and salts were removed from the lobsters by washing them with water. The exoskeleton shells were freeze dried and crushed to a powder, which was demineralized in 2 M HCl for 2 hours. To remove pigments the demineralized powder was soaked in 96% ethanol overnight and subsequently in 20% NaOH for 2 weeks. A kitchen blender (VM0105E, USA) was used to disperse the colloidal nanofibre suspension at pH 3 in the presence of acetic acid and thereafter the suspension was homogenized by passing 10 times through the microfluidizer (Microfluidics, USA). The chitin nanofibre production process resulted in minor deacetylation of the chitin nanofibres, which was 5-13% depending on the measuring method [103].

3.7   Multi- and monolayered graphene (Publication IV)

Multi- and monolayer graphene flakes were directly exfoliated from Powder of Kish graphite (Natural Kish Graphite (Grade 50), Graphene Supermarket, U.S.A.) using a tip sonicator (Vibra-Cell VCX 750, 2 mm stepped microtip, Sonics and Materials

Inc., U.S.A.). The amount of sonication energy was monitored during graphene exfoliation, and 60% of the full output power was used for the tip amplitude. Graphite granules were dispersed into an NFC solution (2.0 gl^{-1}) with relatively high concentration of graphene flakes (usually around 50 wt% in relation to the NFC), from which smaller amounts of graphene flakes within a NFC dispersion were dosed in aqueous NFC dispersions for further sonication and dilution. The amount of graphene refers to a range of flakes that may contain multi- or monolayers of graphene.

3.8 Biomimetic mineralization of CaCO$_3$ of chitin films with and without ChBD-aspein

Mineral precursors CaCl$_2$ (0.5 M) and Na$_2$CO$_3$ (99.5%) were obtained from Sigma Aldrich and utilized without purification. The mineralization of CaCO$_3$ was performed in a glass beaker at room temperature with aqueous solutions of 0.05 M CaCl$_2$ and 0.05 M Na$_2$CO$_3$. Chitin nanofibres were diluted in water with and without ChBD-aspein proteins and the pH of the solution was adjusted to pH 8 using 0.1 M NaOH. CaCl$_2$ and Na$_2$CO$_3$ solutions were added into the nanofibre dispersions simultaneously and slowly by two syringe pumps with an even 40 ml/h flow. The solution of protein and salts was mixed with a magnetic stirrer during mineralization.

3.9 Film formation and stabilization

All of the freestanding films in Publications I, II, III and IV were prepared using the same basic method with slight differences in the sonication energy depending on e.g. sample viscosity or volume. All the suspensions and diluted dispersions were less than 3.5 mL in volume, because the high viscosity of fibrous biopolymers leads to an inefficient sonication of larger sample volumes. Sample dispersions were sonicated with a tip sonicator (Vibra-Cell VCX 750, Sonics & Materials Inc.) to enhance the dispersity of the biopolymers and in the case of graphite to exfoliate graphene flakes from graphite (see the section Multi- and monolayered graphene). The used amplitude of the sonicator tip was 40–60% of the full output power depending on the study. Vacuum filtration was used to create the freestanding films from sample dispersions containing NFC, chitin, proteins, ions, mineral crystals and/or graphene multilayers. The dispersions were filtered through Durapore membranes (GVWP, 0.22 µm, Millipore, U.S.A.), and an O-ring was used to define the diameter of the samples. After filtration of the films gentle pressure was applied using a 300 g load for 10 min to prevent wrinkling of the freestanding films. Films were dried overnight at +65 °C. After oven drying, the samples were stabilized in humidity controlled rooms or desiccators prior to further measurements.

3.10 Humidity control

Samples were conditioned in humidity controlled rooms prior to measurements, which were carried out at 25%RH or higher relative humidities. In the case of measurements in lower humidities than 25%RH, samples were taken directly from the oven into a humidity controlled box or desiccator where the measurement was carried out, and the samples were allowed to stabilize before measurement. The microtensile tests at 85%, and 50% RH were conducted in a humidity controlled desiccator, which was monitored with a hygrometer Testo 608-H1. The relative humidity of the desiccator or box was achieved by laboratory-made systems of flowing air. In the case of high humidity the air was humidified by running it through an aqueous medium. The relative humidity control was achieved by varying the pressure delivered to the desiccator or the measurement box. In Publication IV the mechanical testing was made in ambient conditions. Humidity was checked afterwards to have been around 50-60%RH. At the time when the mechanical tensile measurements for Publication IV were performed there was no humidity controlled chamber available and therefore the measurements were made in ambient conditions.

3.11 Mechanical tensile testing

In order to understand biopolymers as a matrix material in hybrids and nanocomposites, a short description is provided here of basic mechanical tensile testing with tensile properties, which is one of the main measurement methods used in this thesis to study molecular structure and structure-function relationships. A common way to study the structure-function relationships of a composite is to perform tensile measurements, in which a uniaxial force is applied to the sample. Figure 6 displays an example stress-strain curve for an unmodified NFC nanopaper, measured while the force is being increased linearly. Furthermore, the basic and commonly studied mechanical properties are attached to the tensile curve, which consists of elastic and plastic regions. Young´s modulus or elastic modulus is generally noted as the stiffness. It can be calculated from the (steep) slope at the beginning of the stress-strain curve, which usually appears in the range of 0–2% of relative strain depending on the material. Young´s modulus represents the ability of the material to resist the applied force without irreversible structural deformations and is thus an important value when analysing material properties. Yield strength defines the yield point, which is the non-linear part of the tensile curve at the end of the elastic region and represents the stress value that the material can bear before structures start to deform irreversibly. Beyond the yield point materials deform plastically, although some of the deformation may be reversible, giving the material an elastic element in the plastic region. During plastic deformation a material can show strain hardening (a concave curve as in Figure 6), strain softening (convex curve not shown in Figure

6) or constant stress (plastic flow, which would result in a straight line, also not shown in Figure 6). Strain hardening is a typical phenomenon for biopolymers that occurs during plastic deformation from a flow stress, which increases due to the inability of the long polymer chains to orient and relax over large strains because of the entanglements of the polymer chains [104]. Ultimate tensile strength is another important parameter that is also recognized as the maximum stress that the material can absorb before a crack occurs causing catastrophic crack propagation or necking, eventually leading to breaking of the material. Consequently, strain-to-failure is the maximum elongation (usually displayed as a relative value (%) in relation to the original length of the sample) that the material is able to undergo before breaking. Strain-to-failure may not be found at the maximum stress if the material shows strain softening (in this thesis strain-to-failure is always found at the point of ultimate tensile stress due to the material behaviour). The area under the stress-strain curve is a measure of toughness (or work-to-fracture), which is an important measure describing the materials ability to dissipate energy under tensile stress. Spider silk is one of the most studied biological materials for its extraordinary toughness and strength [105-108].
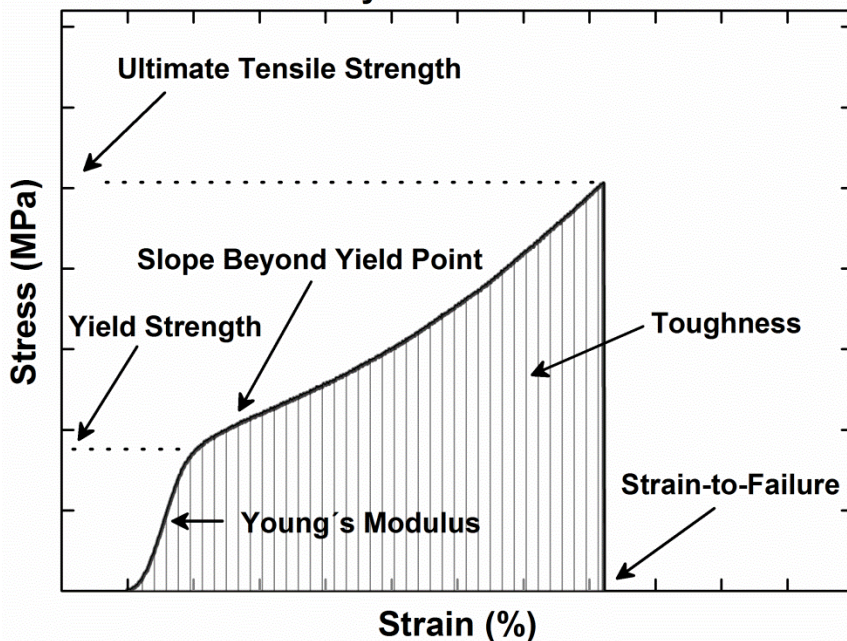
Figure 6. Schematic visualization of the mechanical properties of a tensile stress-strain curve from a biopolymer-based film.

Three different microtensile testers were used in Publication I, II, III and IV, in which the gauge length was set to 10 mm for all the samples in all the measuring

equipment. At least 4 specimens were measured from each sample throughout the studies. Specimen sizes were 2.0 cm x 2.0 mm x 4–15 µm, length, width and thickness, respectively, depending on the sample. Sample thicknesses were measured in Publications I and IV with SEM and in Publications II and III with a linear gauge (LGF-01100L-B transmission-type photoelectric linear encoder with EF-12PRH counter, Mitutoyo). At least 6 measurements from each sample were acquired in order to calculate an average value for thickness. The widths of the samples were measured with a digital sliding gauge (Digimatic, Mitutoyo) in all the studies.

Details of the microtensile device used in Publication I can be found in Burgert et al. [109]. The high precision linear stage was an Owis Limes 60 featuring a 2-phase step motor and the controller was a PI micos Pollux type 1. Tensile tests in Publication I were performed using a 50N load cell with a nominal strain rate of 8 µm*sec^{-1}. In Publications II and III the tensile testing was performed on a 5kN Tensile/compression module (Kammrath & Weiss GmbH, Germany) using a 100N load cell with a nominal strain rate of 8.35 µm/sec (0.5 mm/min). A mini tensile tester (Deben, UK) was used to perform mechanical tests for samples in Publication IV, in which a 20 N load cell was used with a nominal strain rate of 8.35 µm/sec (0.5 mm/min).

3.12 Electron microscopy

3.12.1 Cryo-TEM

High resolution transmission electron microscopy imaging was performed using JEOLS JEM-3200FSC Cryo- Transmission Electron Microscope operating at the temperature of liquid nitrogen. The cryo-TEM microscope was operated at 300 kV in bright field mode with an Omega-type Zero-loss energy filter. Ultrascan 4000 CCD camera (Gatan) was used to acquire images of the samples, which were maintained at -187°C. 3 µl aliquots of sample dispersions were vitrified on c-flat grids under 100% humidity with FEI Vitrobot. Specimens were blotted for 0.5–1.5 s with a filter paper and subsequently vitrified in a mixture of liquid ethane and propane (-180°C).

3.12.2 SEM (-EDX)

JEOLS JSM7500FA field emission scanning electron microscope (Japan) was carried out to image the cross-sections of the films. Acceleration voltages of 1−15 kV were applied depending on the sample. A thin layer of Pd, Au-Pd or PT was sputtered on top of the films (Emitech K950X/K350, Quorum Technologies Ltd., Kent, UK) to enhance imaging conditions and to prevent the charging of a sample. Films were aligned perpendicular to the electron beam. JSM-7500FA is also equipped with a JEOL energy-dispersive X-ray (EDX) analyser. The spectra were taken over 2 min using 15 keV electron energy to analyse the composition of

samples (Publication III). In Publication I the thickness of the films were measured with a scanning electron microscope FEI Quanta 200F (USA), in both low and high vacuum conditions.

4. Results and discussion

In this work two different types of carbohydrate binding domains were utilized: cellulose binding domains (CBD) and chitin binding domains (ChBD). The two binding domains are schematically demonstrated in Figures 7 and 3. Generally, the binding domains adhere to nanofibre surfaces, providing the opportunity to design other functionalities within the same protein and hence to functionalize the nanofibres non-covalently without alteration of the original structures. The approach seems facile as genetic engineering provides a vast number of naturally occurring functionalities that can be tailored together with binding domains. The fundamentals of the binding function of the binding domains were not studied further in this work, but merely utilized based on previous studies, in which their binding has been shown to be functional in aqueous media. Thus, the binding domains were evaluated qualitatively to confirm that their natural functions were preserved after genetic engineering (Publications I, II and III). Nevertheless, the binding function of differently constructed DCBDs was studied further in Publication II with the differently constructed DCBDs.
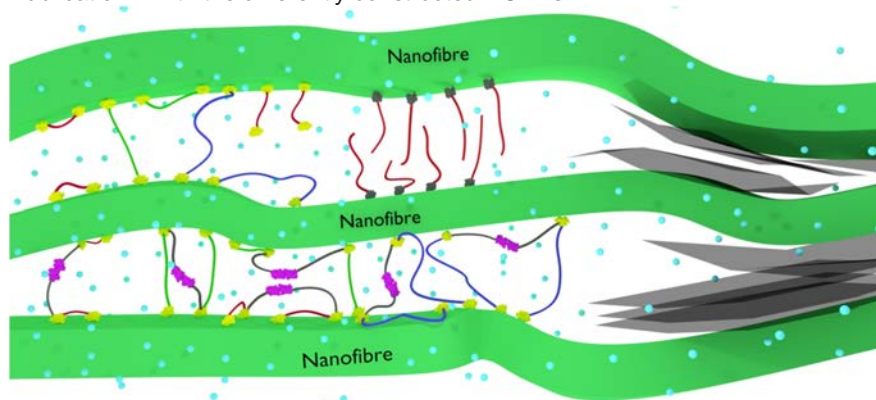
Figure 7. Schematic illustration of different non-covalently interacting molecules within native nanofibre matrices (NFC and chitin). Functionalization and modification of aqueous nanofibre networks were studied here through genetically engineered proteins and physically exfoliated multilayered graphene flakes. The yellow molecules represent cellulose binding domains (CBDs) that are tailored in

tandem to form double cellulose binding domains (DCBDs), in which the CBDs are connected together with different sized non-functional peptide linkers. Furthermore, the DCBD linkers are colour coded based on their length, so that the smallest linker is red (12 amino acids), the medium sized linker is green (24 amino acids) and the longest linker is drawn in blue (48 amino acids). A class II hydrophobin (HFBI) is marked with purple colour and connected to CBDs via another non-functional linker that is coloured grey, having a constant length in all of the fusion proteins containing HFBI. Chitin binding domains (ChBDs) are similar in functions to the CBDs with the exception that they adhere to chitin (nanofibres). The ChBDs are drawn as grey coloured domains on the nanofibre surfaces. Aspein domains are attached to the ChBDs and drawn as red peptide chains. The aspein chains are expected to be sticking out from the nanofibre surface due to their charged carboxylic groups (at pH 8) that repel each other. Graphene mono- and multilayers are drawn as translucent grey planes on the right side of the image between the nanofibres. In addition to the modifying molecules, water molecules are depicted with randomly placed light blue spheres, because the water has a role within the engineered biopolymer matrices. The sizes of the molecules are not drawn to scale but for illustration purposes with indicative measures.

In publications I and II, fusion proteins constructed from double cellulose binding domains (DCBDs) and a class II hydrophobin (HFBI) were studied. The mechanical properties of NFC matrix were tailored by biomolecular crosslinking in Publications I and II, in which the DCBD were designed to work as sacrificial binding units in order to enhance and modify the tensile properties of the nanocomposites. In Publication III, the ChBD was engineered in series with a totally different functional domain - an aspein domain, which becomes highly negatively charged at pH 8 due to its aspartate residues. Studies on aspein have shown it to possess interesting functions in ionic interactions and calcium carbonate biomineralization [102]. It is important to note that the HFBI, CBDs and ChBD all have rigid and well-known structures, whereas the aspein structure is loose and less well understood. Publication III investigates the utilization of ionic interactions as sacrificial bonds to enhance the mechanical properties of nanocomposite materials based on native chitin nanofibres. In addition to the ionic interplay, a conceptual opening was established in biomimetic calcium carbonate mineralization to develop truly nacre mimetic materials via the ChBD-aspein fusion protein (Publication III). Biomimetic mineralization is known to be a highly complex process; therefore the work in Publication III does not provide a comprehensive study of the mineralization of $CaCO_3$ (within a dynamic chitin nanofibre matrix) but suggests a novel route to construct nacre mimetic materials via genetically engineered protein within native chitin nanofibre matrix. Publication IV used a different approach in comparison to the other studies by performing a direct exfoliation of multilayered (and monolayered) graphene into aqueous NFC nanofibre matrix via self-assembly. Graphene is one of the "new nanomolecules" that has been named already as a miracle material and proposed to be a solution for many applications due to its properties [110]. The work is based on the surprising finding that NFC nanofibres are able to stabilize multi- and monolayers

of graphene non-covalently in aqueous dispersion without any other assisting molecules. In Publication III the aim was to form thin but large calcium carbonate platelets to reinforce the chitin/protein matrix, whereas Publication IV handled ideally perfect reinforcing nanosheets of graphene, which are mechanically superior to the $CaCO_3$ mineral platelets.

4.1 The tensile behaviour of unmodified NFC nanopaper and NFC/DCBD-HFBI hybrid under hydration (Publication I)

In the first part the effect of moisture was examined on NFC/DCBD-HFBI hybrid and on an unmodified NFC film. The amount of a fusion protein, DCBD-HFBI, was chosen to be 1:1 in weight in relation to the NFC nanofibres in order to occupy as much of the nanofibre surface as possible. The effect of the amount of fusion protein was examined later with three different fusion proteins (12-mer, 24-mer and 48-mer in the presence of HFBI), of which the HFBI-DCBD-24-mer closely resembled structurally and functionally the DCBD-HFBI. The other two fusion proteins in Publication II (HFBI-DCBD-12-mer and -48-mer) differed structurally only in their DCBD linker length, but significantly in their behaviour.

FT-IR and TGA were used to confirm the presence of the DCBD-HFBI within the hybrid film (see Publication I supplementary information Figures S1 and S2). Sorption measurements were subsequently carried out to determine whether the amount of absorbed moisture deviates between the NFC/DCBD-HFBI hybrid and the unmodified NFC film. The results showed higher amounts of absorbed moisture for the hybrid film throughout the humidity range (5%-85%RH), which is logical since the proteins bind water naturally (Publication I, Figure 1). The hybrid film has a bulky character of several micrometres in thickness, which allows vapour to penetrate the film and to bind on the protein-modified NFC nanofibre matrix. The HFBI part of the fusion protein has a hydrophobic side, which does not bind to the nanofibres and is known to form multimers, whereas other parts of the protein contain sites that enable binding of water molecules and thus higher moisture content than in the unmodified NFC film.

Non-cyclic tensile tests were carried out next for both unmodified NFC and NFC/DCBD-HFBI hybrid films in four different humidities (5%RH, 25%RH, 50%RH and 85%RH). The corresponding stress-strain curves are shown in Figure 8. In the figure, the plasticizing effect of water is clearly visible for unmodified NFC film, where the hydrogen bonding-dominated nanofibre matrix is clearly lubricated and softened by the introduction of water molecules (Figure 8a). Reductions in Young's modulus and yield strength with improved strain-to-failure and toughness demonstrate the propensity of the unmodified NFC film to lose its stiffness in high humidities. The bound moisture is likely to lubricate the inter-fibre interactions, allowing the fibres to slide against each other more easily. In order to modify and more importantly to enhance the hydration-dependent highly percolating biopolymer matrices, the added interacting molecules need to be able to withstand moisture and possibly to work in synergy with the inter-fibre interactions of the

biopolymer matrix. In order to improve the material's stability in higher humidities, the interactions need to be able to outcompete water molecules. The binding domains provide an alternative approach, since they have evolved in Nature to overcome the problem of adhesion in an aqueous environment.

Figure 8b exhibits the altered performance of the NFC/DCBD-HFBI hybrid in four humidities. The humidity-dependent mechanical behaviour of the hybrid is changed drastically in comparison to the unmodified NFC film. Strain-to-failure shows significant reductions, which can be considered a drawback, because the NFC network is natively highly ductile as seen in Figure 8a. When the ultimate tensile strengths are examined it becomes clear that they are almost the same as in the unmodified NFC films, suggesting that only the means to reach the ultimate tensile strength are changed, which results in lower strain-to-failure values (Publication I, Figure 3). Excluding the measurement at 85%RH, at which the ultimate strength is apparently lower for the hybrid than for the unmodified NFC film, the properties of the hybrid are interesting with promising and distinct characteristics. Importantly, the stress-strain curve and properties at 50%RH show increase in yield stress and elastic modulus with close to the same ultimate strength as in unmodified NFC film, suggesting protein-mediated properties, which appear to be humidity dependent. The multivalent binding of the CBDs in fusion protein seem to be able to outcompete hydrogen bonds of water molecules while overriding the hydrogen bonded NFC network in once dried non-native state (at least to some extent).
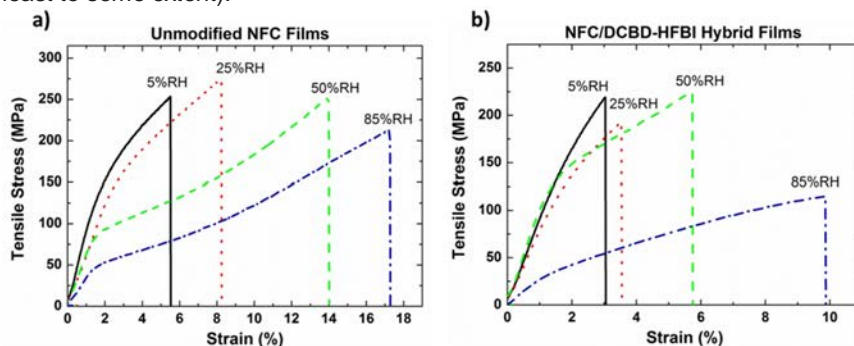
Figure 8. Representative stress-strain curves from non-cyclic tensile tests in four different humidities for a) unmodified NFC film and b) NFC/DCBD-HFBI hybrid film. Solid black curves represent measurements at 5%RH, dotted red curves at 25%RH, dashed green curves at 50%RH and dash dotted blue curves at 85%RH. Adapted from Publication I with permission from American Chemical Society.

Cyclic tensile measurements are a powerful tool to study the nature of interactions, which dominate the elastic region. Cyclic tensile measurements were performed by increasing the applied stress in cycles until the breaking of a sample occurred. During the measurements the stress was allowed to decrease to zero between each cycle. Figure 9 presents representative stress-strain curves from

cyclic measurements for both films in three humidities (25%RH, 50%RH and 85%RH). Both films deformed plastically beyond the yield point and a rather constant elastic modulus was detected throughout the cycles for both of the films, which can only result from reversible bonds that are able to reorganize during stress release, especially beyond the yield point when irreversible structural deformations take place. The stiffness of a material would begin to decrease (distinctively) beyond the yield point in the case of irreversible bond-dominated elastic properties. This result is reasonable since the interactions of HFBI and CBDs are non-covalent and reversible by nature even though the system is dry in comparison to their natural working environment.
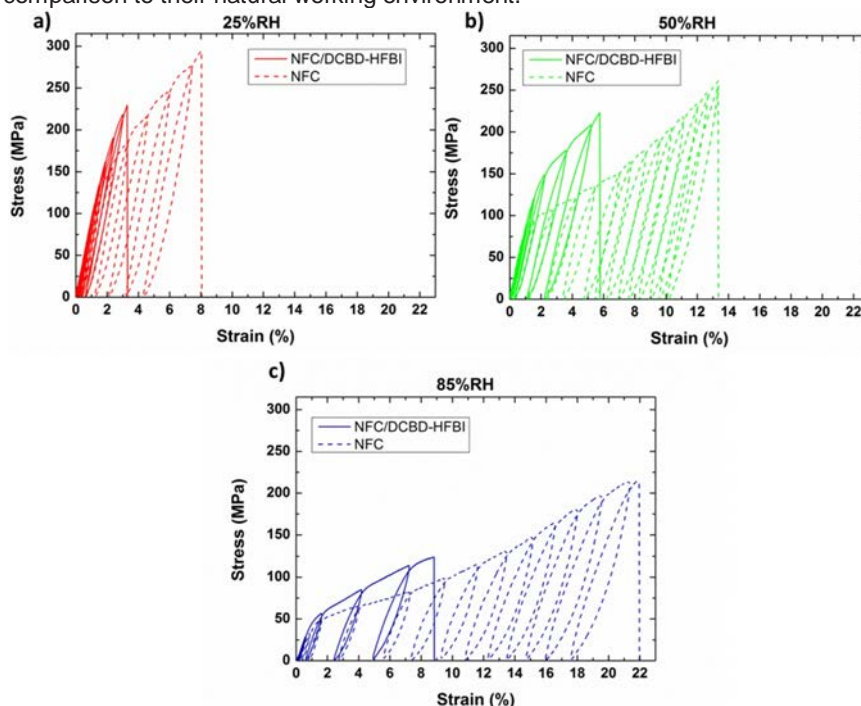
Figure 9. a–c) Representative stress-strain curves from cyclic tensile measurements in 25%RH (red), 50%RH (green) and 85%RH (blue), respectively. NFC/DCBD-HFBI hybrid is shown with solid curves and the unmodified NFC film with dashed curves. Adapted from Publication I with permission from American Chemical Society.

A closer investigation of the plastic region was conducted, since the unmodified NFC film and the NFC/DCBD-HFBI hybrid deviated most clearly during plastic deformation in all of the humidities. Figures 10a and c display the yield strengths of NFC and NFC/DCBD-HFBI in non-cyclic and cyclic measurements, respectively. Notably, the yield strength of the NFC/DCBD-HFBI hybrid is preserved at 50%RH, whereas the unmodified NFC film shows significantly lower

yield stress already at 50%RH. Both of the films exhibit clear strain stiffening beyond the yield point in the plastic region. The unmodified NFC film shows non-linear and pronounced stiffening towards the end of the measurement, whereas the hybrid displays rather pronounced but linear strain stiffening throughout the plastic region. Interestingly, the slope beyond the yield point displays remarkably higher values for the hybrid in all of the humidities in comparison to the unmodified NFC film although the NFC film shows a more pronounced and non-linear slope at the end of the plastic region. The strain stiffening moduli for both of the films are presented in Figures 10b and d for non-cyclic and cyclic measurements, respectively. A steeper slope in the plastic region indicates more effective resistance to plastic deformation. Non-linear and increasing strain stiffening occurs usually at high strain values due to the inability of long polymer chains to reorient during plastic deformation, mostly due to the pronounced fibre-fibre entanglements and interactions. The slopes in the plastic region were calculated directly after the yield point because the non-linearity in the unmodified NFC film at the end of the measurement would have caused problems in determining the slope accurately. The slopes in the plastic regions deviated most between unmodified NFC and NFC/DCBD-HFBI hybrid film for all of the mechanical properties and were visible in all humidities. When the strain stiffening modulus was plotted as a function of relative humidity (Figures 10b and d), the difference between the two films is seen to decrease at 85%RH. At this humidity level, the amount of adsorbed moisture is notably higher for the NFC/DCBD-HFBI hybrid film (Publication I, Figure 1), suggesting that the moisture may eventually interfere with the binding of the protein domains and even more probably with the NFC fibre-fibre interactions.
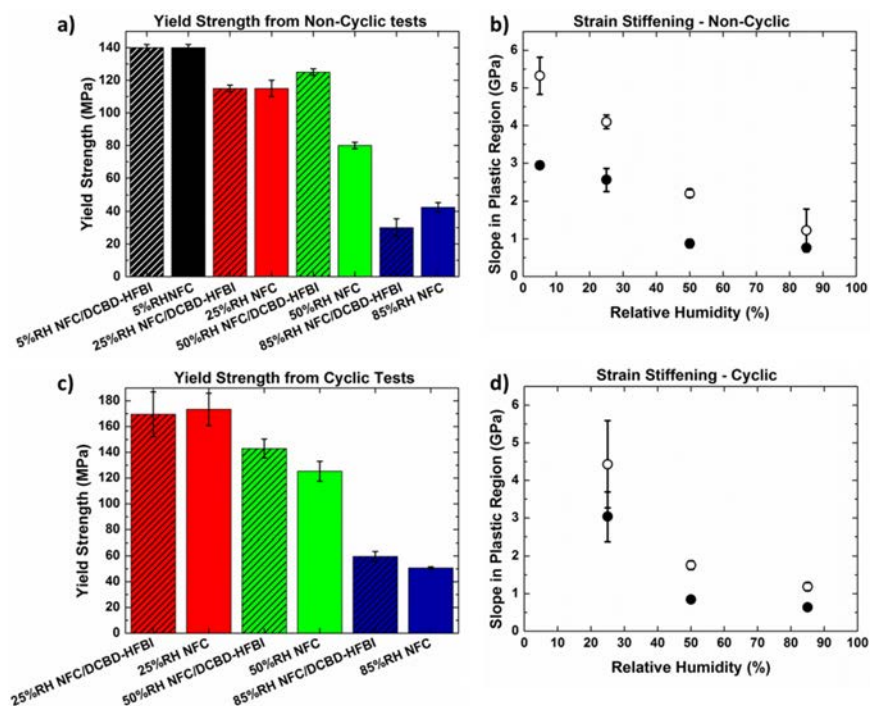
Figure 10. a–b) Yield strengths and strain stiffening moduli of unmodified NFC and NFC/DCBD-HFBI films from the non-cyclic measurements. c–d) Yield strengths and strain stiffening moduli of NFC and NFC/DCBD-HFBI films from cyclic measurements. Strain stiffening moduli are presented as a function of relative humidity b) in 5%RH, 25%RH, 50%RH and 85%RH and d) in 25%RH, 50%RH and 85%RH, from left to right, respectively. The open circles represent the NFC/DCBD-HFBI hybrid and the black closed circles the unmodified NFC film in b and d. At least four measurements were used to calculate averages. All data is presented with standard deviations. Adapted from Publication I with permission from American Chemical Society.

4.2   Designing the DCBD linker for improved mechanical properties (Publication II)

The functions of the two domains (HFBI and DCBD) could not be interpreted conclusively in the study described in the previous section (Publication I), although the behaviour of the NFC/DCBD-HFBI hybrid resembled a crosslinking effect. In publication II the roles of the two functional domains were studied more closely. A schematic illustration of the six new protein constructs is presented in Figure 11. Different DCBD linkers are illustrated from the shortest to the longest with red (12-mer), green (24-mer) and blue (48-mer), respectively. Amino acid sequences for the fusion proteins are also highlighted using the same colours as for the

schematic DCBD domains in Figure 11. The DCBD-HFBI (Publication I) resembles closely the fusion protein HFBI-DCBD-(24-mer); both have same sized DCBD linker of 24 amino acids and they are considered as close equals. The DCBD-(48-mer) has the longest linker of 48 amino acids, whereas the DCBD-(12-mer) contains the shortest linker of only 12 amino acids. The fusion proteins all have a trypsin cleavage site between the HFBI and DCBD domains (marked in Figure 11 as bold and underlined **R**), which enables physical separation of the two domains and generation of the three DCBD proteins, thus facilitating study of the DCBD parts in the NFC matrix without the multimerization domain HFBI.

Fusion-12-mer	HFBI-DCBD-(12-mer) (20.6 kDa): SNGNGNVCPPGLFSNPQCCATQVLGLIGLDCKVPSQNV YDGTDFRNVCAKTGAQPLCCVAPVAGQALLCQTAVGAG GGSGGGSGGGSENLYFQGTPGASTSTG**R**GPGGQACSS VWGQCGGQNWSGPTCCASGSTCVYSNDYYSQCLPGA NPPGTTTTSTQSHYGQCGGIGYSGPTVCASGTTCQVLNP YYSQCL	DCBD-12-mer
Fusion-24-mer	HFBI-DCBD-(24-mer) (21.6 kDa): SNGNGNVCPPGLFSNPQCCATQVLGLIGLDCKVPSQNV YDGTDFRNVCAKTGAQPLCCVAPVAGQALLCQTAVGAG GGSGGGSGGGSENLYFQGTPGASTSTG**R**GPGGQACSS VWGQCGGQNWSGPTCCASGSTCVYSNDYYSQCLPGA NPPGTTTTSRPATTTGSSPGPTQSHYGQCGGIGYSGPTV CASGTTCQVLNPYYSQCL	DCBD-24-mer
Fusion-48-mer	HFBI-DCBD-(48-mer) (23.7 kDa): SNGNGNVCPPGLFSNPQCCATQVLGLIGLDCKVPSQNV YDGTDFRNVCAKTGAQPLCCVAPVAGQALLCQTAVGAG GGSGGGSGGGSENLYFQGTPGASTSTG**R**GPGGQACSS VWGQCGGQNWSGPTCCASGSTCVYSNDYYSQCLPGA NPPGTTTTSRPATTTGSSPGPPPGANPPGTTTTSRPATTTG SSPGPTQSHYGQCGGIGYSGPTVCASGTTCQVLNPYYSQ CL	DCBD-48-mer
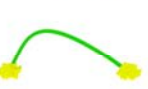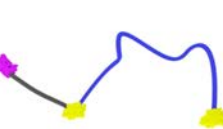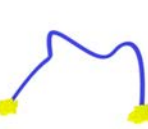
Figure 11. Amino acid sequences of the three HFBI-DCBD (12-mer, 24-mer and 48-mer) constructs. Schematic models of the HFBI-DCBD fusions are shown on the left and of the DCBD proteins on the right. The different molecular motifs are not in drawn in relation to their true sizes, but rather with indicative dimensions. The trypsin cleavage site is marked with a bold and underlined letter R.

First the binding behaviours of the three DCBD proteins were studied to assess their binding properties, because the differently sized linkers were expected to limit or to enable different degrees of freedom in the binding. The binding isotherms from both NFC and bacterial cellulose for the three DCBD proteins are shown in Figure 12. In general, both substrates showed similar binding behaviour, but the measurements from NFC show larger deviations. This is probably because the NFC nanofibres could not be fully removed from the dispersion, which is required for an accurate determination of the amount of free protein in the supernatant. The results differed slightly from those of a previously reported study, in which a protein resembling the DCBD-24-mer was studied [111]. Importantly, the three

DCBD proteins displayed differences in their binding isotherms and binding capacities. The binding capacities indicate differences in the binding modes of the DCBDs (Figures 12 and 15). The DCBD-48-mer shows the most altered behaviour with the lowest binding capacity, whereas the DCBD-24-mer exhibits almost the same or only slightly lower capacity than the DCBD-12-mer. The binding affinities also differ between the proteins, but they are not expected to affect the behaviour of the nanocomposite films due to the dry state. The binding assay results are accurate enough to distinguish differences in the binding behaviours. The focus was on studying the DCBD linker-length dependent behaviour from the mechanical tensile perspective using DCBD and fusion protein hybrid films.
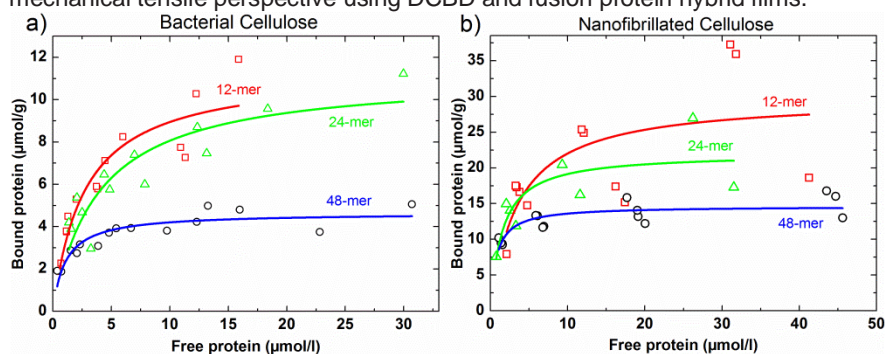
Figure 12. The binding isotherms of the cleaved DCBD proteins from a) bacterial cellulose and b) NFC binding measurements. Red squares and curves represent DCBD-12-mer, the green circles and curves the DCBD-24-mer and the blue triangles and curves the DCBD-48-mer (Publication II).

The hydration induced mechanical behaviour of NFC/DCBD-HFBI hybrid and the unmodified NFC nanopaper was studied in Publication I, in which the amount of protein was kept constant (1:1) in relation to the amount of NFC nanofibres. The effect of the amount of proteins was studied with the fusion hybrids in Publication II. Three protein concentrations ($0.5gl^{-1}$, $0.85gl^{-1}$ and $1.5gl^{-1}$) were chosen for nanocomposites, which correspond to 26 to 78 µM for HFBI-DCBD-(12-mer), 24 to 74 µM for HFBI-DCBD-(24-mer), and 22 to 67 µM for HFBI-DCBD-(48-mer). The amount of NFC was again kept constant ($2.0gl^{-1}$) in all the films throughout the study. The mechanical results of the three fusion hybrid films exhibited similar behaviour to that of the NFC/DCBD-HFBI hybrid (Publication I) when compared to the unmodified NFC film. The results showed reduced strain-to-failure and toughness with improved yield strength and stiffness (Publication II, supplementary information), but also differences between the three fusion protein hybrids in mechanical performance. The improvements in the stiffness were more pronounced in all three protein concentrations for all three fusion proteins than in the previously studied DCBD-HFBI hybrid, in which the amount of protein was higher. Thus, the protein-mediated mechanical behaviour appears to be dependent on the amount and the structure of the protein (Publication II). The

longer DCBD linkers of the fusion proteins demonstrate more pronounced Young's modulus and yield stress with slightly higher ultimate tensile strengths, which suggests that the differently sized non-functional linkers play a role in the once dried fusion protein modified NFC matrix under tensile stress. Consequently, it appears that the DCBD linker can affect the molecular structures and dynamics already in the presence of the multimerization domain HFBI.

   A more applied approach is needed to differentiate and define the roles of the DCBD and HFBI domains, although the role of the HFBI moiety is known to be in forming multimers with other HFBI domains. A physical separation of the HFBI domain from the DCBD domain was performed with trypsin (Publication II). Based on the tensile properties of the nanocomposites with different protein amounts, where the HFBI-DCBD-48-mer hybrid showed the most pronounced effects at $0.85gl^{-1}$, it was decided to use $0.85gl^{-1}$ protein concentrations for all three cleaved hybrid films. The representative stress-strain curves for $0.85gl^{-1}$ of protein-containing hybrids and unmodified NFC film are shown in Figure 13a, in which solid red, green and blue curves represent the HFBI-DCBD-12-mer,-24-mer and -48-mer fusion hybrids, respectively, and the dashed red, green and blue curves the DCBD-12-mer, -24-mer and -48-mer hybrids, respectively. In addition, the solid black line represents the unmodified NFC film. Furthermore, the average values for Young´s modulus, yield strength, ultimate tensile strength, slope after yield point, strain-to-failure and toughness are shown in Figure 14.
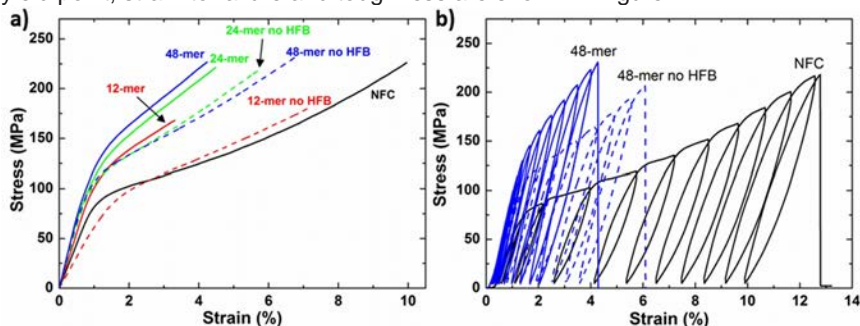
Figure 13. a) The representative stress-strain curves from non-cyclic tensile tests for unmodified NFC film, the fusion hybrids and cleaved DCBD hybrids with 0.85gl-1 protein content and 2.0 gl-1 NFC. b) Representative stress-strain curves from cyclic tensile tests of unmodified NFC film, cleaved DCBD-48-mer hybrid and HFBI-DCBD-48-mer fusion hybrid with 0.85gl-1 protein content and 2.0gl-1 NFC, where unmodified NFC film contains only 2.0gl-1 NFC. Unmodified NFC film is shown with a solid black curves, the cleaved DCBD hybrids with dashed coloured curves and fusion hybrids with solid coloured curves, with red for 12-mer, green for 24-mer and blue for 48-mer for both a) and b).
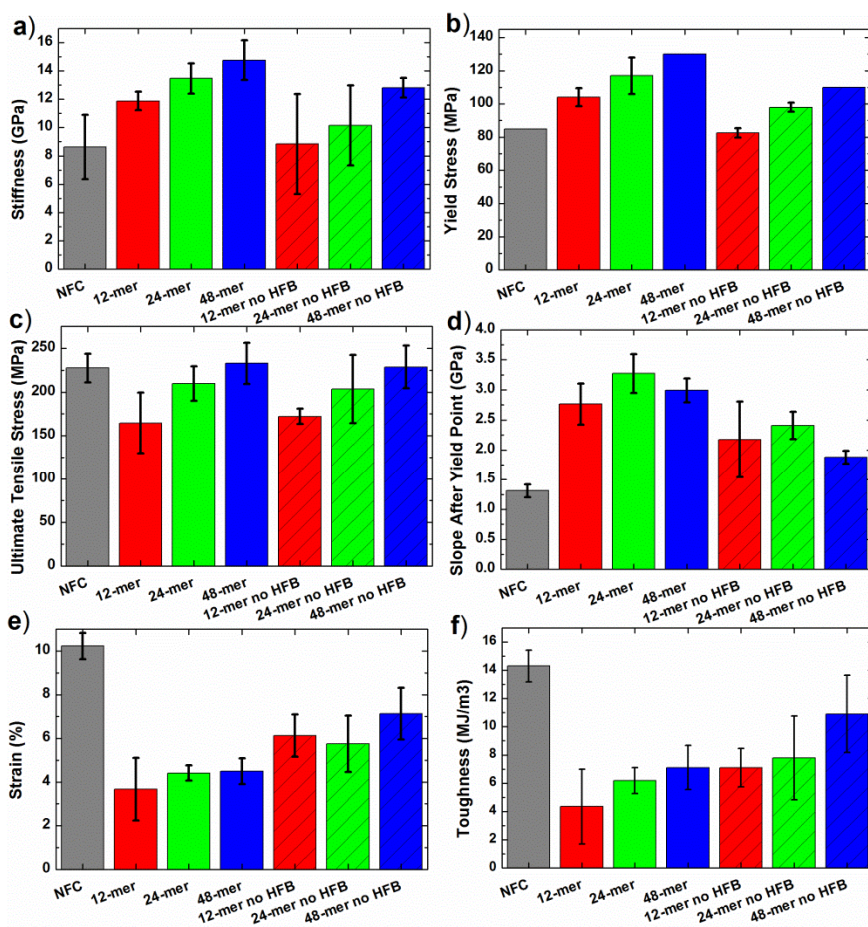
Figure 14. Mechanical tensile properties for the six hybrid films with 0.85gl-1 protein and 2.0gl-1 NFC, excluding the unmodified NFC film, which contains only NFC. a) Young's modulus, b) yield strength, c) ultimate tensile strength d) slope after yield point e) strain-to-failure and f) toughness. At least four measurements were used to calculate average values. All data is presented with standard deviations. The other mechanical properties for the hybrids with different amounts of fusion proteins can be found in Publication II supplementary information.

In general, the protein-mediated properties show enhancements in elastic modulus, yield strength and slope after the yield point (strain stiffening modulus). The longest linker in the DCBD-48-mer hybrid shows the most well-defined effect on the mechanical performance, having the highest elastic modulus and yield strength, which can result from an effective biomolecular crosslinking of the NFC matrix. The smallest DCBD linker clearly limits the behaviour of the DCBD-12-mer hybrid, since the Young´s modulus and yield strength fall far from those of the

HFBI-DCBD-12-mer hybrid and other DCBD hybrids. DCBD-24-mer hybrid shows a performance in between the DCBD-12-mer and -48-mer hybrids, which is analogous to the behaviour of the HFBI-DCBD-24-mer within the fusion protein hybrids. Strain stiffening modulus was lower for all DCBD hybrids in comparison to the fusion protein hybrids, suggesting that the interactions during plastic deformation are not as effective after the separation of the HFBI domain.

To investigate the nature of the interactions between unmodified NFC, HFBI-DCBD-48-mer-NFC and DCBD-48-mer-NFC, cyclic tensile measurements were carried out and the representative stress-strain curves were shown in Figure 13b. The hybrids with the longest DCBD linker (48-mer) were studied, since the effects were most pronounced with the DCBD-48-mer domain and because all of the six proteins are based on the same molecular interactions due to their identical functional domains, although the linker length seems to affect the synergetic binding and the interplay of the two CBDs in a DCBD. The cyclic results exhibited differences similar to those observed in the non-cyclic tests and the samples differed clearly from each other. However, all of the films displayed a relatively constant elastic modulus through the cycles, confirming that the dominating interactions at the elastic region are based on reversible bonds in all of the films.

In order to understand how the binding results might explain the mechanical performance or vice versa, it is necessary to contemplate the behaviours with schematic illustrations of the possible molecular structures (Figure 15). Linder et al. suggested that the binding affinity of a DCBD with DCBD linker of the same size as the linker in the DCBD-24-mer would generate a situation, in which it is energetically more favourable for the two CBDs to bind the same cellulose (nanofibre) surface rather than separate ones [94], because the binding of one CBD brings the other tethered CBD into the vicinity of the cellulose surface increasing the local CBD molecule concentration in comparison to a single CBD [94]. By comparison, it is possible that the smallest linker (12-mer) is too short to allow both of the CBDs to bind to the same NFC nanofibre, leaving one of the CBDs unbound but more likely to limit the binding of the DCBD-12-mer to the same NFC nanofibre as proposed by Linder et al. [94]. However, if another nanofibre is in close range the possibly unbound but tethered CBD might be able to reach the other nanofibre causing biomolecular crosslinking between two nanofibres especially during plastic deformation, when the nanofibres are slipping against each other and aligning. This model would explain the strain stiffening modulus of the DCBD-12-mer hybrid, since the fibres are aligning under tensile stress and the probability of an unbound but tethered CBD finding a cellulose surface is increasing. Furthermore, the DCBD-48-mer with the longest linker provides an option where both of the CBDs in the DCBD-48-mer are able to bind equally well but are probably even more likely to bind separate nanofibres due to the long length of the linker, causing crosslinking of the NFC network. Based on the results, the DCBD-24-mer appears to be able to bind separate nanofibres as well, which may still be less probable than with the DCBD-48-mer because the linker is only half as long. The binding abilities would explain the altered binding capacities. The DCBD-12-mer and -24-mer bind most probably with both of the

CBDs to the same and sometimes to separate nanofibres, whereas the DCBD-48-mer is likely to bind always with both CBDs and often to separate nanofibres. The linker length-dependent crosslinking densities could explain the differences in the binding capacities alongside with the mechanical properties of the different hybrids. It is also probable that the longer linkers occupy more space, inhibiting the binding of other DCBD molecules and therefore partly affecting the binding capacities.
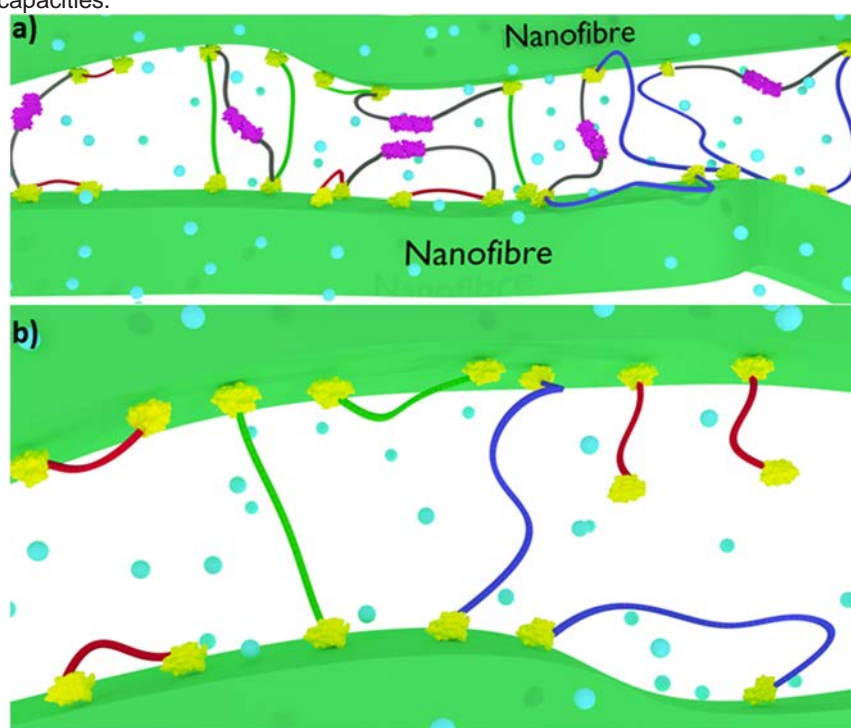
Figure 15. Schematic illustrations of the possible molecular structures of the fusion and DCBD hybrids. a) Proposed molecular structures of the fusion protein hybrids and b) DCBD hybrids in the NFC matrix based on their mechanical performance and binding studies. HFBI domains are drawn in violet, the NFC nanofibres in green (larger molecules appearing up and down in the images) and the CBDs in yellow. The different DCBD linkers connect the two CBDs together with non-functional peptide chains, in which the DCBD-12-mer linker is highlighted with red, the DCBD-24-mer linker with green and the DCBD-48-mer with blue. The molecules are not drawn to scale.

Although the altered mechanical behaviour may be explained to some extent by the different binding configurations (Figure 15), the results provide basis also for different molecular dynamics between the different protein-containing hybrids. Figure 16 presents proposed molecular dynamics during tensile measurements with respect to the proteins and their different sized linkers. Whereas the binding

modes may be limited and controlled by the linker length, it is possible that the linker allows sacrificial binding of the two tethered CBDs during tensile measurements. With the shortest DCBD-12-mer linker the detaching of the CBDs may be simultaneous, requiring less energy and therefore resulting in lower mechanical performance in the dried state in relation to the other DCBD hybrids with longer linkers. In the case of DCBD-24-mer and -48-mer it seems logical that the tethered CBDs are detached from the surface one at the time, during which the linker is straightened. This non-simultaneous detaching consumes more energy and provides improved elastic and plastic tensile properties. Consequently the DBCD-units work as sacrificial binding units alongside with the multimerizing HFBI domains.
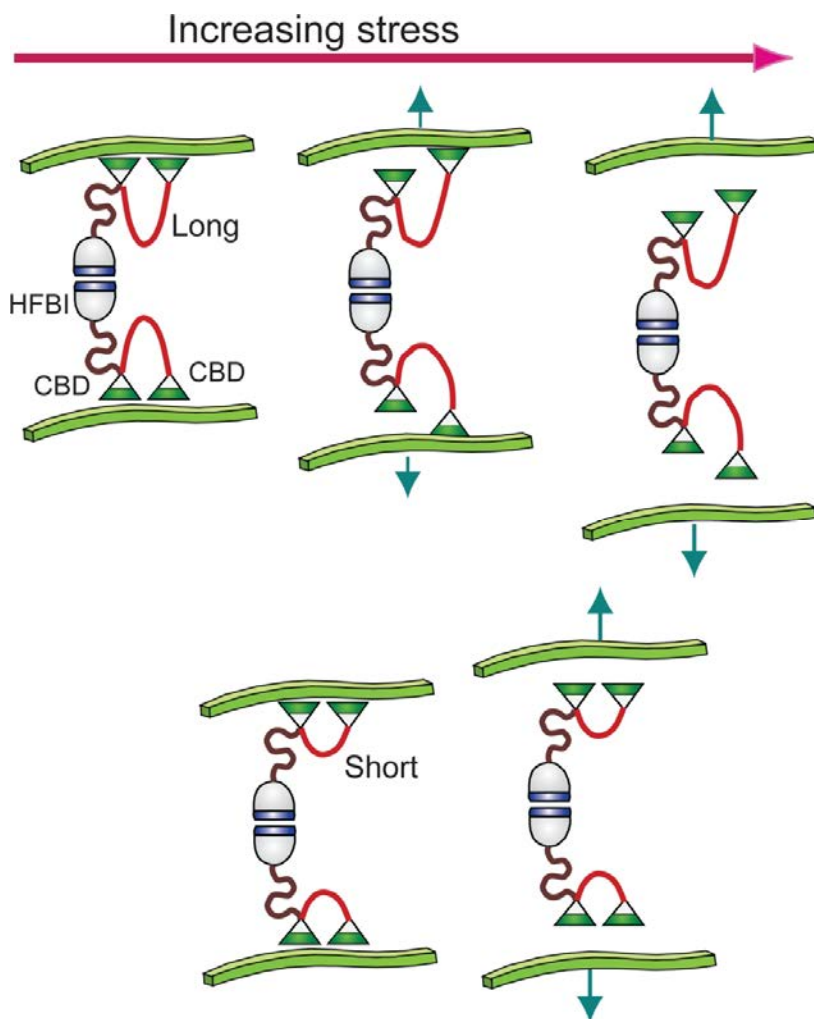
Figure 16. Linker length-dependent sacrificial bonding. Longer linkers allow non-simultaneous detachment of the tethered CBDs, while the linker provides hidden length scale. Both the separate detachment of the two CBDs and the straightening of the linker consume energy, thus improving the (plastic) tensile properties. The shortest linker is likely to lead to a simultaneous detachment of both the CBDs, which requires less energy and thus results in lower (plastic) tensile properties.

4.3 Ionic crosslinking and biomimetic mineralization of native chitin matrix via bifunctional ChBD-aspein (Publication III)

In this study chitin nanofibres [79] were exploited by performing a non-covalent modification using chitin binding domain-aspein fusion proteins (ChBD-aspein). Both of the functional domains were first assessed separately. The binding experiment was performed on chitin beads and the results displayed a regular binding isotherm, confirming that the ChBD had preserved its function during fusion with the aspein fragment (Publication III). The preliminary biomimetic mineralization experiments were performed on ChBD-aspein-modified chitin beads, in which the minerals appeared in the vicinity of the ChBD-aspein-modified beads with a controlled crystal size (Publication III). The results confirmed that both ChBD and the aspein had retained their known functions during genetic engineering. Although chitin beads were used in the binding and preliminary mineralization studies, chitin nanofibres would serve as a better matrix material for the creation of biosynthetic nanocomposites. Figure 4b presented a cryo-TEM image of vitrified dispersions of unmodifed chitin nanofibres, in which some aggregation was visible due to the nature of the unmodified chitin nanofibres. The nanofibres were functionalized using the bifunctional ChBD-aspein protein. The aspein moiety contains several carboxylic groups (aspartates), which are deprotonated at pH 8, making it highly negatively charged and attractive to positively charged ions such as divalent calcium ions.

The introduction of ChBD-aspein to the nanofibre dispersion led to enhanced dispersion of the nanofibres (at pH 8), which is a logical response due to the repulsive forces created by the charged aspein domains on the chitin nanofibre surfaces. Four separate films were formed by vacuum filtration: unmodified chitin film, chitin film in the presence of calcium ions, ChBD-aspein/chitin hybrid and ChBD-aspein/chitin film in the presence of calcium ions. The films were subsequently tested with a micro tensile tester in controlled humidity (30%RH) and ambient temperature (21°C). The mechanical tensile results can be seen in Figure 17a-d. An increase in Young´s modulus (5.5 GPa) was observed in the ChBD-aspein/chitin hybrid, with no other clear changes in mechanical performance. Introduction of the calcium ions to the ChBD-aspein functionalized chitin nanofibre film resulted in an even higher Young´s modulus (7 GPa) and importantly also in an increase in the ultimate tensile strength (120 MPa). The presence of the calcium ions in the mechanically stiffened and strengthened ChBD-aspein/chitin hybrid was further confirmed with SEM-EDX spectroscopy (Publication III, supplementary information Figure S4). Since the protein-modified chitin film showed slightly increased elastic modulus but no increase in ultimate tensile strength in the absence of calcium ions, the results indicate that the ChBD-aspein might have only improved the dispersity of the chitin nanofibres and consequently the stiffness of the ChBD-aspein/chitin hybrid film, whereas the increment in ultimate tensile strength required additional sacrificial bonds to resist the

deformation and to dissipate more energy. Introduction of calcium ions showed no improvements in the chitin film in the absence of the ChBD-aspein protein, suggesting that the protein provided the platform for the interplay between calcium ions and the nanofibres. A schematic representation of the possible molecular structures and interplay is presented in Figure 19a.
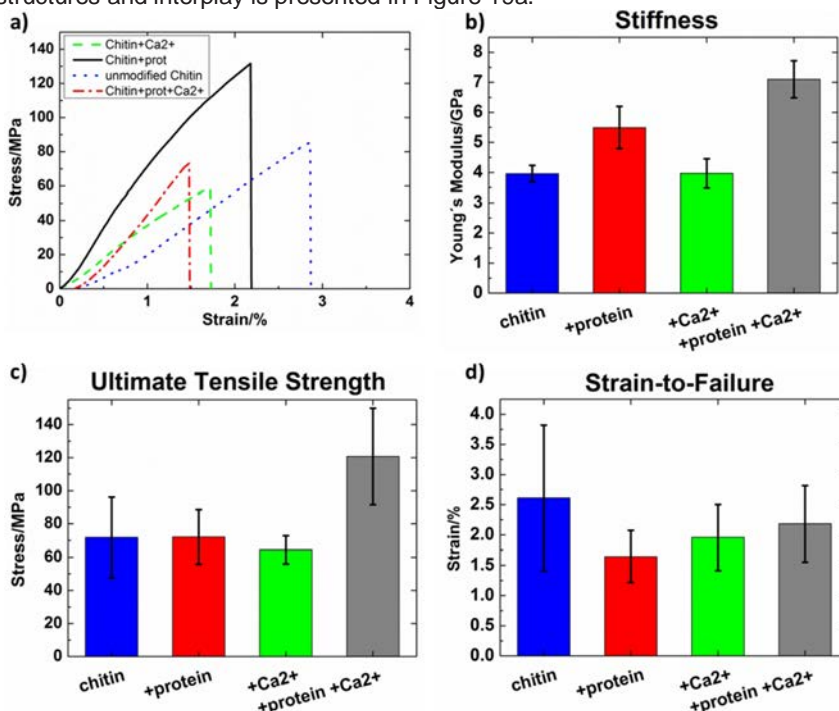
Figure 17. Mechanical properties of the chitin and chitin/ChBD-aspein films in the presence and absence of calcium ions. a) Representative stress-strain curves, b) Young's modulus, c) ultimate tensile strength and d) strain-to-failure values for unmodified chitin film (blue), ChBD-aspein/Chitin hybrid film (red), Ca2+-chitin film (green) and the Ca2+-ChBD-aspein/Chitin hybrid film (grey) with standard deviations. The solid black curve represents Ca2+-ChBD-aspein/Chitin hybrid, the dashed green curve the Ca2+-Chitin, the dotted blue curve the unmodified chitin and the dash-dotted red curve the ChBD-aspein/Chitin film. At least four measurements were used to calculate average values. All data is presented with standard deviations. Adapted from Publication III with permission from the Royal Society of Chemistry.

Enhancement of the mechanical properties through ionic interplay of the bifunctional protein and calcium ions provided an encouragement to push the studies even further to perform biomimetic mineralization of calcium carbonate within the protein modified chitin matrix. This approach can be considered to be truly nacre mimetic, since nacre is thought to grow calcium carbonate platelets

within the aqueous chitin-protein matrix (referred to as the organic framework and organic matrix in the introduction) during construction of the mechanically desirable shell structures [48]. Two concentrations of $CaCl_2$ and $NaCO_3$ were chosen so that the lower amount had close to the same molar content of charges as in the ChBD-aspein modified chitin network and the other concentration was tenfold higher. Moreover, the amount of calcium ions in the ionically modified ChBD-aspein/chitin film was equal to the amount of charges on the chitin nanofibre surfaces and thus the same as in the case of the lower amount of the salts ($CaCl_2$ and $NaCO_3$) in the biomimetic biomineralization. Unmodified chitin dispersions were used as control samples in order to follow the biomimetic mineralization in the absence of the protein. Figure 18a presents a cross-sectional SEM image from the $10XCaCO_3$-ChBD-aspein/Chitin. The wide angle x-ray scatter (WAXS) results showed clear calcite peaks only for the $10XCaCO_3$-ChBD-aspein/Chitin hybrid whereas the other films had no traces of calcium carbonate in the WAXS measurements (Figure 17b).
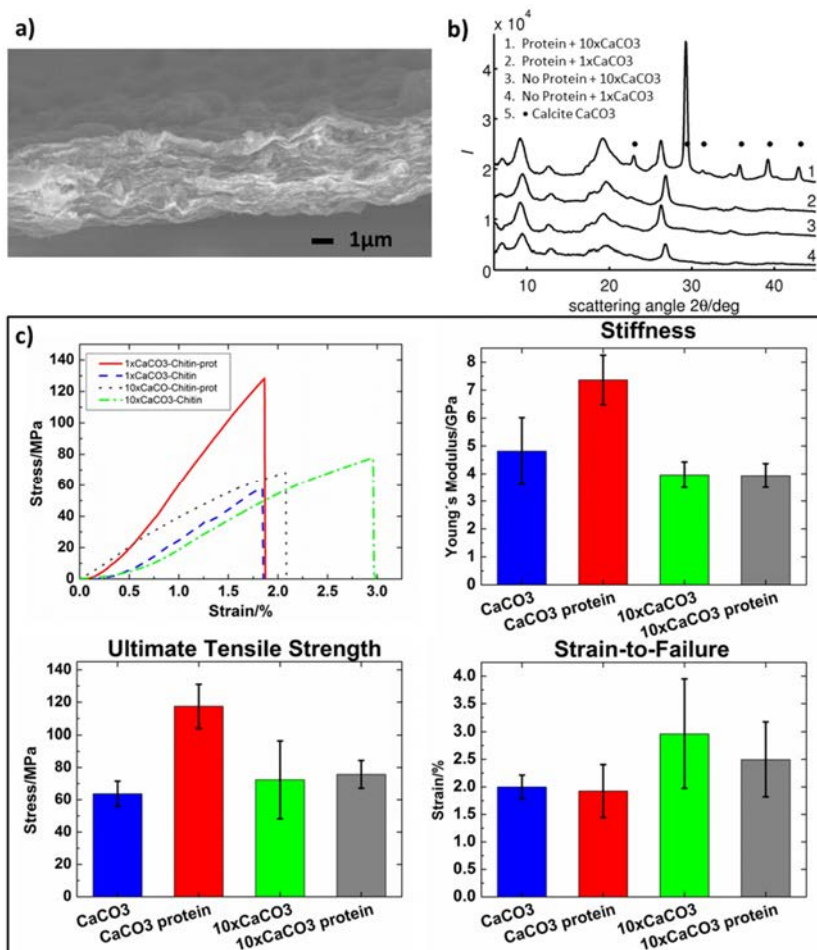
Figure 18. Hybrid films after biomimetic biomineralization of calcium carbonate with and without ChBD-aspein. a) An SEM image from the cross-section of the 10xCaCO3-ChBD-aspein/Chitin film, which was the only film in which CaCO3 crystals were found by WAXS. b) WAXS spectra from the four hybrid films, in which the common locations for the calcium carbonate peaks are shown with black dots. c) Representative stress-strain curves for samples prepared with 1xCaCO3 (dashed blue curve), 1xCaCO3 with protein (solid red curve), 10xCaCO3 (dash-dotted green curve), and 10xCaCO3 with protein (dotted dark grey curve). Average values with standard deviations of stiffness, ultimate tensile strength and strain-to-failure are also shown. At least four measurements were used to calculate average values. All data is presented with standard deviations. Adapted from Publication III with permission from the Royal Society of Chemistry.

The mechanical tensile tests showed higher stiffness (7 GPa) and enhanced ultimate tensile strength (120 MPa) only for the $1xCaCO_3$-ChBD-aspein/chitin, in

which no crystals were measured with WAXS. This hybrid had approximately the same amount of calcium ions as the ionically cross-linked ChBD-aspein/chitin hybrid film, and surprisingly similar mechanical performance (Figure 18c). This might be due to the fact that the protein can bind almost all the calcium ions and thus inhibit the calcium carbonate nucleation in the presence of the low amounts of calcium and carbonate ions. Inhibition might result in a situation in which the calcium ions are bound and retained within the ChBD-aspein modified chitin hybrid to generate sacrificial bonds between ChBD-aspein modified nanofibres as schematically presented in Figure 19a. The $10xCaCO_3$-ChBD-aspein/chitin film showed traces of calcite crystals in WAXS, although the mechanical performance was unchanged in relation to the unmodified chitin film. Figure 19b presents suggested molecular structures for the $10xCaCO_3$-ChBD-aspein/chitin hybrid.

The possible explanation for the unchanged mechanical properties of the $10xCaCO_3$-ChBD-aspein/chitin is that the mineralized $CaCO_3$ crystals are round in shape, which is usually an inefficient shape for reinforcing particles for the construction of mechanically high-performing nanocomposites. However, the results suggest that the crystal growth is affected and that the crystals are retained within the chitin nanofibre matrix only in the presence of ChBD-aspein protein. Although neither the Young´s modulus (4 GPa) nor the ultimate tensile strength (70 MPa) were enhanced in the hybrid film in the presence of $CaCO_3$ crystals, the preservation of the properties suggests that the nanocomposite material was properly integrated and that the aspein domains may have been interacting with the formed crystals. Thus, the approach can be considered promising even though a considerable amount of additional work would be required to gain control over the morphology and aspect ratio of the crystals for nacre-like mechanical performance and structures. Hierarchical self-assembly over higher length scales is also needed when targeting properties of natural nacre (40–70 GPa of stiffness and 80–135 MPa of tensile strength) [5]. It remains a mystery how Nature is capable of synthesizing such a brilliant nanocomposite materials (e.g. nacre and bone) in ambient and mild conditions [4]. Mimicking of the construction principles of natural materials can be considered as important as the final structures and properties for the development of biomimetic high-performance materials.
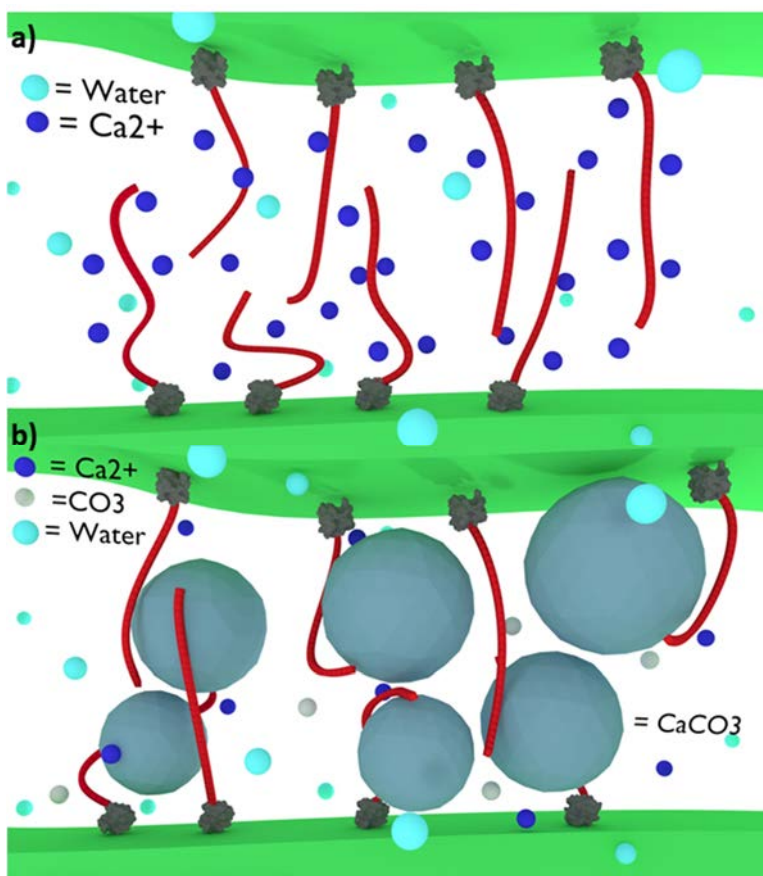
Figure 19. Schematic illustration of the proposed molecular interactions and self-assembled structures of the protein-modified hybrids. a) Visualization of the molecular structures of Chitin/ChBD-aspein/Ca^{2+} hybrid film. The dark blue spheres represent the calcium ions within the ChBD-aspein decorated chitin nanofibre matrix. b) Illustration of the biomimetic mineralization of calcium carbonate crystals within ChBD-aspein modified chitin nanofibre matrix. $CaCO_3$ crystals are shown as large grey-blue spherical particles, in which the round shape of the particles is exaggerated. The molecules are not drawn to scale.

4.4 NFC nanocomposites with multilayered graphene (Publication IV)

The final study (Publication IV) was also inspired by the brick-and-mortar type of structure of nacre, although here the nanocomposite material was formed from multilayered graphene and cellulose nanofibres. The work was initially inspired by the work of Laaksonen et al. [92], in which DCBD-HFBI (the same fusion protein

as used in Publication I) was used to bind hydrophobic graphene flakes and cellulose nanofibres together. Here, the exfoliation of graphene multilayers was attained directly into an aqueous dispersion of NFC nanofibres by tip sonication without any assisting molecules. A cryo-TEM image from a vitrified dispersion of graphene multilayers and cellulose nanofibres can be seen in Figure 20b. The exfoliated graphene flakes were stable in the aqueous dispersion of NFC nanofibres, which could be due to the mechanical interlocking of large graphene platelets, although it is also possible that the NFC nanofibres can interact with the aromatic graphene flakes. Hydrophobic interactions exist within amphiphilic NFC nanofibres, even though the interfibrillar hydrogen bonding dominates the behaviour of the nanofibres. Studies have suggested the existence of a specific interaction between aromatic moieties and sugar rings of biopolymers [54]. The results of the study described in Publication IV are insufficient to conclude whether exfoliated graphene flakes can actually interact with the NFC nanofibres via a specific interaction, but the results do indicate synergistic mechanical properties.
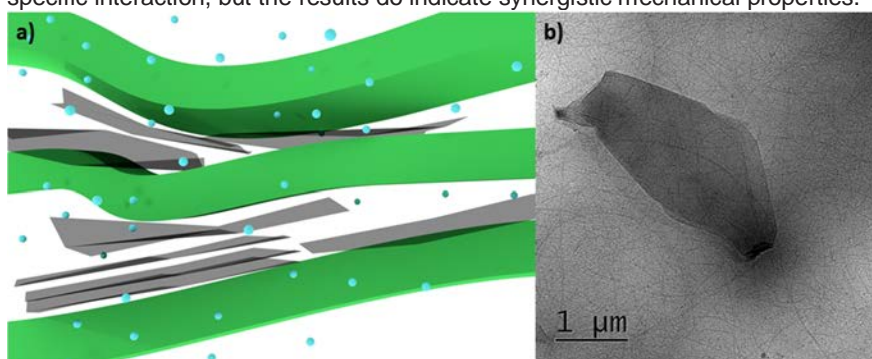
Figure 20. Visualization of the exfoliated and intercalated graphene flakes in the aqueous NFC nanofibre matrix. a) Schematic illustration of the graphene flakes and the NFC nanofibres. The molecules are not drawn to scale. b) Cryo-TEM image of a vitrified dispersion of the exfoliated graphene multilayers within the NFC nanofibre matrix.

Nanocomposite films with variyng amounts of graphene multilayers were created through tip sonication and vacuum filtration, while the amount of NFC nanofibres was kept constant ($2.0gl^{-1}$) in all of the films. The amount of graphene multilayers was noted in relation to the amount of NFC. Figures 21a and b present cross-sectional SEM-images from an unmodified NFC nanopaper and 50wt% of graphene-containing NFC nanocomposite, respectively. The thick, incompletely exfoliated or intercalated graphene flakes can be seen in the cross-section of the nanocomposite containing 50wt% of graphene multilayers. The exfoliation was more complete for the nanocomposites with less graphene, in which both mono- and multilayers of graphene were detected by Raman spectroscopy (Publication IV, Figure 3). The transparency and flexibility of the nanocomposites were also improved significantly with lower amounts of graphene multilayers. Figures 21c

and d display the flexibility and the translucency of the NFC nanocomposite containing 1.25wt% of graphene multilayers. Nanocomposites appeared to be firm candidates for the mechanical tensile testing because they had retained to some extent the ductility of NFC (Figure 21c). Ductility is often clearly reduced when large amounts of reinforcing platelets are introduced into a nanofibre matrix in the rule-of-mixtures composites [8]. The reason for preserved ductility might be the non-covalent interactions, which do not inhibit the percolation of the NFC nanofibres and thus the ductility of the graphene -NFC nanocomposites is like that of unmodified NFC nanopaper.
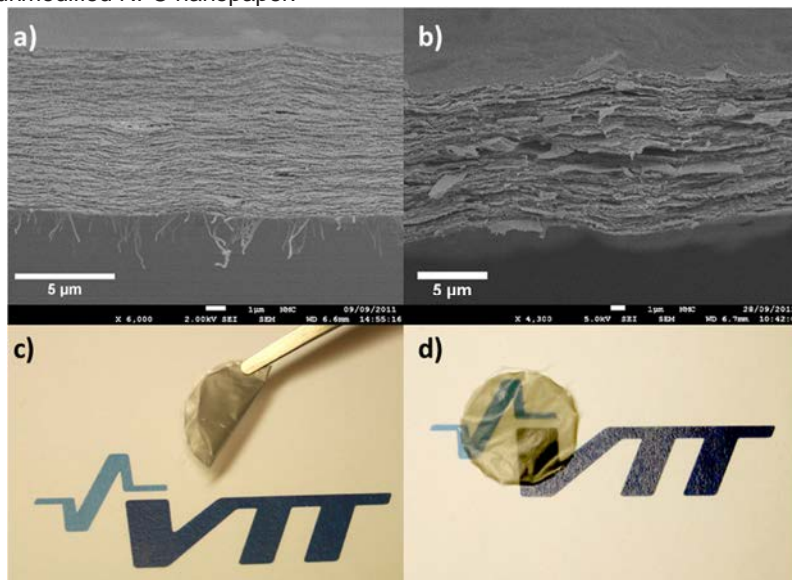
Figure 21. Visualization of an unmodified NFC nanopaper and NFC nanocomposites with graphene multilayers. a–b) Cross-sectional images of unmodified NFC nanopaper and NFC nanocomposite with 50wt% of graphene multilayers, respectively. c–d) Photographs of NFC nanocomposite containing 1.25wt% of graphene multilayers to demonstrate the flexibility and the translucency of the nanocomposites, respectively. Adapted from Publication IV with permission from American Chemical Society.

The mechanical tensile results are presented in Figure 22, in which the nanopaper-like appearance matches surprisingly well with the ductile behaviour of all the films. All nanocomposites demonstrated rather unchanged strain-to-failure values of around 10%, which can be considered high for nanocomposites containing significant amounts of graphene (from the perspective of the rule-of-mixture [8]). The SEM image in Figure 21b displayed thick graphene flakes at the cross-section of nanocomposites, with high amounts of poorly exfoliated and intercalated graphene sheets, which is unideal for optimized mechanical performance. The nanocomposites with high amounts (over 5wt%) of graphene

platelets showed reduced mechanical properties, with the exception of only slightly decreased strain-to-failure values. An "optimal" range of graphene multilayers was found at around 1.25wt% of graphene, where the Young's modulus, yield strength, ultimate tensile strength and toughness all exhibited significant improvements with a well preserved strain-to-failure value. The results display a synergetic effect of inter-fibre interactions of NFC and the exfoliated graphene flakes, which might be due to the alignment of the nanofibres and possibly due to specific interactions between aromatic graphene platelets and cellulose sugar rings. The suggested interactions between graphene flakes and cellulose nanofibres are solely based on the mechanically improved performance and were not confirmed by any direct method.
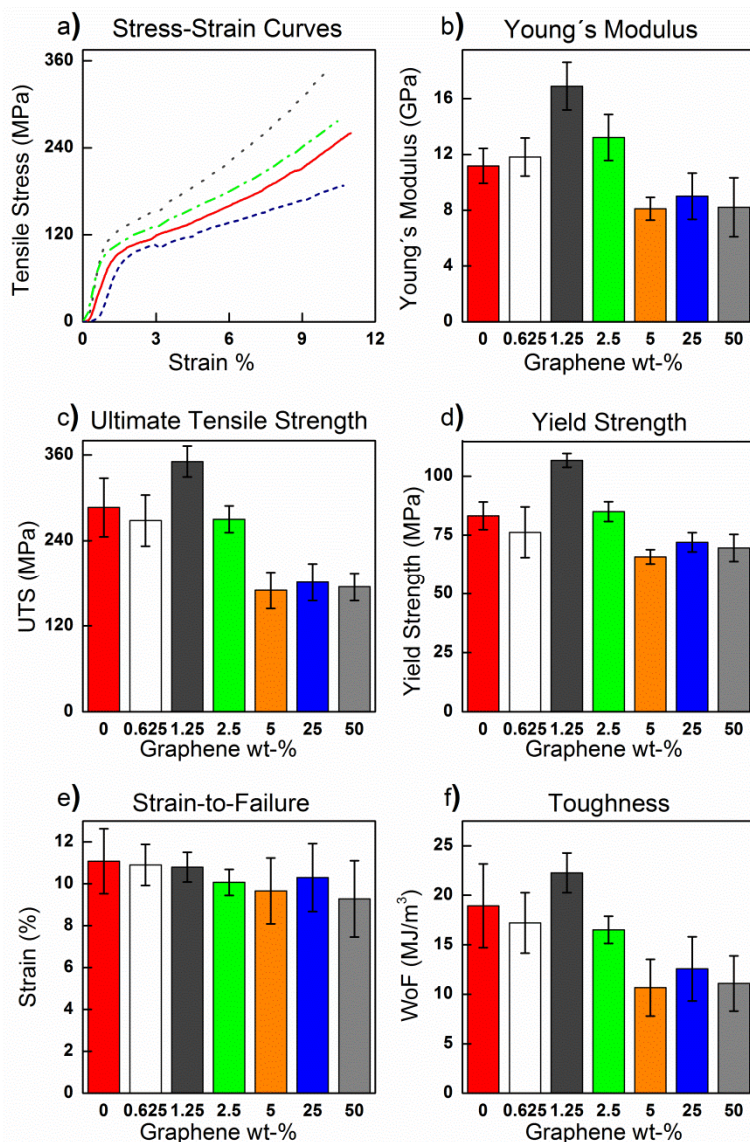
Figure 22. Mechanical tensile results from unmodified NFC film and NFC nanocomposites with varying amounts of graphene multi-layers. a) Representative stress-strain curves for unmodified NFC film (solid red curve), nanocomposite with 1.25%wt of graphene multilayers (dotted dark grey curve), nanocomposite with 2.5wt% of graphene multilayers (dash-dotted green curve) and nanocomposite with 25wt% of graphene multilayers (dashed blue curve). b-f) Young's modulus, ultimate tensile strength, yield strength, strain-to-failure and toughness, respectively, for unmodified NFC film and nanocomposites with standard deviations, where red represents the unmodified NFC film, white the 0.625wt% of

graphene multilayers, dark grey 1.25wt% of graphene multilayers, green the 2.5wt% of graphene multilayers, orange the 5wt% of graphene multilayers, blue the 25wt% of graphene multilayers and grey the 50wt% of graphene multilayers. At least four measurements were used to calculate average values. All data is presented with standard deviations. Adapted from Publication IV with permission from American Chemical Society.

Graphene flakes can be considered as ideal reinforcing platelets, because they possess exceptional mechanical properties in addition to their other interesting properties [110, 112, 113]. However, exploitation of the full potential of graphene (or graphene oxide) platelets has not been achieved in nanocomposites. Graphene- and graphene oxide-based nanocomposites have been studied extensively in recent years with biopolymers such as chitosan [114] and with many synthetic polymers such as poly (vinyl alcohol) (PVA) [115]. More information about the recent progress in graphene-based nanocomposites can be found in some recent reviews [116-118]. Many of the graphene-based nanocomposites handle graphene oxide rather than graphene, partly because of the inert and poorly dispersible character of unmodified graphene flakes. The tip sonication allowed us to exfoliate graphene directly into aqueous NFC network, although this is rather harsh method to transfer energy into the dispersion and is likely to cause degradation of the nanofibres by cutting them into shorter pieces. However, the tip sonication is also known to enhance the dispersity of the nanofibres by opening their fine structure. Sonication may also induce defects into the exfoliated graphene flakes, which can cause deterioration of their native properties. Still, the method is simple and attractive choice for the utilization of NFC nanofibres and graphene flakes in mild aqueous media without any assisting molecules. Although the mechanical performance yielded promising results as the ductility was preserved with improved stiffness, strength and toughness, up-scaling appears unlikely at the moment due to problems with the tip sonication, in which the sample volume, tip size and the possible defects require further studies.

5. Conclusions

Designing of the molecular architecture of biopolymer matrices through non-covalent interactions showed significant relevance for the mechanical performance and can be considered as a promising approach to construct and to study biopolymer matrices for materials science applications. Both the number of interacting components and the strength of interactions need to be optimized and tailored for effective engineering of the highly percolating nanofibre networks. Ideally all of the matrix components should be able to work cohesively over several length scales in order to obtain multifunctional properties similar to those of Nature's materials [13].

Proper adhesion within the matrix components was realized in this work using only non-covalent and weak interactions via recombinant fusion proteins and exfoliated graphene multilayers. The recombinant proteins showed that the elastic modulus can be tuned by the introduction of stronger, yet non-covalent, crosslinking and sacrificial binding units via biological multimerization and binding domains (Publications I and II). The utilization of ionically interacting protein domains gave rise to improved performance in the presence of divalent calcium ions via sacrificial bonds (Publication III). The deformations in the elastic region are reversible by nature, although when the material is stressed beyond the elastic region even the foundations for elastic properties may be disintegrated, which is often the case with materials that have elastic properties that are dominated by covalent interaction. Cyclic tensile measurements used in Publications I and II is a useful method to confirm the reversibility of the elastic properties of nanocomposite materials. Interestingly, clear effects were also observed in the plastic region, where the presence of the non-covalently interacting molecules improved the resistance of the materials to plastic deformations under tensile stress. In addition, the sacrificial bonding was further tuned by molecular designing (Publication II).

The construction of biomimetically mineralized nanocomposites showed promising results via natural mineralization domain of aspein [102], although the effect of mineralized components appears to be complex and requires further studies. The results indicate that the protein interacted with the ions and possibly with the created minerals, because both the ions and the minerals were retained

within the organic matrix. However, no other evidence was acquired concerning the possible interactions between the minerals and the aspein domain. The mineralized nanocomposite structures did not resemble the structure of nacre either mechanically or visually [119]. The lack of improvements in mechanical properties suggests that the interactions between the aspein and the minerals were not adequate and that the matrix functioned merely as a template for the mineralization of $CaCO_3$ [36]. On the other hand the interpretation of mineralized chitin matrix is far from straightforward, and several other factors such as the particle size and shape can affect the properties. At the moment the mineralized structure of bone might actually be a more realistic model and target for material construction via biomimetic mineralization, because bone contains mineralized fibres, in which the mineral content is approximately half the organic content, whereas the highly defined $CaCO_3$ platelets of nacre comprise over 95% of the total volume [12]. As a conclusion, the organic matrix may be easier to adjust for an optimal mechanical performance than the construction and assembly of the mineral particles for an optimized reinforcing phase.

New high performance molecules, e.g. graphene, have emerged recent decades. These are available for utilization in man-made materials instead of the ceramic or mineral particles that are often used in biological nanocomposites. In Publication IV, the utilization of nearly ideal reinforcing platelets of graphene (multilayers) showed how relatively large amounts of inorganic material can be applied directly into a biopolymer matrix without any assisting molecules, and thus the method stands out as a promising approach. The tensile results of the graphene-NFC nanocomposites showed improved properties with low amounts of exfoliated graphene multilayers. The possible reason for mechanical enhancements may reside in the non-covalent interactions, which may allow NFC matrix to percolate and to work in synergy with the added graphene flakes. Higher amounts of graphene did not result in enhanced mechanical properties but they displayed relatively unchanged strain-to-failure, which is a step towards integration of the native properties of the ductile NFC nanofibres with relatively high amounts of inorganic material [5].

In summary, non-covalent modification of the biopolymers appears to be a promising route to develop multifunctional nanocomposite materials. Despite the enhancements in mechanical properties of biopolymer nanocomposites, some bottlenecks were encountered. The modification of the matrices appeared to result in unchanged or sometimes reduced ultimate tensile strength, suggesting that only the means to reach the threshold for the maximum tensile stress were changed and at times were also met earlier. The reason for this might be in the amounts of biopolymers, which dominated all of the materials and thus the properties of a single nanofibre may have limited the performance of the nanocomposites in ultimate tensile strength. Absolute values are not very reliable indicators of a material's performance, due to the heterogeneity issues of biopolymers and their processing history. However, some studies have been able to show higher tensile strengths for NFC nanopaper by aligning the biopolymer nanofibres [85], which suggests that the inter-fibre interactions become more effective due to the

alignment, allowing improved stress transfer in the biopolymer matrix and thus higher ultimate tensile strength and stiffness. On the other hand, when the shape of the stress-strain curve is dramatically altered (indistinguishable plastic region [85]), it refers to significantly altered molecular structure and behaviour of the biopolymer matrix and thus the material cannot be compared directly in the sense of structure-property relationships. Here the chitin and the NFC-graphene nanocomposites showed increased ultimate tensile strength via protein-calcium mediated sacrificial bonds and the synergistic behaviour of graphene-NFC matrix, respectively. Improved tensile strength refers to more effective utilization of the properties of the nanofibre networks and possibly enhanced stress transfer within the matrices, which can be considered as another step forward in understanding and utilising biopolymers as matrices for structural materials.

This work demonstrated how bioinspired approaches can be used to tailor native biopolymer matrices in mild aqueous conditions to construct hybrid and nanocomposite materials. All of the utilized molecules interacted non-covalently with the matrices without alteration of the biopolymer structures. Genetic engineering provides a novel route to construct materials by designing the structural components and their functions at the molecular level. The disadvantage of the approach is the time consuming synthesis, production and characterization of the novel (multi)functional molecules. In addition, there are other bottlenecks such as the cultivation and purification methods, and also possible issues concerning protein heterogeneity, all of which can impede the work significantly. The existence of these issues was acknowledged with no further discussion to limit the focus of this work to the applying of the novel multifunctional proteins. In the future, more complete understanding could possibly be achieved using several alternative loading rates in mechanical tensile testing and by carrying out rheological measurements and dynamic mechanical analysis. In addition to experimental methods, modelling would allow more thorough investigation of the molecular and macroscopic behaviour of the molecules and of the nanocomposite materials if combined with experimental studies. Hence, a combination of experimental and theoretical studies will be desirable in the future.

References

1. Meyers, M.A., et al., *Biological materials: structure and mechanical properties.* Progress in Materials Science, 2008. **53**(1): p. 1-206.
2. Fratzl, P., et al., *On the role of interface polymers for the mechanics of natural polymeric composites.* Physical Chemistry Chemical Physics, 2004. **6**(24): p. 5575-5579.
3. Klemm, D., et al., *Nanocelluloses: A New Family of Nature-Based Materials.* Angewandte Chemie International Edition, 2011. **50**(24): p. 5438-5466.
4. Ji, B. and H. Gao, *Mechanical properties of nanostructure of biological materials.* Journal of the Mechanics and Physics of Solids, 2004. **52**(9): p. 1963-1990.
5. Espinosa, H.D., et al., *Merger of structure and material in nacre and bone– Perspectives on de novo biomimetic materials.* Progress in Materials Science, 2009. **54**(8): p. 1059-1100.
6. Ajayan, P.M., et al., *Nanocomposite science and technology*. 2006: John Wiley & Sons.
7. Jones, R.M., *Mechanics of composite materials*. 1998: CRC Press.
8. Qin, Z., et al., *Robustness-strength performance of hierarchical alpha-helical protein filaments.* International Journal of Applied Mechanics, 2009. **1**(01): p. 85-112.
9. Ritchie, R.O., *The conflicts between strength and toughness.* Nature Materials, 2011. **10**(11): p. 817-822.
10. Kim, H.S., *On the rule of mixtures for the hardness of particle reinforced composites.* Materials Science and Engineering: A, 2000. **289**(1–2): p. 30-33.
11. Ortiz, C. and M.C. Boyce, *Bioinspired structural materials.* Science, 2008. **319**(5866): p. 1053-1054.
12. Fratzl, P., et al., *Structure and mechanical quality of the collagen–mineral nano-composite in bone.* Journal of Materials Chemistry, 2004. **14**(14): p. 2115-2123.
13. Dunlop, J.W., et al., *Artful interfaces within biological materials.* Materials Today, 2011. **14**(3): p. 70-78.
14. Chen, P.-Y., et al., *Biological materials: Functional adaptations and bioinspired designs.* Progress in Materials Science, 2012. **57**(8): p. 1492-1704.
15. Keckes, J., et al., *Cell-wall recovery after irreversible deformation of wood.* Nature Materials, 2003. **2**(12): p. 810-813.
16. Jackson, A.P., et al., *The Mechanical Design of Nacre.* Proceedings of the Royal Society of London. Series B. Biological Sciences, 1988. **234**(1277): p. 415-440.
17. Rho, J.-Y., et al., *Mechanical properties and the hierarchical structure of bone.* Medical Engineering & Physics, 1998. **20**(2): p. 92-102.

18.   Luz, G.M. and J.F. Mano, *Biomimetic design of materials and biomaterials inspired by the structure of nacre.* Philosophical Transactions of the Royal Society A: Mathematical, Physical and Engineering Sciences, 2009. **367**(1893): p. 1587-1605.

19.   Tang, Z., et al., *Nanostructured artificial nacre.* Nature Materials, 2003. **2**(6): p. 413-418.

20.   Bonderer, L.J., et al., *Bioinspired design and assembly of platelet reinforced polymer films.* Science, 2008. **319**(5866): p. 1069-1073.

21.   Munch, E., et al., *Tough, bio-inspired hybrid materials.* Science, 2008. **322**(5907): p. 1516-1520.

22.   Walther, A., et al., *Large-area, lightweight and thick biomimetic composites with superior material properties via fast, economic, and green pathways.* Nano Letters, 2010. **10**(8): p. 2742-2748.

23.   Sumitomo, T., et al., *In situ transmission electron microscopy observation of reversible deformation in nacre organic matrix.* Journal of Materials Research, 2008. **23**(05): p. 1466-1471.

24.   Bezares, J., et al., *Macromolecular structure of the organic framework of nacre in Haliotis rufescens: Implications for growth and mechanical behavior.* Journal of Structural Biology, 2008. **163**(1): p. 61-75.

25.   Evans, A., et al., *Model for the robust mechanical behavior of nacre.* Journal of Materials Research, 2001. **16**(09): p. 2475-2484.

26.   Smith, B.L., et al., *Molecular mechanistic origin of the toughness of natural adhesives, fibres and composites.* Nature, 1999. **399**(6738): p. 761-763.

27.   Fantner, G.E., et al., *Sacrificial bonds and hidden length dissipate energy as mineralized fibrils separate during bone fracture.* Nature Materials, 2005. **4**(8): p. 612-616.

28.   Fantner, G.E., et al., *Sacrificial bonds and hidden length: unraveling molecular mesostructures in tough materials.* Biophysical Journal, 2006. **90**(4): p. 1411-1418.

29.   Bezares, J., et al., *Macromolecular structure of the organic framework of nacre in Haliotis rufescens: Implications for mechanical response.* Journal of Structural Biology, 2010. **170**(3): p. 484-500.

30.   Bezares, J., et al., *Core structure of aligned chitin fibers within the interlamellar framework extracted from Haliotis rufescens nacre. Part I: implications for growth and mechanical response.* Theoretical and Applied Mechanics, 2012. **39**(4): p. 343-363.

31.   Checa, A.G., et al., *Mineral bridges in nacre.* Journal of Structural Biology, 2011. **176**(3): p. 330-339.

32.   Song, F., et al., *Structural and mechanical properties of the organic matrix layers of nacre.* Biomaterials, 2003. **24**(20): p. 3623-3631.

33.   Lopez, M.I., et al., *Organic interlamellar layers, mesolayers and mineral nanobridges: Contribution to strength in abalone (Haliotis rufescence) nacre.* Acta Biomaterialia, 2014. **10**(5): p. 2056-2064.

34.   Barthelat, F., et al., *On the mechanics of mother-of-pearl: a key feature in the material hierarchical structure.* Journal of the Mechanics and Physics of Solids, 2007. **55**(2): p. 306-337.

35.   Mayer, G., *Rigid biological systems as models for synthetic composites.* Science, 2005. **310**(5751): p. 1144-1147.

36.   Meyers, M.A., et al., *Mechanical strength of abalone nacre: Role of the soft organic layer.* Journal of the Mechanical Behavior of Biomedical Materials, 2008. **1**(1): p. 76-85.

37.   Buehler, M.J., *Tu(r)ning weakness to strength.* Nano Today, 2010. **5**(5): p. 379-383.

38.   Gao, H., et al., *Materials become insensitive to flaws at nanoscale: Lessons from nature.* Proceedings of the National Academy of Sciences, 2003. **100**(10): p. 5597-5600.

39.   Dastjerdi, A.K., et al., *Cohesive behavior of soft biological adhesives: experiments and modeling.* Acta Biomaterialia, 2012. **8**(9): p. 3349-3359.

40.   Khayer Dastjerdi, et al., *The weak interfaces within tough natural composites: Experiments on three types of nacre.* Journal of the Mechanical Behavior of Biomedical Materials, 2013. **19**(0): p. 50-60.

41.   Zhang, S., *Fabrication of novel biomaterials through molecular self-assembly.* Nature Biotechnology, 2003. **21**(10): p. 1171-1178.

42.   Shen, X., et al., *Molecular cloning and characterization of lustrin A, a matrix protein from shell and pearl nacre of Haliotis rufescens.* Journal of Biological Chemistry, 1997. **272**(51): p. 32472-32481.

43.   Addadi, L., et al., *Mollusk shell formation: a source of new concepts for understanding biomineralization processes.* Chemistry-A European Journal, 2006. **12**(4): p. 980-987.

44.   Laaksonen, P., et al., *Genetic engineering in biomimetic composites.* Trends in Biotechnology, 2012. **30**(4): p. 191-197.

45.   Tsukamoto, D., et al., *Structure and expression of an unusually acidic matrix protein of pearl oyster shells.* Biochemical and Biophysical Research Communications, 2004. **320**(4): p. 1175-1180.

46.   Isowa, Y., et al., *A Comparative Study of the Shell Matrix Protein Aspein in Pterioid Bivalves.* Journal of Molecular Evolution, 2012. **75**(1-2): p. 11-18.

47.   Suzuki, M., et al., *An acidic matrix protein, Pif, is a key macromolecule for nacre formation.* Science, 2009. **325**(5946): p. 1388-1390.

48.   Falini, G., et al., *Control of aragonite or calcite polymorphism by mollusk shell macromolecules.* Science, 1996. **271**(5245): p. 67-69.

49.   Linder, M. and T.T. Teeri, *The roles and function of cellulose-binding domains.* Journal of Biotechnology, 1997. **57**(1): p. 15-28.

50.   Guillén, D., et al., *Carbohydrate-binding domains: multiplicity of biological roles.* Applied Microbiology and Biotechnology, 2010. **85**(5): p. 1241-1249.

51.   Igarashi, K., et al., *High speed atomic force microscopy visualizes processive movement of Trichoderma reesei cellobiohydrolase I on crystalline cellulose.* Journal of Biological Chemistry, 2009. **284**(52): p. 36186-36190.

52.   Igarashi, K., et al., *Traffic jams reduce hydrolytic efficiency of cellulase on cellulose surface.* Science, 2011. **333**(6047): p. 1279-1282.

53.   Carrard, G., et al., *Cellulose-binding domains promote hydrolysis of different sites on crystalline cellulose.* Proceedings of the National Academy of Sciences, 2000. **97**(19): p. 10342-10347.

54.   Asensio, J.L., et al., *Carbohydrate–aromatic interactions.* Accounts of Chemical Research, 2012. **46**(4): p. 946-954.

55.   Lehtiö, J., et al., *The binding specificity and affinity determinants of family 1 and family 3 cellulose binding modules.* Proceedings of the National Academy of Sciences, 2003. **100**(2): p. 484-489.

56. Nakari-Setälä, T., et al., *Genetic and biochemical characterization of the Trichoderma reesei hydrophobin HFBI.* European Journal of Biochemistry, 1996. **235**(1-2): p. 248-255.

57. Wösten, H.A., et al., *How a fungus escapes the water to grow into the air.* Current Biology, 1999. **9**(2): p. 85-88.

58. Linder, M., et al., *Surface adhesion of fusion proteins containing the hydrophobins HFBI and HFBII from Trichoderma reesei.* Protein Science, 2002. **11**(9): p. 2257-2266.

59. Linder, M.B., *Hydrophobins: proteins that self assemble at interfaces.* Current Opinion in Colloid & Interface Science, 2009. **14**(5): p. 356-363.

60. Ravi Kumar, M.N., *A review of chitin and chitosan applications.* Reactive and Functional Polymers, 2000. **46**(1): p. 1-27.

61. Sandberg, K.R., et al., *Microfibrillated cellulose*. 1984, Google Patents.

62. Pääkkö, M., et al., *Enzymatic hydrolysis combined with mechanical shearing and high-pressure homogenization for nanoscale cellulose fibrils and strong gels.* Biomacromolecules, 2007. **8**(6): p. 1934-1941.

63. Herrick, F.W., et al. *Microfibrillated cellulose: morphology and accessibility.* in *Journal of Applied Polymer Science: Applied Polymer Symposium;(United States)*. 1983: ITT Rayonier Inc., Shelton, WA.

64. Eichhorn, S., et al., *Review: current international research into cellulose nanofibres and nanocomposites.* Journal of Materials Science, 2010. **45**(1): p. 1-33.

65. Iwamoto, S., et al., *Elastic modulus of single cellulose microfibrils from tunicate measured by atomic force microscopy.* Biomacromolecules, 2009. **10**(9): p. 2571-2576.

66. Lu, P. and Y.-L. Hsieh, *Preparation and properties of cellulose nanocrystals: rods, spheres, and network.* Carbohydrate Polymers, 2010. **82**(2): p. 329-336.

67. Min, B.-M., et al., *Chitin and chitosan nanofibers: electrospinning of chitin and deacetylation of chitin nanofibers.* Polymer, 2004. **45**(21): p. 7137-7142.

68. Rolandi, M. and R. Rolandi, *Self-assembled chitin nanofibers and applications.* Advances in Colloid and Interface Science, 2014. **207**(0): p. 216-222.

69. Muzzarelli, R.A., *Chitin nanostructures in living organisms*, in *Chitin*. 2011, Springer. p. 1-34.

70. Ifuku, S. and H. Saimoto, *Chitin nanofibers: preparations, modifications, and applications.* Nanoscale, 2012. **4**(11): p. 3308-3318.

71. Zhao, H.-P., et al., *Ultrasonic technique for extracting nanofibers from nature materials.* Applied Physics Letters, 2007. **90**(7): p. -.

72. Ravi Kumar, M.N.V., *A review of chitin and chitosan applications.* Reactive and Functional Polymers, 2000. **46**(1): p. 1-27.

73. Ogawa, Y., et al., *Elastic modulus in the crystalline region and the thermal expansion coefficients of α-chitin determined using synchrotron radiated X-ray diffraction.* Carbohydrate Polymers, 2011. **83**(3): p. 1213-1217.

74. Nishino, et al., *Elastic modulus of the crystalline regions of chitin and chitosan.* Journal of Polymer Science Part B: Polymer Physics, 1999. **37**(11): p. 1191-1196.

75. Solomon, M.J. and P.T. Spicer, *Microstructural regimes of colloidal rod suspensions, gels, and glasses.* Soft Matter, 2010. **6**(7): p. 1391-1400.

76. Hoy, R.S. and M.O. Robbins, *Strain hardening of polymer glasses: Effect of entanglement density, temperature, and rate.* Journal of Polymer Science Part B: Polymer Physics, 2006. **44**(24): p. 3487-3500.

77.   Verho, T., et al., *Hydration and Dynamic State of Nanoconfined Polymer Layers Govern Toughness in Nacre-mimetic Nanocomposites.* Advanced Materials, 2013. **25**(36): p. 5055-5059.

78.   Benítez, A.J., et al., *Humidity and Multiscale Structure Govern Mechanical Properties and Deformation Modes in Films of Native Cellulose Nanofibrils.* Biomacromolecules, 2013, **14**(12), 4497-4506. .

79.   Torres-Rendon, J., et al., *Mechanical performance of macrofibers of cellulose and chitin nanofibrils aligned by wet-stretching: A critical comparison.* Biomacromolecules, 2014, **15**(7), 2709-2717.

80.   Saito, T., et al., *Homogeneous suspensions of individualized microfibrils from TEMPO-catalyzed oxidation of native cellulose.* Biomacromolecules, 2006. **7**(6): p. 1687-1691.

81.   Saito, T. and A. Isogai, *TEMPO-Mediated Oxidation of Native Cellulose. The Effect of Oxidation Conditions on Chemical and Crystal Structures of the Water-Insoluble Fractions.* Biomacromolecules, 2004. **5**(5): p. 1983-1989.

82.   Arola, S., et al., *The role of hemicellulose in nanofibrillated cellulose networks.* Soft Matter, 2013. **9**(4): p. 1319-1326.

83.   Henriksson, M., et al., *Cellulose nanopaper structures of high toughness.* Biomacromolecules, 2008. **9**(6): p. 1579-1585.

84.   Sehaqui, H., et al., *Strong and tough cellulose nanopaper with high specific surface area and porosity.* Biomacromolecules, 2011. **12**(10): p. 3638-3644.

85.   Sehaqui, H., et al., *Cellulose nanofiber orientation in nanopaper and nanocomposites by cold drawing.* ACS Applied Materials & Interfaces, 2012. **4**(2): p. 1043-1049.

86.   Liu, A., et al., *Clay nanopaper with tough cellulose nanofiber matrix for fire retardancy and gas barrier functions.* Biomacromolecules, 2011. **12**(3): p. 633-641.

87.   Wu, C.-N., et al., *Ultrastrong and high gas-barrier nanocellulose/clay-layered composites.* Biomacromolecules, 2012. **13**(6): p. 1927-1932.

88.   Jin, H., et al., *Ionically interacting nanoclay and nanofibrillated cellulose lead to tough bulk nanocomposites in compression by forced self-assembly.* Journal of Materials Chemistry B, 2013. **1**(6): p. 835-840.

89.   McKee, J.R., et al., *Molecular Engineering of Fracture Energy Dissipating Sacrificial Bonds Into Cellulose Nanocrystal Nanocomposites.* Angewandte Chemie International Edition, 2014. **126**(20): p. 5149-5153.

90.   Sen, D. and M.J. Buehler, *Structural hierarchies define toughness and defect-tolerance despite simple and mechanically inferior brittle building blocks.* Scientific Reports, 2011. **1**.

91.   Palmeri, M.J., et al., *Sacrificial bonds in stacked-cup carbon nanofibers: biomimetic toughening mechanisms for composite systems.* ACS Nano, 2010. **4**(7): p. 4256-4264.

92.   Laaksonen, P., et al., *Genetic engineering of biomimetic nanocomposites: diblock proteins, graphene, and nanofibrillated cellulose.* Angewandte Chemie International Edition, 2011. **50**(37): p. 8688-8691.

93.   Linder, M.B., et al., *Efficient purification of recombinant proteins using hydrophobins as tags in surfactant-based two-phase systems.* Biochemistry, 2004. **43**(37): p. 11873-11882.

94.   Linder, M., et al., *Characterization of a double cellulose-binding domain Synergistic high affinity binding to crystalline cellulose.* Journal of Biological Chemistry, 1996. **271**(35): p. 21268-21272.

95.   Laaksonen, P., et al., *Interfacial engineering by proteins: exfoliation and functionalization of graphene by hydrophobins.* Angewandte Chemie International Edition, 2010. **49**(29): p. 4946-4949.

96.   Jäger, I. and P. Fratzl, *Mineralized collagen fibrils: a mechanical model with a staggered arrangement of mineral particles.* Biophysical Journal, 2000. **79**(4): p. 1737-1746.

97.   Paakko, M., et al., *Enzymatic hydrolysis combined with mechanical shearing and high-pressure homogenization for nanoscale cellulose fibrils and strong gels.* Biomacromolecules, 2007. **8**(6): p. 1934-41.

98.   Teeri, T.T., et al., *Homologous domains in Trichoderma reesei cellulolytic enzymes: Gene sequence and expression of cellobiohydrolase II.* Gene, 1987. **51**(1): p. 43-52.

99.   Teeri, T., et al., *The molecular cloning of the major cellulase gene from Trichoderma reesei.* Nature Biotechnology, 1983. **1**(8): p. 696-699.

100.   Linder, M., et al., *The hydrophobins HFBI and HFBII from Trichoderma reesei showing efficient interactions with nonionic surfactants in aqueous two-phase systems.* Biomacromolecules, 2001. **2**(2): p. 511-517.

101.   Watanabe, T., et al., *The roles of the C-terminal domain and type III domains of chitinase A1 from Bacillus circulans WL-12 in chitin degradation.* Journal of Bacteriology, 1994. **176**(15): p. 4465-4472.

102.   Takeuchi, T., et al., *In vitro regulation of CaCO3 crystal polymorphism by the highly acidic molluscan shell protein Aspein.* FEBS Letters, 2008. **582**(5): p. 591-596.

103.   Mushi, N.E., et al., *Nanostructured membranes based on native chitin nanofibers prepared by mild process.* Carbohydrate Polymers, 2014. **112**(0): p. 255-263.

104.   Hoy, R.S. and C.S. O'Hern, *Viscoplasticity and large-scale chain relaxation in glassy-polymeric strain hardening.* Physical Review E, 2010. **82**(4): p. 041803.

105.   Keten, S., et al., *Nanoconfinement controls stiffness, strength and mechanical toughness of [beta]-sheet crystals in silk.* Nature Materials, 2010. **9**(4): p. 359-367.

106.   Nova, A., et al., *Molecular and nanostructural mechanisms of deformation, strength and toughness of spider silk fibrils.* Nano Letters, 2010. **10**(7): p. 2626-2634.

107.   Cranford, S.W., et al., *Nonlinear material behaviour of spider silk yields robust webs.* Nature, 2012. **482**(7383): p. 72-76.

108.   Shao, Z. and F. Vollrath, *Materials: Surprising strength of silkworm silk.* Nature, 2002. **418**(6899): p. 741-741.

109.   Burgert, I., et al., *Microtensile testing of wood fibers combined with video extensometry for efficient strain detection.* Holzforschung, 2003. **57**(6): p. 661-664.

110.   Geim, A.K. and K.S. Novoselov, *The rise of graphene.* Nature Materials, 2007. **6**(3): p. 183-191.

111.   Varjonen, S., et al., *Self-assembly of cellulose nanofibrils by genetically engineered fusion proteins.* Soft Matter, 2011. **7**(6): p. 2402-2411.

112. Stankovich, S., et al., *Graphene-based composite materials.* Nature, 2006. **442**(7100): p. 282-286.
113. Novoselov, K.S., et al., *Electric field effect in atomically thin carbon films.* Science, 2004. **306**(5696): p. 666-669.
114. Yang, X., et al., *Well-Dispersed Chitosan/Graphene Oxide Nanocomposites.* ACS Applied Materials & Interfaces, 2010. **2**(6): p. 1707-1713.
115. Liang, J., et al., *Molecular-level dispersion of graphene into poly (vinyl alcohol) and effective reinforcement of their nanocomposites.* Advanced Functional Materials, 2009. **19**(14): p. 2297-2302.
116. Kim, H., et al., *Graphene/Polymer Nanocomposites.* Macromolecules, 2010. **43**(16): p. 6515-6530.
117. Potts, J.R., et al., *Graphene-based polymer nanocomposites.* Polymer, 2011. **52**(1): p. 5-25.
118. Kuilla, T., et al., *Recent advances in graphene based polymer composites.* Progress in Polymer Science, 2010. **35**(11): p. 1350-1375.
119. Weiner, S. and L. Addadi, *Design strategies in mineralized biological materials.* Journal of Materials Chemistry, 1997. **7**(5): p. 689-702.

Enhanced Plastic Deformations of Nanofibrillated Cellulose Film by Adsorbed Moisture and Protein Mediated Interactions

Enhanced Plastic Deformations of Nanofibrillated Cellulose Film by Adsorbed Moisture and Protein-Mediated Interactions

Jani-Markus Malho,*,[†] Claudiane Ouellet-Plamondon,[‡] Markus Rüggeberg,[§,‖] Päivi Laaksonen,[†,⊥] Olli Ikkala,[#] Ingo Burgert,[§,‖] and Markus B. Linder*,[†,○]

[†]VTT Technical Research Centre of Finland, Tietotie 2, P.O. Box 1000, FI-02044, Espoo, Finland

[‡]ETH-Zürich, Inst. Bau-u. Infrastrukturmanagement, Stefano-Franscini-Platz 5, 8093 Zürich, Switzerland

[§]ETH-Zürich, Institute for Building Materials (IfB), Stefano-Franscini-Platz 3, 8093 Zürich, Switzerland

[‖]Empa, Applied Wood Materials Laboratory, Überlandstrasse 129, 8600 Dübendorf, Switzerland

[⊥]Aalto University, Department of Materials Science, P.O. Box 16200, FI-00076 Aalto, Finland

[#]Aalto University, Department of Applied Physics, P.O. Box 15100, FI-00076 Aalto, Finland

[○]Aalto University, Department of Biotechnology and Chemical Technology, P.O. Box 16100, FI-00076 Aalto, Finland

Ⓢ *Supporting Information*

ABSTRACT: Biological composites are typically based on an adhesive matrix that interlocks rigid reinforcing elements in fiber composite or brick-and-mortar assemblies. In nature, the adhesive matrix is often made up of proteins, which are also interesting model systems, as they are unique among polymers in that we know how to engineer their structures with atomic detail and to select protein elements for specific interactions with other components. Here we studied how fusion proteins that consist of cellulose binding proteins linked to proteins that show a natural tendency to form multimer complexes act as an adhesive matrix in combination with nanofibrillated cellulose. We found that the fusion proteins are retained with the cellulose and that the proteins mainly affect the plastic yield behavior of the cellulose material as a function of water content. Interestingly, the proteins increased the moisture absorption of the composite, but the well-known plastifying effect of water was clearly decreased. The work helps to understand the functional basis of nanocellulose composites as materials and aims toward building model systems for molecular biomimetic materials.

■ INTRODUCTION

Biological structural materials have inspired materials scientists to understand routes to combine high stiffness and strength with promoted toughness within a single material and, additionally, being sustainable and lightweight.[1,2] Classically, they seem to be conflicting properties, as stiffness and strength could be thought to need rigid and firmly interlocked reinforcing units, whereas toughness and suppressed catastrophic crack growth require ability to consume fracture energy using dissipative movements of the structural units.[3] Combining these requirements has turned out to be subtler than simply constructing composites or nanocomposites based on hard and soft domains.[4−6] Selected biological structural materials provide inspiration in this context, such as dragline silk, various shells, like nacre, and insect exoskeletons.[7] Silk is particularly instructive for the present case, as it is all-organic macromolecular system.[8,9] The reinforcing units are a few nanometers thick protein β-sheets as connected by more flexible protein domains consisting of folds that can efficiently consume mechanical deformation energy, involving sacrificial bonds and loopings that form hidden lengths.[10,11] To achieve

the feasible combination of mechanical properties, the different mechanisms work in synergy in parallel and balanced ways.

In synthetic materials, progress has been made, inspired by biological structural materials.[7,12−14] Tough inorganic/organic layered biomimetic composites have been produced by ice-templating and also using sequential spin coatings.[15,16] One-step self-assemblies of core−shell colloidal polymer-coated sheets have been shown to possess high strength and stiffness as well as stable crack growth under wet conditions.[4,17] Graphene has also been incorporated as the reinforcing unit by physical exfoliation into a native nanofibrillated cellulose matrix with improved ultimate tensile strength, stiffness, and toughness.[18]

Nanofibrillated cellulose (NFC) is nanofibrils with a high aspect ratio being typically a few micrometers in length and 5−20 nm in width possessing exceptional mechanical properties with high modulus of about 140 GPa and tensile strength even in the GPa range.[19,20] The cellulose nanofibrils play a key role

in the mechanical properties of plant cell walls, and their interplay with matrix polymers like hemicellulose, lignin, or pectin dictates the performance of the natural composites.[21,22] Being highly abundant and renewable, NFC is an interesting option for nanocomposites.[23] NFC is obtained by grinding and fluidization of, for example, pulp in combination with different pretreatments.[24−27] The interfibrillar interactions (mostly hydrogen bonds but also other weak interactions) are expected to dominate the behavior and structure of an unmodified native NFC film (nanopaper),[23] making it mechanically strong. Although the energy dissipation under mechanical loading can be high, the tightly packed random network structure shows typically brittle failure as cracks grow catastrophically upon deformation. One could speculate that this is due to the inability of the rigid colloidal level NFC fibrils to undergo dissipative relative movements to further consume mechanical energy. A trivial approach would be to expose the films to humidity, where the adsorbed water could plasticize the film. A more versatile approach could be to tune the interactions of the NFC by constructing different polymeric shells around the NFC cores.[28] So far, for several such approaches, the stress−strain curves in tensile measurements have been remarkably similar, with an initial elastic part and then a smooth yield-point manifested as a slope change and followed by plastic strain-stiffening. One report that deviates from this NFC performance pattern describes the introduction of surface modifications to introduce sacrificial bonds in cellulose nanocrystals, where the sacrificial bonds were based on acrylate polymer brushes, incorporating supramolecular ureidine pyrimidone groups and resulted in noncatastrophic crack propagation and substantial yielding by necking in tensile deformation.[29] In all above cases, the nanocellulose-based films and composites were prepared from solvent-dispersed phase upon solvent removal, which leads to jamming into highly packed solid phase with reduced dynamics. This phase can be regarded as colloidal glass. Deformations and colloidal dynamics of rod-like colloidal glasses are not yet fully understood.[30−32]

The above-mentioned arguments suggest in general pursuing toward finding protocols to tune the deformation characteristics of nanocellulose-based colloidal glasses by involving side chains with supramolecular binding units. Our hypothesis here was that proteins are, par excellence, macromolecules allowing supramolecular interactions based on tunable and specific protein folding-based interactions, as well as enabling non-specific hydrogen bonds. Here we selected a bifunctional fusion protein to decorate NFCs, consisting of groups allowing binding on NFC and a group that allows supramolecular binding to other similar groups. The supramolecular motif was selected to be class II hydrophobin (HFBI), which is known to have a high intermolecular binding constant. As the second motif we selected cellulose-binding domains, denoted here DCBD, where two CBDs were included due to their small size to allow a balanced structure with HFBI. The two types of motifs are connected by a linker. Therefore, the genetically produced "diblock protein" is here denoted as DCBD-HFBI.[33] Both HFBI and CBDs are found in nature, wherein HFBI is known to self-assemble on (hydrophobic) interfaces in aqueous environments[34] and the CBDs to have a high affinity to cellulose surfaces.[35] The behavior of DCBD-HFBI has earlier been studied within an NFC matrix[36] and utilized to exfoliate multilayered graphene in aqueous environment.[37] Furthermore, the same approach has been taken even further to mimic the structure of nacre[1] by combining native NFC fibrils, multi-layered graphene, and DCBD-HFBI in an aqueous environment via self-assembly, where the DCBD-HFBI was used as a glue to bind hydrophobic graphene flakes together with NFC fibrils.[38]

Here we study how the DCBD-HFBI functions within unmodified native NFC matrix to gain insights on the characteristics of the plastic deformation behavior. The initial amount of DCBD-HFBI in relation to the NFC was chosen to be high to saturate the binding on the NFC fibrils surfaces,[36] while the sample preparation should remove the unbound proteins from the film. To better understand interactions generated by the proteins and the NFC fibrils within a freestanding film, the effect of the degree of hydration on the mechanical behavior of unmodified NFC film and the NFC/DCBD-HFBI hybrid films is studied. Hydration is known to have major effects on the interactions of biomaterials and on the performance of composites.[17,39] More importantly, moisture is an inevitable part of materials in most of the systems highlighting the importance of understanding the role of water molecules within the system.

■ MATERIALS AND METHODS

Materials. NFC was processed by mechanical disintegration of bleached birch kraft pulp by 10 passes through a M7115 Fluidizer (Microfluidics Corp.), essentially according to previous reports.[26] The solid content of the prepared water dispersion was 1.9%. The bifunctional fusion protein consisted of one hydrophobin part linked to two different CBDs in series. The HFBI-hydrophobin from *Trichoderma reesei*[34] was used and the two CBDs were from the enzymes Cel7A (previously CBHI)[40] and Cel6A (previously CBHII),[41] also from *T. reesei*. These modules of the proteins were connected by polypeptide linker regions, as previously reported.[33] The abbreviation DCBD-HFBI is used for the fusion protein. The fusion protein was produced by recombinant means in *T. reesei* and purified by aqueous two-phase extraction, as described previously.[33] The protein was then purified by preparative reversed phase high performance liquid chromatography (RP-HPLC) using a water acetonitrile gradient with 0.1% trifluoroacetic acid. The identity and concentration were verified by amino acid analysis. Mass spectroscopy was additionally used to verify the identity. The proteins were lyophilized after purification.

Film Preparation. NFC dispersions were diluted in Milli-Q water (mQ) so that the concentration was 4.0 gL^{-1} based on the weight mass of the NFC batch. DCBD-HFBI was weighted in a plastic tube and diluted in mQ to concentration of 4.0 gL^{-1}. The NFC and DCBD-HFBI were mixed so that both NFC and DCBD-HFBI had the concentration of 2.0 gL^{-1} (108 μM) in the final volume of 2.4 mL. With these starting conditions it is calculated using that at equilibrium the bound amount is 19 μmol/g and the free concentration is 69 μM (K_d= 2.4 μM, B_{max} 20 μmol/g, M_w = 18436 g/mol).[36] Before vacuum filtration, the dispersions were sonicated by 2000 J per 2.4 mL dispersion via tip sonicator (Vibra-Cell VCX 750, Sonics and Materials Inc.) to enhance the dispersity of the fibrils and NFC/DCBD-HFBI mixtures. The used power was 40% of the full output power. The dispersions were vacuum filtrated using Durapore membranes (GVWP, 0.22 μm, Millipore, U.S.A.) and an O-ring to determine the diameter of the films. A press with a 300 g load for 10 min was applied to prevent wrinkling. At the end, the films were dried overnight in an oven at +60 °C.

Relative Humidity Control. The microtensile tests at 85% and 50% relative humidity (RH) were conducted in a controlled desiccator monitored with a hygrometer Testo 608-H1. At 85% RH, samples were conditioned in a controlled humidity room until the test time. The relative humidity of the desiccator was achieved by a homemade system of flowing air heated and humidified by boiling water on a hot plate. Potassium chloride contributed to maintain the relative humidity of the desiccator. For the drier conditions (25%RH and 5%RH),

samples were dried in the oven at 60 °C and conditioned in a desiccator equipped with a compressed air line. The relative humidity control was achieved by varying the pressure delivered to the desiccator from 0 to 1 bar with potassium acetate.

Scanning Electron Microscopy. The thickness of the films was measured with a scanning electron microscope (SEM) FEI Quanta 200F (U.S.A.), both in low and high vacuum conditions. A thin Au layer was sputtered on the samples in high vacuum.

Tensile Testing. Tensile test were conducted using a microtensile testing device. A detailed description of this device can be found in Burgert et al.[42] The high precision linear stage was an Owis Limes 60 featuring a two-phase step motor. The controller was a PI micos Pollux type 1. Tensile tests were carried out using a 50 N load cell with a nominal strain rate of 8 μm·s^{-1}. The gauge length was set to 10 mm for all of the samples. At least four specimens were measured from each sample. Sample sizes were 2.0 cm × 2.0 mm × 8−14 μm, length, width, and thickness, respectively. Sample thicknesses were measured using SEM. Here, at least six measurements from a cross-section of a sample were measured to calculate average value for thickness. The widths were measured with a digital slide gauge (Digimatic, Mitutoyo). The mechanical tensile tester was placed inside desiccator during the measurements, so the measurements could be done in a controlled humidity. Depending on the desired relative humidity, dry air or humid air was pumped into the desiccator. For the measurements at 50%RH and 85%RH samples were first stored overnight in humidity controlled rooms. Before testing they were moved to the humidity controlled desiccator. Samples that were measured at 5%RH were taken directly from the oven to the dry desiccator and tested. Samples measured at 25%RH were taken from oven and equilibrated to 25% RH in a desiccator prior to testing.

FT-IR Spectroscopy. The FT-IR spectroscopy measurements were performed using a PerkinElmer Spectrum 100 in the 4000 to 600 cm^{-1} range with a resolution of 4 cm^{-1}. The resulting spectra represent averages of 50 scans. They were baseline-corrected for CO_2 and water.

Dynamic Vapor Sorption (DVS). Moisture sorption and desorption isotherms of one unmodified NFC film and one NFC/DCBD-HFBI film were generated with a VTI-SA Vapor Sorption Analyzer (TA Instruments). Measurements were performed at 10, 25, 50, and 85% relative humidity. The samples were initially dried at 105 °C for 60 min. Equilibrium was assumed when there was no mass change more than 0.0010% in 2 min with the condition that equilibrium must be reached within 300 min.

TGA. The thermogravimetric analysis was conducted with a TGA Q50 (TA Instruments). A 2.2 mg sample was placed in a platinum pan and heated 10 °C/min until 1000 °C in a nitrogen current. The thermogravimetric (TG) curves express the percent mass loss as a function of temperature and the derivative TG show the mass loss rate as a function of temperature.

■ RESULTS AND DISCUSSION

The structural and chemical composition of the NFC/DCBD-HFBI composites was qualitatively evidenced with FTIR and TGA. First, FTIR spectra of the NFC/DCBD-HFBI films show two additional bands in comparison to the spectra of the pure NFC films which confirm the presence of protein in the modified films. One band at 1639 cm^{-1} represents an amide I band of protein associated with the C═O vibration in antiparallel β-sheets,[43] and the other band at 1518 cm^{-1} corresponds to an amide II band associated with the N−H bending vibration and the C−N stretching vibration (see the Supporting Information, Figure S1). Second, the TGA of the NFC/DCBD-HFBI film showed a pronounced shoulder in the spectrum, which corresponds to the degradation of the protein (see Supporting Information, Figure S2). Films containing protein were approximately 20−40% thicker than controls not containing protein, indicating a 70−80% volume fraction of NFC in the protein-containing films.

Furthermore, the water vapor absorption−desorption properties of an unmodified NFC and NFC/DCBD-HFBI films were different. The masses of films were determined upon exposure to different relative humidity conditions and the water uptake was evaluated (Figure 1). The results show that NFC/
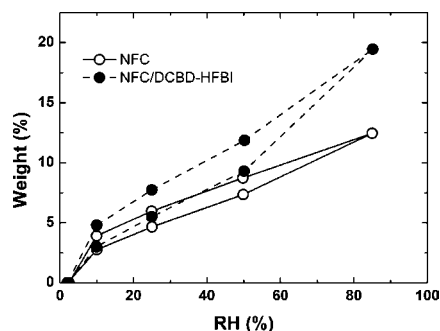

Figure 1. Water vapor adsorption−desorption isotherms of unmodified NFC and NFC/DCBD-HFBI films. The *y*-axis shows relative change.

DCBD-HFBI films adsorbed more moisture than unmodified NFC films over the entire range of humidity from 5 to 85% RH. Especially at high humidity levels, the differences between the two films were significant. In addition, the TGA measurements displayed higher amount of evaporated moisture for the NFC/DCBD-HFBI film (see Supporting Information, Table 1).

Tensile testing of both unmodified NFC film and protein-containing NFC/DCBD-HFBI film were performed at four different humidities: 5%RH, 25%RH, 50%RH, and 85%RH. In Figure 2, representative stress−strain curves are shown. The average values for calculated parameters are shown in Figure 3. In all cases, the shape of the stress−strain curves consisted of an initial elastic part, then a yield point where the slope changed, and following that, a plastic region at high strains that showed strain stiffening.

Figure 2a shows the effect of humidity on the tensile properties of unmodified NFC film. At 5%RH, the maximum stress was near 250 MPa, whereas the strain-to-failure was relatively small (5.5%). We found that, upon increasing moisture content, the yield point became more distinct at approximately the same strain values, and that the yield stress became substantially reduced in humid samples. Notably the plastic strain region was considerably increased. For 85%RH, the strain was relatively high (17%) as was the ultimate stress (200 MPa). As a general trend, the Young's moduli decreased with absorbed humidity. A pronounced effect of humidity was seen in the plastic region, where the slope of the stress−strain curve was significantly reduced upon increased moisture (see Figure 5). The values for the slopes were calculated directly after the yield points. This signifies the plasticizing effect of water to allow dissipative mutual sliding of the NFC fibrils. The dissipation was further investigated using cyclic mechanical testing in the plastic region (Figure 4) showing that the elongation does not recover after the yield-point. Finally, we remark that upon tearing both the protein containing and the unmodified NFC films qualitatively showed catastrophic crack propagation at all humidity levels.
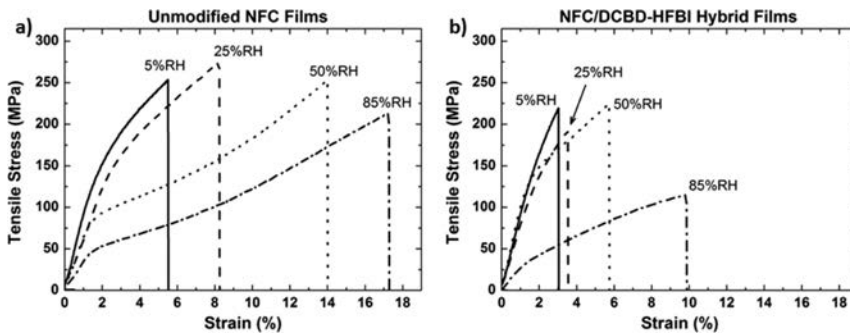
Figure 2. Representative stress−strain curves for (a) unmodified NFC and (b) NFC/DCBD-HFBI hybrid films in four different humidities. Solid lines represent measurements at 5%RH, dashed lines at 25%RH, dotted lines at 50%RH, and dash dotted lines at 85%RH.
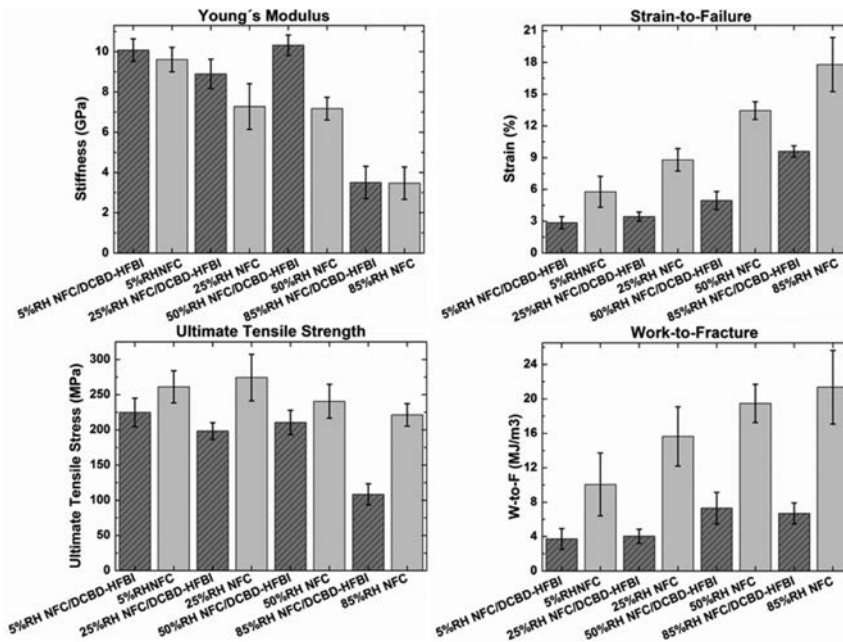

Figure 3. Young's modulus, strain-to-failure, ultimate tensile strength, and work-to-fracture of the noncyclic measurements for the unmodified NFC films and the NFC/DCBD-HFBI hybrid films at four different humidities with standard deviation. The values for unmodified NFC film are shown with gray bars and the values for the NFC/DCBD-HFBI hybrid film in dark gray lined columns.

Both quantitatively and qualitatively there were significant differences in the stress−strain curves of NFC/DCBD-HFBI and unmodified NFC films, see Figure 2. At all humidity levels, the strain values for NFC/DCBD-HFBI were less than those of unmodified NFC, and notably at 85%RH, the ultimate strength was only half of that of unmodified NFC. In the plastic zone, the initial slope in the plastic region increased particularly strongly upon reduced water content, Figure 5b,d.

The same data show that the plastifying effect of water is lower in the protein-containing films than in those without proteins. This is in interesting contrast to the observation that the protein-containing samples actually adsorbed more water in the sorption measurements (Figure 1). The slopes of the stress−strain curves in the plastic region for films with and

without protein showed the largest relative difference around 50% RH, being double at this range (Figure 5b,d). The plastifying effect of water is interpreted in terms of water molecules competing with interfibril hydrogen bonding, which allows fibrils to slip more easily past each other. The presence of protein molecules leads to a situation where more water can be accommodated in the structure, but the effect of water as a plasticizer is decreased. This apparent contradiction may be explained by considering the natural environment of proteins. Proteins naturally function in aqueous environments but rely on hydrogen bonding for interactions. To do so, they rely on precise structures, which are able to form multivalent, mutually strengthening, synergistic bonding. At the same time, they offer many hydration sites around their structures. Therefore, the
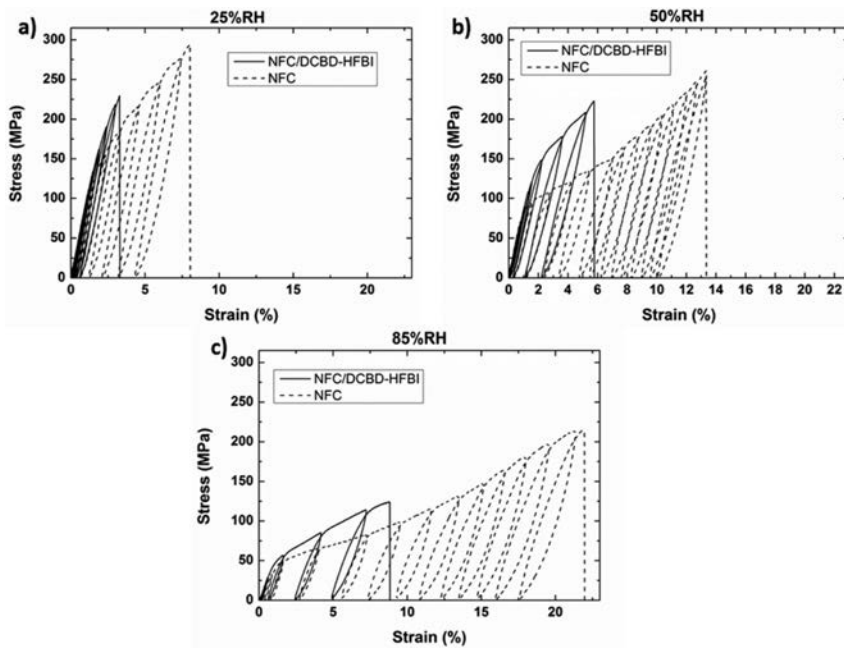
Figure 4. Representative stress−strain curves of the unmodified NFC (drawn as dashed black line) and NFC/DCBD-HFBI films (solid black line) from cyclic tensile tests measured at 25%RH, 50%RH, and 85%RH (a−c, respectively).

ability of the protein-containing films to both absorb more water and simultaneously resist the plasticizing effect may be a logical consequence of the natural structure and function of the embedded proteins.

Since the protein matrix affected the material mainly through interaction during plastic deformation, while the effect was relatively minor for the elastic modulus the results suggest that we only partly can rationalize results through a model where the protein would act as an adhesive matrix between fibrils. First, we conclude that there is a clear effect of proteins as an adhesive element based on the arguments presented above. However, since the elastic modulus remained mostly unaffected by the protein addition we hypothesize that the initial elastic stiffness of the structures is dominated by other interactions. A likely reason is the entanglement of the long NFC fibrils, and involving bonding not immediately affected by the protein, that is, a situation where in a velcro-like manner hooks and loops are entangled. Such mechanical interlocking and entanglement is expected because of the very long aspect ratios found in NFC fibrils. Only when the strain leads to irreversible transformations in the entangled structures, that is, during plastic deformation, do we note a role of the protein. This suggests that in protein containing samples the rearrangements lead to increased interactions between fibrils over higher length scales. The relatively large dimensions of the protein perhaps allow a more efficient spanning of the space in between the fibrils. A plausible mechanism for linkage is suggested in Figure 6. According to this model, the CBD-parts adhere to the cellulose and interchain linkage is mediated by HFBI-multimerization interactions or by bridges formed by the linker between cellulose binding domains. The latter case may be less favorable

since we know that the linkage of CBD-domains leads to a higher affinity in binding. The reason for this increase in affinity lies in the lower entropy cost for the binding of the second domain once the first one has bound. This reduction in entropy cost is expected to be more beneficial if binding sites were close to each other, that is, on the same fibril rather than separated on different fibrils. During the later stages of plastic deformation, the protein containing material shows less ultimate stress compared to the nonprotein controls. It is also noted that during plastic deformation the samples without protein showed a characteristic concave-up shape of the stress−strain curve. This is indicative of a strain-stiffening due to reorganization and sliding of fibrils relative to each other. The effect is seen in both static and cyclic testing. This effect is not observed in the protein-containing samples. We can interpret this effect in terms of a resistance to plastic deformation caused by the protein. Because this increased resistance to deformation also leads to less stress-relieving rearrangements, it is also logical that the ultimate strength of the protein containing samples is somewhat decreased. This is because the protein apparently does not allow sliding of fibrils to relieve local stress concentration, and therefore lead to higher local concentrations of stress and subsequent rupture of fibrils.

As a note, however, we see that for the samples measured at 50% RH the protein containing films show a pronounced stiffness. At this humidity there is also a clearly elevated yield point, indicating some sort of increased molecular interaction between fibrils. This is an interesting observation that somewhat deviates from the overall trends observed in the samples and for which the significance is not clear. It may be
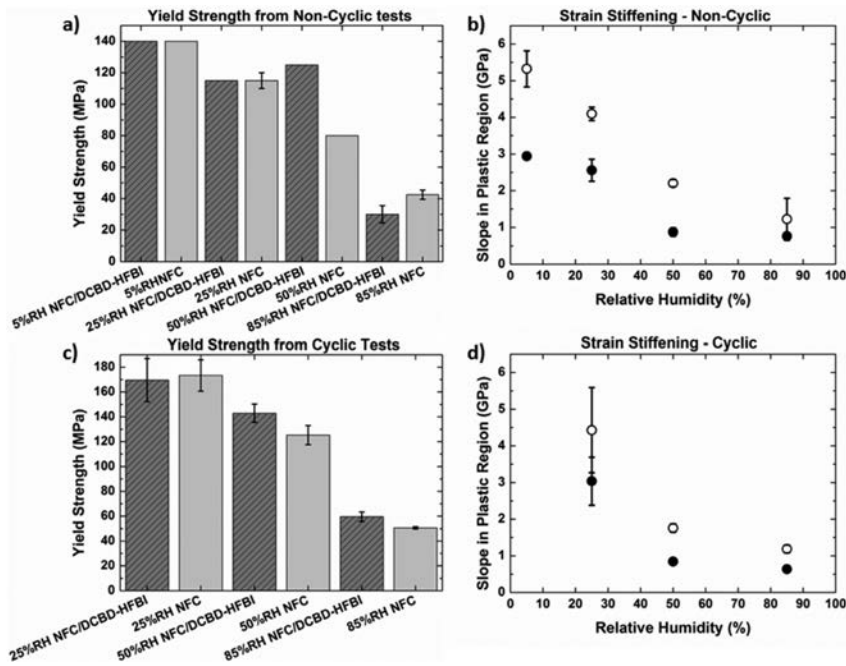
Figure 5. Average yield stress values from (a) noncyclic measurements and (c) cyclic measurements for unmodified NFC and NFC/DCBD-HFBI films in four different humidities. (b) The calculated slope in the plastic region from noncyclic measurements after the yield point at 5%RH, 25%RH, 50%RH, and 85%RH, respectively, as a function of relative humidity, where unmodified NFC film is drawn with black round dots and the NFC/DCBD-HFBI hybrid film with hollow black round circles. (d) The slope in the plastic region at 25%RH, 50%RH, and 85%RH, respectively, as a function of relative humidity in the cyclic measurements, where unmodified NFC film is drawn with filled round circles and the NFC/DCBD-HFBI hybrid film with nonfilled black circles. All results are shown with standard deviation.

that, at this particular humidity, there is an optimal resistance of protein containing samples for the plastifying effect of water.

Qualitatively, the present stress–strain curves resemble those of several glassy polymers. It is interesting to contemplate the differences between polymeric molecular glasses and nanofibrillar colloidal glasses. In polymeric glasses, the initial part at low strains is elastic, allowing complete recovery of the initial structure after removing the deformation forces. After the yield point, the deformation starts to be nonaffine, where the polymeric chains start sliding past each other, thus, consuming energy. In the process, the material starts to be slightly anisotropic. Strain stiffening is more pronounced for long polymers, obviously as under deformation the chains become slightly stretched due to larger number of entanglements in longer polymers. The strain stiffening is an activated process, where the strain stiffening is higher at high strains and becomes smaller upon increased temperature, obviously as the chains can slide more easily past each other's at higher temperatures, with higher free volume. It has been hypothesized that in polymeric glasses, large strain stiffening is connected to reduced strain location and can lead to promoted toughness.[44] In polymeric glasses, there are still segmental dynamics, after the main dynamics has been arrested in glass transition. In rod-like colloidal glasses, one could expect similarities but also differences. The colloidal units obviously have more defined geometrical shapes, and therefore the packing reasons leading to arrested dynamics may be more pronounced and the

secondary relaxations more suppressed. An important difference between the polymeric glasses and the present colloidal glasses is the aspect ratio, which in the NFC-based colloidal glasses is substantially smaller. This may require well-balanced supramolecular interactions between the NFC fibrils, which still remains a challenge for future work.

■ CONCLUSIONS

This work aims to control fracture energy dissipation in NFC-based films by using bifunctional genetically prepared fusion proteins, providing adsorption on NFC (cellulose binding domain, CBD) and supramolecular binding between the proteins (hydrophobin, HFBI). DCBD-HFBI fusion protein affects the properties of nanocellulose films. The resulting nanocellulose/protein colloidal glasses show a distinct yielding and a steeper slope in the plastic region. Still, toughness in the form of suppressed catastrophic crack growth could not be achieved. Increased water content caused easier sliding of fibrils in NFC-films, that is, water plasticized the films. Proteins in the films lead to an increased uptake of water but also resulted in a reduction of the amount of water that was available for sliding of fibrils. This study supports a central role of proteins in adhesive matrix functions in natural composites, but also suggests that the material properties are highly dependent on balanced structural arrangements at all length scales.
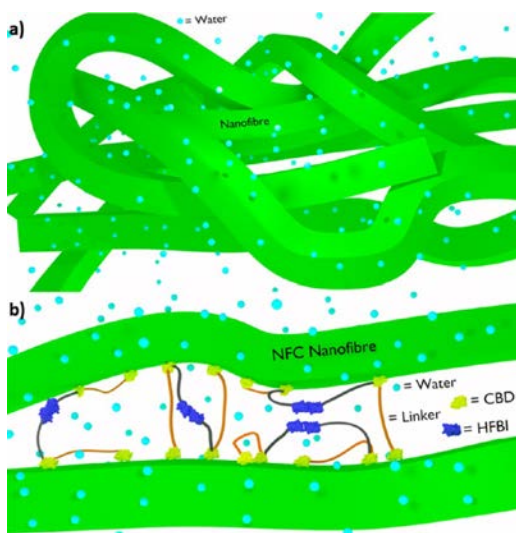
Figure 6. Schematic illustrations of (a) a highly entangled NFC fibrils matrix and (b) of the possible molecular structures of the NFC/DCBD-HFBI hybrid film. The most probable structure that would result in the modified mechanical performance is that the HFBI domains bind to each other while both of the CBDs in a DCBD-HFBI molecule would bind to the same NFC fibril causing molecular cross-linking of the NFC network. Another possibility is that the hydrophobins are bound to each other as in the first scenario, but the CBD domains bind separate NFC fibrils, where molecular cross-linking of the NFC fibrils would occur through CBDs and the HFBI domains. Both scenarios are possible and may take place at the same time, although cross-linking through a DCBD domains seems more unlikely based on previous studies.[35] Water molecules are highlighted with light blue dots. Hemicellulose is not included to the image due to the fact that no reliable information on the location of hemicelluloses is known to our understanding; furthermore both films contain the same amount of hemicellulose since the same batch of NFC was used for this study. Based on the mechanical tensile testing water molecules seem to be able to penetrate both unmodified NFC film and the NFC/DCBD-HFBI hybrid film affecting the mechanical performances. However, the DCBD-HFBI is likely to be able to outcompete the water molecules within the matrix, which is seen in the altered hydration dependent mechanical behavior.

◼ ASSOCIATED CONTENT

Ⓢ Supporting Information

FT-IR spectra, cyclic tensile test results, and TGA data. This material is available free of charge via the Internet at http://pubs.acs.org.

◼ AUTHOR INFORMATION

Corresponding Authors
*E-mail: jani-markus.malho@vtt.fi.
*E-mail: markus.linder@aalto.fi.

Notes
The authors declare no competing financial interest.

◼ ACKNOWLEDGMENTS

◼ REFERENCES

(1) Espinosa, H. D.; Rim, J. E.; Barthelat, F.; Buehler, M. J. Merger of structure and material in nacre and bone: perspectives on de novo biomimetic materials. *Prog. Mater. Sci.* **2009**, *54*, 1059−1100.

(2) Weiner, S.; Addadi, L. Design strategies in mineralized biological materials. *J. Mater. Chem.* **1997**, *7*, 689−702.

(3) Song, F.; Soh, A.; Bai, Y. Structural and mechanical properties of the organic matrix layers of nacre. *Biomaterials* **2003**, *24*, 3623−3631.

(4) Walther, A.; Bjurhager, I.; Malho, J.-M.; Pere, J.; Ruokolainen, J.; Berglund, L. A.; Ikkala, O. Large-area, lightweight and thick biomimetic composites with superior material properties via fast, economic, and green pathways. *Nano Lett.* **2010**, *10*, 2742−2748.

(5) Rosilo, H.; Kontturi, E.; Seitsonen, J.; Kolehmainen, E.; Ikkala, O. Transition to reinforced state by percolating domains of intercalated brush-modified cellulose nanocrystals and poly(butadiene) in cross-linked composites based on thiol−ene click chemistry. *Biomacromolecules* **2013**, *14*, 1547−1554.

(6) Tang, Z.; Kotov, N. A.; Magonov, S.; Ozturk, B. Nanostructured artificial nacre. *Nat. Mater.* **2003**, *2*, 413−418.

(7) Meyers, M. A.; Chen, P.-Y.; Lin, A. Y.-M.; Seki, Y. Biological materials: structure and mechanical properties. *Prog. Mater. Sci.* **2008**, *53*, 1−206.

(8) Hardy, J.; Scheibel, T. Silk-inspired polymers and proteins. *Biochem. Soc. Trans.* **2009**, *37*, 677−681.

(9) Nova, A.; Keten, S.; Pugno, N. M.; Redaelli, A.; Buehler, M. J. Molecular and nanostructural mechanisms of deformation, strength and toughness of spider silk fibrils. *Nano Lett.* **2010**, *10*, 2626−2634.

(10) Keten, S.; Xu, Z.; Ihle, B.; Buehler, M. J. Nanoconfinement controls stiffness, strength and mechanical toughness of beta-sheet crystals in silk. *Nat. Mater.* **2010**, *9*, 359−367.

(11) Keten, S.; Buehler, M. J. Nanostructure and molecular mechanics of spider dragline silk protein assemblies. *J. R. Soc., Interface* **2010**, *7*, 1709−1721.

(12) Buehler, M. J. Turning weakness to strength. *Nano Today* **2010**, *5*, 379−383.

(13) Dunlop, J. W.; Weinkamer, R.; Fratzl, P. Artful interfaces within biological materials. *Mater. Today* **2011**, *14*, 70−78.

(14) Meyers, M. A.; McKittrick, J.; Chen, P.-Y. Structural biological materials: critical mechanics-materials connections. *Science* **2013**, *339*, 773−779.

(15) Bonderer, L. J.; Studart, A. R.; Gauckler, L. J. Bioinspired design and assembly of platelet reinforced polymer films. *Science* **2008**, *319*, 1069−1073.

(16) Munch, E.; Launey, M. E.; Alsem, D. H.; Saiz, E.; Tomsia, A. P.; Ritchie, R. O. Tough, bioinspired hybrid materials. *Science* **2008**, *322*, 1516−1520.

(17) Verho, T.; Karesoja, M.; Das, P.; Martikainen, L.; Lund, R.; Alegría, A.; Walther, A.; Ikkala, O. Hydration and dynamic state of nanoconfined polymer layers govern toughness in nacre-mimetic nanocomposites. *Adv. Mater.* **2013**, *25*, 5055−5059.

(18) Malho, J. M.; Laaksonen, P.; Walther, A.; Ikkala, O.; Linder, M. B. Facile method for stiff, tough, and strong nanocomposites by direct exfoliation of multilayered graphene into native nanocellulose matrix. *Biomacromolecules* **2012**, *13*, 1093−1099.

(19) Eichhorn, S.; Dufresne, A.; Aranguren, M.; Marcovich, N.; Capadona, J.; Rowan, S.; Weder, C.; Thielemans, W.; Roman, M.; Renneckar, S. Review: current international research into cellulose nanofibres and nanocomposites. *J. Mater. Sci.* **2010**, *45*, 1−33.

(20) Iwamoto, S.; Kai, W.; Isogai, A.; Iwata, T. Elastic modulus of single cellulose microfibrils from tunicate measured by atomic force microscopy. *Biomacromolecules* **2009**, *10*, 2571−2576.

(21) Keckes, J.; Burgert, I.; Frühmann, K.; Müller, M.; Kölln, K.; Hamilton, M.; Burghammer, M.; Roth, S. V.; Stanzl-Tschegg, S.; Fratzl, P. Cell-wall recovery after irreversible deformation of wood. *Nat. Mater.* **2003**, *2*, 810−813.

(22) Fratzl, P.; Burgert, I.; Gupta, H. S. On the role of interface polymers for the mechanics of natural polymeric composites. *Phys. Chem. Chem. Phys.* **2004**, *6*, 5575−5579.

(23) Klemm, D.; Kramer, F.; Moritz, S.; Lindström, T.; Ankerfors, M.; Gray, D.; Dorris, A. Nanocelluloses: a new family of nature-based materials. *Angew. Chem., Int. Ed.* **2011**, *50*, 5438−5466.

(24) Turbak, A. F.; Snyder, F. W.; Sandberg, K. R. Microfibrillated cellulose, a new cellulose product: properties, uses, and commercial potential. *J. Appl. Polym. Sci.: Appl. Polym. Symp.*; ITT Rayonier Inc., Shelton, WA, 1983; pp 815−827.

(25) Henriksson, M.; Henriksson, G.; Berglund, L.; Lindström, T. An environmentally friendly method for enzyme-assisted preparation of microfibrillated cellulose (MFC) nanofibers. *Eur. Polym. J.* **2007**, *43*, 3434−3441.

(26) Pääkkö, M.; Ankerfors, M.; Kosonen, H.; Nykänen, A.; Ahola, S.; Österberg, M.; Ruokolainen, J.; Laine, J.; Larsson, P. T.; Ikkala, O.; Lindstrom, T. Enzymatic hydrolysis combined with mechanical shearing and high-pressure homogenization for nanoscale cellulose fibrils and strong gels. *Biomacromolecules* **2007**, *8*, 1934−1941.

(27) Saito, T.; Nishiyama, Y.; Putaux, J.-L.; Vignon, M.; Isogai, A. Homogeneous suspensions of individualized microfibrils from TEMPO-catalyzed oxidation of native cellulose. *Biomacromolecules* **2006**, *7*, 1687−1691.

(28) Larsson, P. A.; Berglund, L. A.; Wågberg, L. Ductile all-cellulose nanocomposite films fabricated from core−shell structured cellulose nanofibrils. *Biomacromolecules* **2014**, *15*, 2218−2223.

(29) McKee, J. R.; Huokuna, J.; Martikainen, L.; Karesoja, M.; Nykänen, A.; Kontturi, E.; Tenhu, H.; Ruokolainen, J.; Ikkala, O. Molecular engineering of fracture energy dissipating sacrificial bonds into cellulose nanocrystal nanocomposites. *Angew. Chem., Int. Ed.* **2014**, *126*, 5149−5153.

(30) Hoy, R. S.; Robbins, M. O. Strain hardening of polymer glasses: effect of entanglement density, temperature, and rate. *J. Polym. Sci., Part B: Polym. Phys.* **2006**, *44*, 3487−3500.

(31) Hoy, R. S.; O'Hern, C. S. Viscoplasticity and large-scale chain relaxation in glassy-polymeric strain hardening. *Phys. Rev. E* **2010**, *82*, 041803−1−041803−10.

(32) Solomon, M. J.; Spicer, P. T. Microstructural regimes of colloidal rod suspensions, gels, and glasses. *Soft Matter* **2010**, *6*, 1391−1400.

(33) Linder, M. B.; Qiao, M.; Laumen, F.; Selber, K.; Hyytiä, T.; Nakari-Setälä, T.; Penttilä, M. E. Efficient purification of recombinant proteins using hydrophobins as tags in surfactant-based two-phase systems. *Biochemistry* **2004**, *43*, 11873−11882.

(34) Nakari-Setälä, T.; Aro, N.; Kalkkinen, N.; Alatalo, E.; Penttilä, M. Genetic and biochemical characterization of the *Trichoderma reesei* hydrophobin HFBI. *Eur. J. Biochem.* **1996**, *235*, 248−255.

(35) Linder, M.; Salovuori, I.; Ruohonen, L.; Teeri, T. T. Characterization of a double cellulose-binding domain synergistic high affinity binding to crystalline cellulose. *J. Biol. Chem.* **1996**, *271*, 21268−21272.

(36) Varjonen, S.; Laaksonen, P.; Paananen, A.; Valo, H.; Hähl, H.; Laaksonen, T.; Linder, M. B. Self-assembly of cellulose nanofibrils by genetically engineered fusion proteins. *Soft Matter* **2011**, *7*, 2402−2411.

(37) Laaksonen, P.; Kainlauri, M.; Laaksonen, T.; Shchepetov, A.; Jiang, H.; Ahopelto, J.; Linder, M. B. Interfacial engineering by proteins: exfoliation and functionalization of graphene by hydrophobins. *Angew. Chem., Int. Ed.* **2010**, *49*, 4946−4949.

(38) Laaksonen, P.; Walther, A.; Malho, J. M.; Kainlauri, M.; Ikkala, O.; Linder, M. B. Genetic engineering of biomimetic nanocomposites: diblock proteins, graphene, and nanofibrillated cellulose. *Angew. Chem., Int. Ed.* **2011**, *50*, 8688−8691.

(39) Johnson, M.; Walter, S.; Flinn, B.; Mayer, G. Influence of moisture on the mechanical behavior of a natural composite. *Acta Biomater.* **2010**, *6*, 2181−2188.

(40) Teeri, T.; Salovuori, I.; Knowles, J. The molecular cloning of the major cellulase gene from *Trichoderma reesei*. *Nat. Biotechnol.* **1983**, *1*, 696−699.

(41) Teeri, T. T.; Lehtovaara, P.; Kauppinen, S.; Salovuori, I.; Knowles, J. Homologous domains in *Trichoderma reesei* cellulolytic enzymes: gene sequence and expression of cellobiohydrolase II. *Gene* **1987**, *51*, 43−52.

(42) Burgert, I.; Frühmann, K.; Keckes, J.; Fratzl, P.; Stanzl-Tschegg, S. E. Microtensile testing of wood fibers combined with video extensometry for efficient strain detection. *Holzforschung* **2003**, *57*, 661−664.

(43) Barth, A. Infrared spectroscopy of proteins. *Biochim. Biophys. Acta, Bioenerg.* **2007**, *1767*, 1073−1101.

(44) Jean-Louis Barrat, J. B.; Lyulin, A. Molecular dynamics simulations of glassy polymers. *arXiv* **2010**, 1002.2065.

Enhanced Plastic Deformations of Nanofibrillated Cellulose Film by Adsorbed Moisture and Protein Mediated Interactions

Jani-Markus Malho, Claudiane Ouellet-Plamondon, Markus Rüggeberg, Päivi Laaksonen, Olli Ikkala, Ingo Burgert and Markus B. Linder
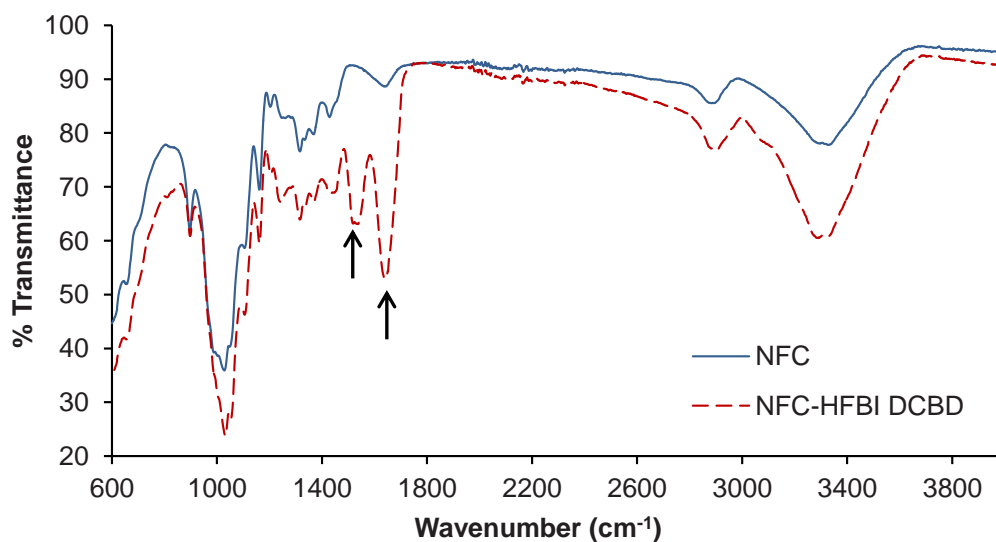
Figure S1. FTIR measurements of the unmodified NFC film and the NFC/DCBD-HFBI hybrid film. The arrows show Amide I band at 1639 cm^{-1} associated with the C=O vibration in antiparallel beta-sheets and an Amide II band at 1518 cm^{-1} associated with the N-H bending vibration and the C-N stretching vibration confirming the presence of the fusion protein in the modified NFC film.

TGA measurements were performed on NFC films, NFC/DCBD-HFBI films and the DCBD-HFBI protein alone (figure S2). Three maxima are visible in the derivative thermogravimetric (DTG) curves. The first maximum below 100°C corresponds to the evaporation of the adsorbed water. The evaporation of the adsorbed water was 3.3% for the NFC, 5.3% for the NFC-Protein and 6% for the pure DCBD-HFBI (Table 1). The higher amount of evaporated water for the NFC-DCBD-HFBI

film confirms the results of the DVS that the water content of the NFC/DCBD-HFBI film is higher than that of the unmodified NFC film at a certain relative humidity. The protein shows a second maximum at 300°C corresponding to its degradation. Both films show a second maximum at 350°C corresponding to the depolymerization, dehydration and decomposition of the glycosyl units. Hereby, the sample with the protein shows a shoulder at 300°C, which corresponds to the degradation of the fusion protein. The third maximum corresponds to the formation of charred residue and is more apparent in the protein sample. The third DTG maximum at 410-420°C was caused by oxidation and breakdown of the char to gaseous product.
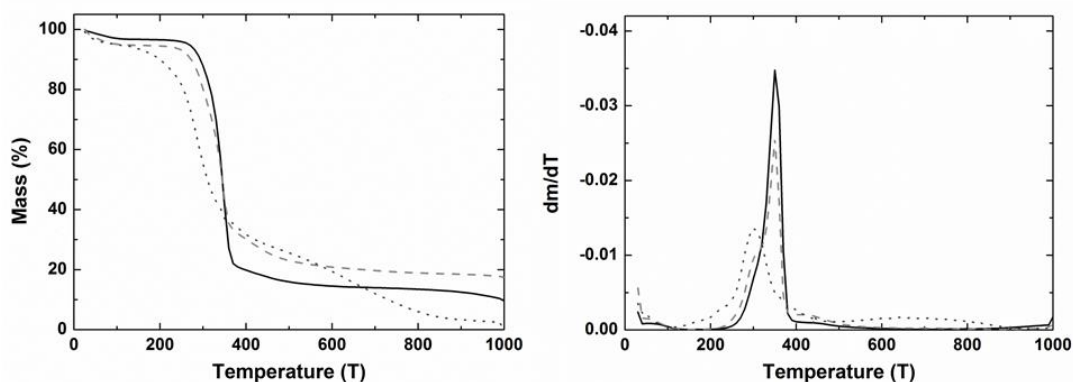
Figure S2. Thermogravimetric (left) and derivative thermogravimetric (DTG) curves (right) of unmodified NFC film, NFC/DCBD-HFBI film and pure DCBD-HFBI protein (Black solid line, light grey dashed line and dark grey dotted line, respectively).

Table 1. Mass loss of the TGA.

T (°C)	NFC	NFC/DCBD-HFBI	HFBI DCBD
25 - 150	3.3%	5.3%	6.0%
150 - 400	76.8%	64.5%	61.2%
400 - 600	5.3%	9.3%	12.7%
600 - 1000	5.0%	3.5%	18%
Residue	9.6%	17.4%	2%
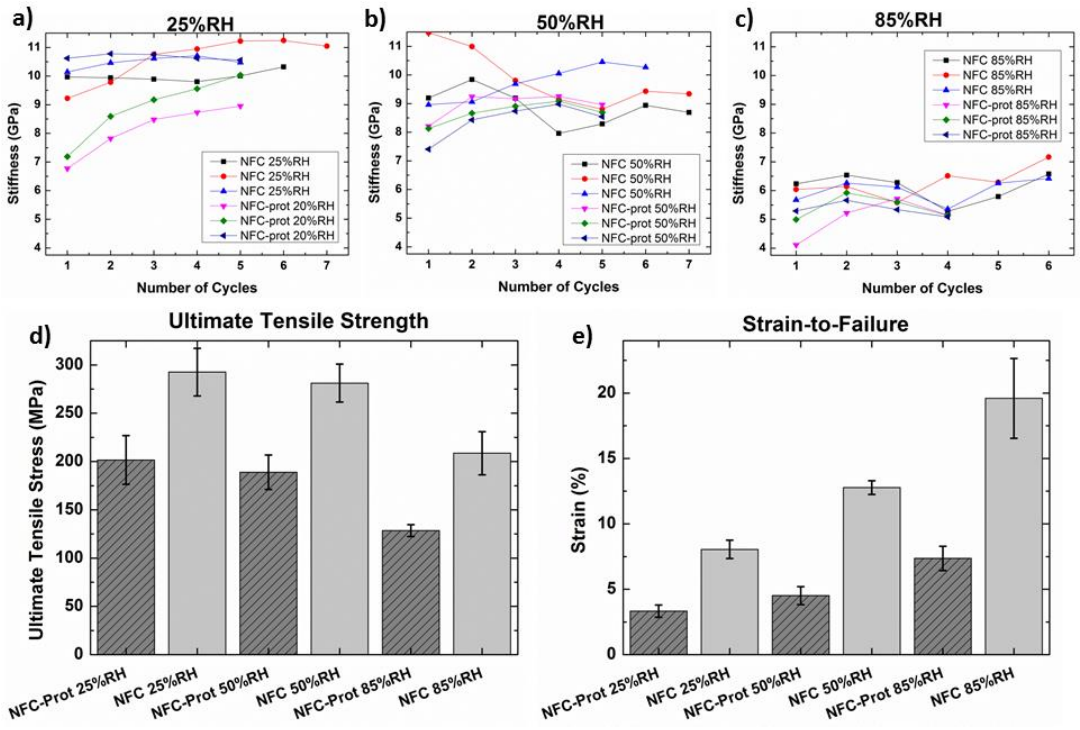
Figure S3. Cyclic measurements of unmodified NFC film and NFC/DCBD-HFBI hybrid films in 25%RH, 50%RH and 85%RH. a-c) Show three diagrams, where the development of stiffness during the cyclic measurements at 25%RH, 50%RH and 85%RH (a-c respectively) is drawn as a function of the cycles. d) Displays the average tensile strength for NFC/DCBD-HFBI and unmodified NFC films with standard deviation. e) Shows the average strain-at-failure values for NFC/DCBD-HFBI and NFC films with standard deviation.
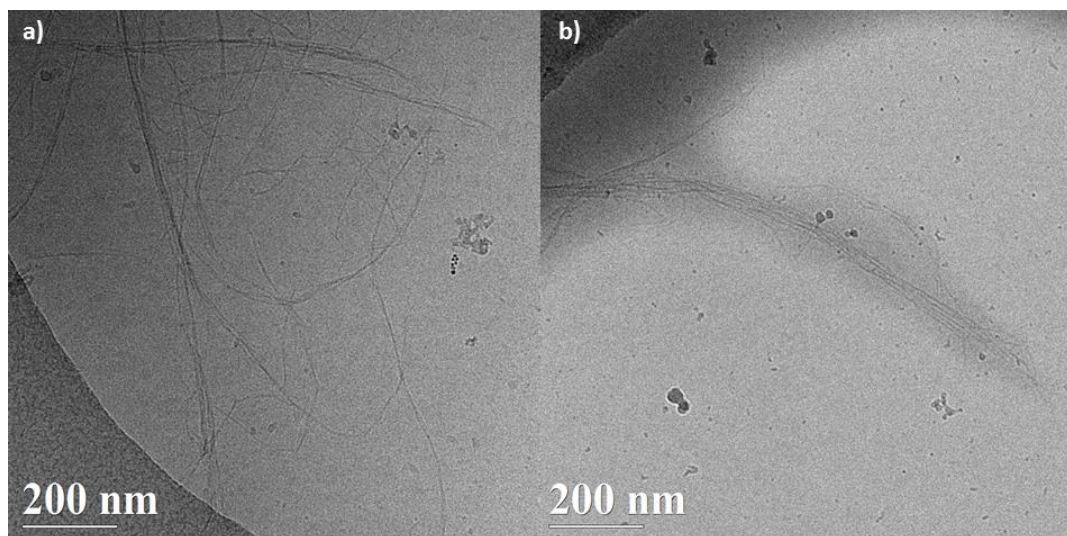
Figure S4. Cryo-TEM images of vitrified dispersions of a) unmodified NFC nanofibers and b) HFBI-DCBD modified NFC nanofiber dispersion.

Modular tuning of the supracolloidal interactions between nanocellulose fibrils with genetically engineered protein binding units

Modular Tuning of the Supracolloidal Interactions between Nanocellulose Fibrils with Genetically Engineered Protein Binding Units**

Jani-Markus Malho, Suvi Arola, Päivi Laaksonen, Géza R. Szilvay, Olli Ikkala, Markus B. Linder

***Abstract**: Mechanically excellent colloidal level fibers based on nanofibrillated cellulose (NFC) were combined with genetically engineered proteins to allow tunable supracolloidal interactions. The proteins consist of two cellulose-binding domains (CBD) separated by linkers of lengths of 12-, 24-, or 48-mers to provide modularly tailored binding to NFC. Connected by another linker, the opposing end of the protein optionally incorporates a multimerizing hydrophobin (HFB). Incorporation of HFBs increases considerably the moduli and yield strength values in the mechanical properties of solid films. Increased linker length between the two CBDs leads to reduced adsorption on NFC but to a higher yield strength and strain in comparison to the shorter linker. Our interpretation is that longer linkers allow sequential detachment of the CBDs in the strained state. Such an effect would suggest formation of de-novo protein-based sacrificial bonding constructs between the colloidal NFC nanofibrils.*

Biological structures lead to a wealth of multifunctional high-performing materials based on a limited palette of basic components. Therein, multiple levels of hierarchy connect molecular, colloidal, and macroscopic architectures across the length-scales.[1] The mechanically strong biological structural materials are nanocomposites where the reinforcing hard components are interlinked in balanced ways by soft components which provide sufficient binding for promoted overall strength and stiffness, still allowing energy dissipation upon deformations, such as silk, bone, tendons, mollusk shells, and insect exoskeletons.[1a-d, 1f, 1g, 2] In materials science, various efforts have been presented to mimic such concepts in technologically more feasible ways, also to introduce new functions: Using layered reinforcements, examples are provided by inorganic/polymer nanocomposites by freeze-casting, sequential spin coatings, and layer-by-layer depositions.[3] The mechanically excellent nanocelluloses with their native internal crystalline structures based on the parallel grossly hydrogen bonded cellulose chains have recently been employed as nanofibrillar reinforcements. Examples include long and entangled nanofibrillated cellulose (NFC) from plant cell wall sources, rod-like cellulose nanocrystals (CNC) based on strong acid hydrolysis of NFC, and bacterial cellulose (BC) from *Acetobacterium xylium*.[4] They all have lateral dimensions of a few nanometers and length from 100-300 nm for CNC towards macroscopic ones for BC. Among these the plant-based nanofibrils, i.e., NFC and CNC, are particularly attractive due to the wide availability of the plant cell wall resources. Sheets of NFC have been prepared for strong nanopaper films.[5] Nanocellulose constructs involving polymeric, proteinic or supramolecular corona layers have been used, in an effort to tune the interactions between the nanofibrils, towards tuning the mechanical properties.[6] Using CNC, supramolecular groups have been used to tune the mutual interactions, such as using 2-ureido-4[1H]-pyrimidone (UPY) in blends[6k] and to form sacrificial bonds[6l], which has led to toughened CNC films showing non-catastrophic fracture processes. Finally, tunable interactions between CNCs can lead to switchable mechanical properties in composites.[7]

Such considerations indicate that it is relevant to develop concepts to tune in detail the interactions between the nanoscopic reinforcements for nanocelluloses and in more general in the supracolloidal chemistry. Even more, it has been suggested that one of the central mechanisms in biological structural nanocomposite materials involves sacrificial bonds, which involve sequential supramolecular bond openings upon deformations, still allowing sufficient adhesion.[2c] In this work we created constructs in which NFC was used as a "hard" reinforcing component and genetically engineered proteins functioned as a "soft" adhesive matrix with the intention to achieve in-depth tunable interactions between the NFCs and to achieve sequential sacrificial bonds. NFC has a high aspect ratio, being typically several micrometers in length and 5-20 nanometers in width.[4a] It is obtained from softwood pulp by mechanical integration. We have previously shown that engineered proteins with specific binding functions can be used as an adhesive matrix, allowing to tune the plastic behavior of NFC composites and in combination with graphene also affecting the stiffness and strength.[8]

Using genetic engineering techniques and proteolytic processing[9] we constructed six different variants of adhesive proteins consisting of modules aiming to bind to nanocellulose in a sequential manner and involving modules for capable of protein-protein supramolecular interactions (Figure 1). As protein modules for adhesion towards nanocellulose we used two cellulose-binding domains (CBDs),[10] whose cooperative effect was tailored based on a different lengths of the linker between the CBDs. As multimerizing supramolecular modules we used class II hydrophobin proteins (HFBI)[11], see Figure 2.
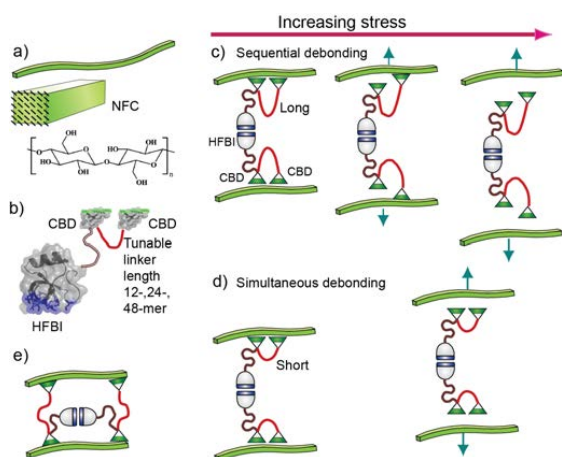
Figure 1. Schematics for the aimed supracolloidal interactions between cellulose nanofibrils. a) Nanofibrillated cellulose (NFC). b) The engineered proteins, having two cellulose binding domains (CBD) with three linker lengths. The other end of the protein consists of hydrophobin (HFBI). c) For long linkers, the two CBDs were expected to bind non-cooperatively, thus potentially allowing sequential detachment upon mechanical deformation, taken intact HFB-HFB interactions. d) For short linkers, the two CBDs are expected to detach cooperatively under mechanical deformations, i.e. simultaneously. e) Another possible mode of interaction. Also the HFB-HFB interaction can open in deformations.

CBDs are found in enzymes that interact with cellulose, where they bind to cellulose by specific combinations of hydrogen bonding and stacking of aromatic residues and pyranose rings between the protein side chains and the cellulose molecules on the surface of the native cellulose nanofibrils. By

coupling two CBDs together using a specific linker (Figure 2) to produce a "double CBD" (DCBD) one can obtain a molecular motif with a modularly adjustable affinity to cellulose without altering the residue-level interactions. We created three different proteins that were otherwise identical but the linker connecting the CBD modules had different peptide chain lengths (12-, 24-, and 48-mers, respectively), see Figure 2. The proteins were denoted as HFBI-DCBD-(12-mer), HFBI-DCBD-(24-mer), and HFBI-DCBD-(48-mer). The CBDs were constructed based on the sequences of *Trichoderma reesei* Cel6A (38 amino acids) and Cel7A (36 amino acids). We expected that a longer "non-functional" linker could modify the affinity of the dimeric CDBs towards NFC. Indeed, the analysis of binding affinities showed that the DCBD constructs with increasing linker-lengths interacted less with nanocellulose (Figure 3). Our interpretation is that a short linker tethers the domains close to each other and promoted cooperative binding, i.e., when one of the CBDs in the DCBD binds to cellulose the effective concentration of its pair becomes locally high, thus leading to a high probability of binding of the second CBD. For longer linkers, a less efficient tethering leads to lower affinity. In consequence, the DCBD has 3 different binding states, depending whether 2, 1, or 0 CBDs undergo binding. Of these, the first state occurs with higher probability when the linker has an optimal length, not too short or too long.

The remote end of the proteins incorporated HFBI modules, capable of providing enhanced protein-protein supramolecular interactions.[11] The hydrophobins are amphiphilic proteins that interact strongly with each other forming multimeric complexes. We used the class II hydrophobin HFBI in this study. Each DCBD and HFBI-DCBD was otherwise identical and the DCBD was made from the corresponding HFBI-DCBD by proteolytic cleavage of the linker connecting the hydrophobin and CBDs (Figure 2).
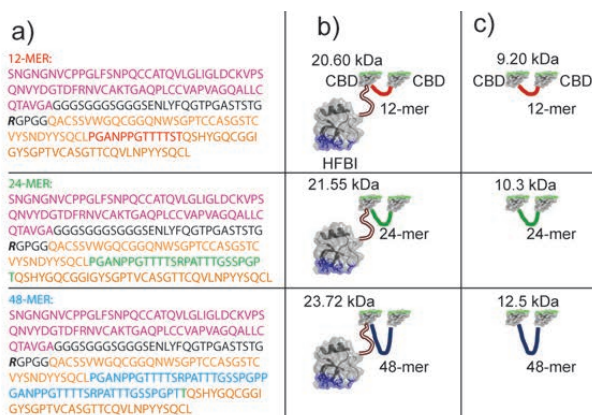

Figure 2. a) Amino acid sequences of the three HFBI-DCBD proteins. b) Schematic illustrations. c) For reference, the corresponding proteins were constructed without the supramolecular binding motif HFB (amino acid sequences denoted as violet) and its linker unit (black). The arginine (R) residue at which trypsin cleavage occurs is marked with bold and italic R.
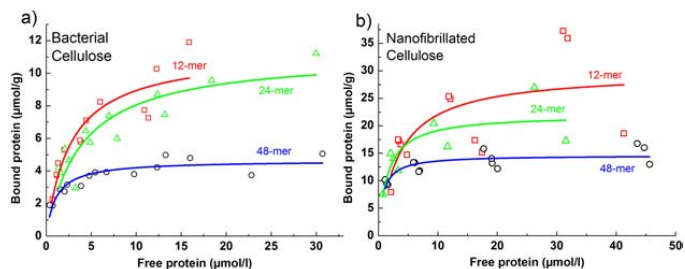
Figure 3. Binding isotherms of the HFBI-DCBD proteins on nanocelluloses for the three linker lengths between the two CBDs. a) Binding on bacterial cellulose. b) Binding on nanofibrillated cellulose. Note that due to the shorter nanofibrils, the separation of the adsorbed and free protein was more difficult in the binding assay, thus leading to large scatter.

Films of NFC involving different interlinking proteins were made to analyze the effects of protein structure for the tensile mechanical properties at controlled humidity (50% RH) and ambient temperature (21 °C). The films were prepared using different aqueous protein loadings, 0.5 gl^{-1}, 0.85 gl^{-1}, and 1.5 gl^{-1} together with 2 gl^{-1} of NFC, followed by drying. This range of concentration corresponds to 26 to 78 µM for HFBI-DCBD-(12-mer), 24 to 74 µM for HFBI-DCBD-(24-mer), and 22 to 67 µM for HFBI-DCBD-(48-mer). The differences in binding constants result in different bound amounts for each of the different constructs, see Figure 3. In this range the binding due to the 12-mer is the highest resulting of bound amounts from 8 to 14 µmolg^{-1} and DCBD using the 48-mer having the lowest binding from 3-5 µmolg^{-1} i.e. the concentration range from half-maximum to maximum for the binding of the constructs to cellulose, as calculated from the binding isotherms. Tensile stress-strain curves of the dried films are shown in Figure 4, also showing the films without protein as a control. The relatively high aspect ratio of pristine NFC results in an entangled dense "spaghetti-like" colloidal structure where the stiffness and strength is promoted by the entanglements of the nanofibrils and hydrogen-bonds, as already known.[5a] Beyond the yield point (Figure 4), plastic deformations of nanofibrils past each other are inferred, and the strain hardening suggests some fibril orientation during the plastic deformation.[12] The films with proteins showed significant concentration dependent effects in the stress-strain curves (Figures S1 and S2). Incorporating DBCD-HFB with the 12-mer linker increased the yield strength to 105 MPa from 85 MPa of the pristine NFC, as well as increase of the Young's modulus to 11.6 GPa from 8.6 GPa, respectively. The strain was reduced from 10.3 % to 3.6 % (see Figure 4 and 5). At the same time, the binding isotherm suggests efficient binding of the protein onto the NFC. Combining these findings suggests that the DBCD-HFB-(12-mer) allowed a strong interlinking between the NFC nanofibrils due to the adsorbed CBDs and supramolecular binding between HFBs (Figure 1d left). This leads to high stiffness and yield strength, but suppresses their relative plastic deformations due to strong connectivity. That the supramolecular interactions between the HFBI motifs were operational, was manifested in the stress strain curves, where incorporation of the DCBDs without HFB lead to lower moduli and considerably larger strain in comparison to the case with HFBI-DCBD. Increasing the linker length to 24-mer and 48-mer in NFC/HFBI-DCBD, lead to further increase of the moduli and yield strength in comparison to the case where 12-mer was used (Figure 5). This suggests increased interlinking between the NFCs, even if the isotherms showed reduced adsorption on NFC. Also, the maximum strain increased in comparison to the case of the 12-mer. In other words, the long linkers promote interlinking, yet smaller adsorption on NFC, still allowing mutual movements, which seems at first sight paradoxical. We tentatively interpret this by the effect of the longer linker allowing sequential detachment of the CBDs, where detachment of one

CBD still allows interlinking due to the second CBD, where the weaker binding of a single CBD on NFC allows plastic mutual movement of NFCs. Again, removal of HFBI leads to reduced yield strength, signaling the role of HFBI to supracolloidal binding between NFCs. But here the effect was smaller than in the case of 12-mers, as the 24-mer and 48-mer are more prone to make also bonds between two different NFC nanofibrils, as allowed by the longer linkers.

In addition to the above tensile tests, cyclic tensile measurements were performed for NFC incorporating the HFBI-DCBD-(48-mer), DCBD-(48-mer), and pristine NFC films to study the dissipative properties more closely. Representative stress-strain curves from cyclic tensile measurements for the hybrids that contain 0.85 gl^{-1} of protein and for the unmodified NFC film are shown in Figure S5. The results show that deformations after the yield point were not recovered after stress release and therefore the deformations were plastic. Furthermore, the elastic moduli were constant throughout the tensile testing for the hybrid films and the unmodified NFC films, which suggests that the elastic properties were based on non-covalent and reversible interactions.
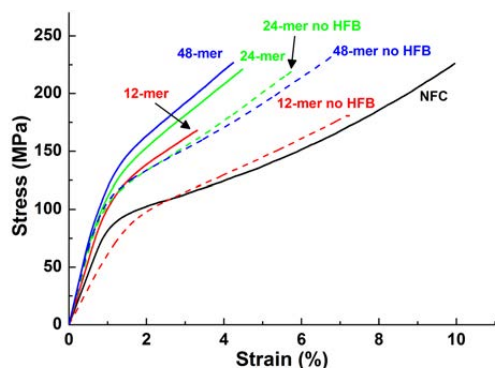

Figure 4. Representative stress-strain curves from non-cyclic tensile measurements. Unmodified NFC film is drawn with a solid black line, and the constructs based on HFBI-DCBD with 12-, 24-, and 48-mer linker lengths with a solid red, green and blue lines, respectively. The omission of the supramolecular binding units HFBI is described using the dashed lines of same colors, respectively.
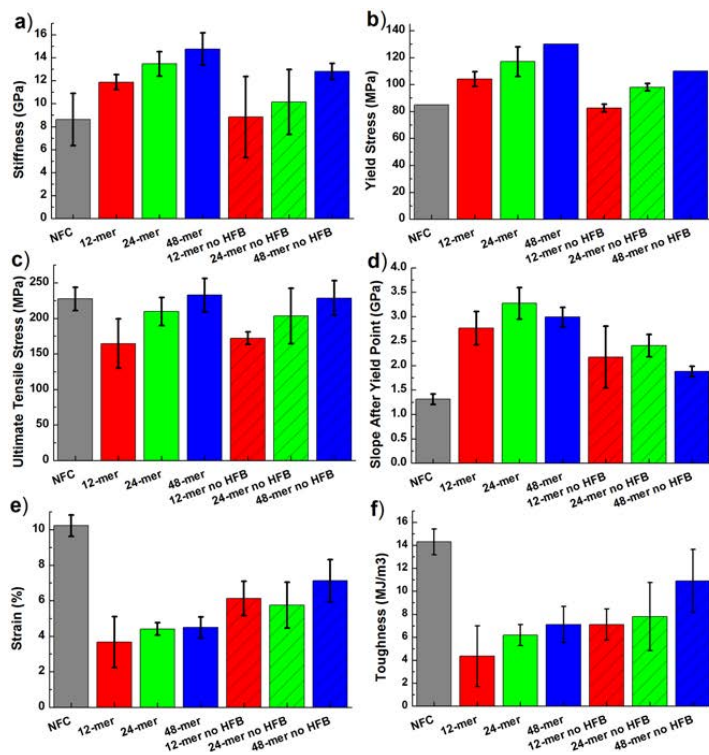
Figure 5. Mechanical properties of the HFBI-DCBD and DCBD and unmodified NFC film as a reference. a) stiffness; b) yield strength; c) ultimate tensile strength; d) slope after yield point; e) strain-to-failure and f) toughness. The standard deviations are shown for all data.

Cryo-TEM imaging was carried out to observe the modified and native NFC nanofibril dispersions. Images showed mainly bundles of NFC/HFBI-DCBD-(48-mer) and NFC/DCBD-(48-mer) with no or few individually dispersed nanofibrils, whereas the native NFC nanofibrils showed less aggregated and even individually dispersed nanofibrils (see supplementary information Figure S6). The vitrified protein-NFC dispersions can be qualitatively interpreted as biomolecular crosslinking of the NFC nanofibrils via HFBI-DCBD-(48-mer) and DCBD-(48-mer).

We conclude that genetically engineered protein constructs allow a modular control of supracolloidal interaction strengths between cellulose nanofibrils. The binding on nanocellulose is realized using two cellulose binding domains (DCBDs). To achieve tunable binding, instead of modifying the internal structure of the CBDs, the net binding is tuned in a modular fashion by incorporating polypeptide linker of length 12, 24, or 48 amino acid residues. The proteins are also equipped with hydrophobin (HFBI) proteins, capable of mutual supramolecular interactions. Based on aqueous binding isotherm and tensile measurements of dried films, it is inferred that the long linkers lead to smaller protein binding on NFC, still allowing increased modulus and strain, in comparison to short linkers. We interpret this by protein based sacrificial bonds that open sequentially upon deformations. We foresee that genetic engineering is worth pursuing towards exactly tuned multifunctional de-novo supracolloidal materials combining competing properties for nanocellulose.

[*]Prof. P. Laaksonen, Prof. M. B. Linder*
School of Chemical Technology,
Aalto University
P.O. Box 16100, FI-00076 Aalto, Finland
markus.linder@aalto.fi
hyber.aalto.fi

J-M. Malho, Dr. G. Szilvay
VTT Technical Research Centre of Finland
 Tietotie 2, P.O. Box 1000, FI-02044, Espoo, Finland

S. Arola*, Prof. O.Ikkala.
School of Science
Aalto University
P.O. Box 11100, FI-00076 Aalto, Finland
* and VTT Technical Research Centre of Finland

[1]   aP. Fratzl, R. Weinkamer, *Progress in Materials Science* **2007**, *52*, 1263-1334; bM. A. Meyers, P.-Y. Chen, A. Y.-M. Lin, Y. Seki, *Progress in Materials Science* **2008**, *53*, 1-206; cH. D. Espinosa, J. E. Rim, F. Barthelat, M. J. Buehler, *Progress in Materials Science* **2009**, *54*, 1059-1100; dB. Bhushan, *Philosophical Transactions of the Royal Society A: Mathematical, Physical and Engineering Sciences* **2009**, *367*, 1445-1486; eM. Suzuki, K. Saruwatari, T. Kogure, Y. Yamamoto, T. Nishimura, T. Kato, H. Nagasawa, *science* **2009**, *325*, 1388-1390; fS. Keten, Z. Xu, B. Ihle, M. J. Buehler, *Nature materials* **2010**, *9*, 359-367; gM. J. Buehler, *Nano Today* **2010**, *5*, 379-383.
[2]   aP. Fratzl, I. Burgert, H. S. Gupta, *Physical Chemistry Chemical Physics* **2004**, *6*, 5575-5579; bJ. W. Dunlop, P. Fratzl, *Annual Review of Materials Research* **2010**, *40*, 1-24; cG. E. Fantner, E. Oroudjev, G. Schitter, L. S. Golde, P. Thurner, M. M. Finch, P. Turner, T. Gutsmann, D. E. Morse, H. Hansma, *Biophysical Journal* **2006**, *90*, 1411-1418.
[3]   aZ. Tang, N. A. Kotov, S. Magonov, B. Ozturk, *Nature materials* **2003**, *2*, 413-418; bE. Munch, M. E. Launey, D. H. Alsem, E. Saiz, A. P. Tomsia, R. O. Ritchie, *science* **2008**, *322*, 1516-1520; cL. J. Bonderer, A. R. Studart, L. J. Gauckler, *science* **2008**, *319*, 1069-1073; dA. Walther, I. Bjurhager, J.-M. Malho, J. Pere, J. Ruokolainen, L. A. Berglund, O. Ikkala, *Nano letters* **2010**, *10*, 2742-2748.
[4]   aD. Klemm, F. Kramer, S. Moritz, T. Lindström, M. Ankerfors, D. Gray, A. Dorris, *Angewandte Chemie International Edition* **2011**, *50*, 5438-5466; bY. Habibi, L. A. Lucia, O. J. Rojas, *Chemical reviews* **2010**, *110*, 3479-3500.
[5]   aM. Henriksson, L. A. Berglund, P. Isaksson, T. Lindström, T. Nishino, *Biomacromolecules* **2008**, *9*, 1579-1585; bM. Nogi, S. Iwamoto, A. N. Nakagaito, H. Yano, *Advanced Materials* **2009**, *21*, 1595-1598.

[6]   aQ. Zhou, H. Brumer, T. T. Teeri, *Macromolecules* **2009**, *42*, 5430-5432; bQ. Zhou, E. Malm, H. Nilsson, P. T. Larsson, T. Iversen, L. A. Berglund, V. Bulone, *Soft Matter* **2009**, *5*, 4124-4130; cE. Kloser, D. G. Gray, *Langmuir* **2010**, *26*, 13450-13456; dF. Azzam, L. Heux, J.-L. Putaux, B. Jean, *Biomacromolecules* **2010**, *11*, 3652-3659; eS. Utsel, E. E. Malmström, A. Carlmark, L. Wågberg, *Soft Matter* **2010**, *6*, 342-352; fJ. Majoinen, A. Walther, J. R. McKee, E. Kontturi, V. Aseyev, J. M. Malho, J. Ruokolainen, O. Ikkala, *Biomacromolecules* **2011**, *12*, 2997-3006; gH. Lonnberg, K. Larsson, T. Lindstrom, A. Hult, E. Malmstrom, *ACS applied materials & interfaces* **2011**, *3*, 1426-1433; hA. Carlmark, E. Larsson, E. Malmström, *European Polymer Journal* **2012**, *48*, 1646-1659; iG. Morandi, W. Thielemans, *Polymer Chemistry* **2012**, *3*, 1402-1407; jP. S. Lacerda, A. M. Barros-Timmons, C. S. Freire, A. J. Silvestre, C. P. Neto, *Biomacromolecules* **2013**, *14*, 2063-2073; kM. V. Biyani, E. J. Foster, C. Weder, *ACS Macro Letters* **2013**, *2*, 236-240; lJ. R. McKee, J. Huokuna, L. Martikainen, M. Karesoja, A. Nykänen, E. Kontturi, H. Tenhu, J. Ruokolainen, O. Ikkala, *Angewandte Chemie* **2014**, *126*, 5149-5153; mC. O.-P. J.-M. Malho, M. Rüggerberg, P. Laaksonen, O. Ikkala, I. Burgert, M. B. Linder, **2014**.

[7]   J. R. Capadona, K. Shanmuganathan, D. J. Tyler, S. J. Rowan, C. Weder, *science* **2008**, *319*, 1370-1374.

[8]   P. Laaksonen, A. Walther, J. M. Malho, M. Kainlauri, O. Ikkala, M. B. Linder, *Angewandte Chemie International Edition* **2011**, *50*, 8688-8691.

[9]   P. Laaksonen, G. R. Szilvay, M. B. Linder, *Trends in biotechnology* **2012**, *30*, 191-197.

[10]   I. Levy, O. Shoseyov, *Biotechnology advances* **2002**, *20*, 191-213.

[11]   aM. B. Linder, *Current Opinion in Colloid & Interface Science* **2009**, *14*, 356-363; bM. Lienemann, J.-A. Gandier, J. J. Joensuu, A. Iwanaga, Y. Takatsuji, T. Haruyama, E. Master, M. Tenkanen, M. B. Linder, *Applied and environmental microbiology* **2013**, *79*, 5533-5538; cT. Nakari-Setälä, N. Aro, N. Kalkkinen, E. Alatalo, M. Penttilä, *European Journal of Biochemistry* **1996**, *235*, 248-255.

[12]   H. Sehaqui, N. Ezekiel Mushi, S. Morimune, M. Salajkova, T. Nishino, L. A. Berglund, *ACS applied materials & interfaces* **2012**, *4*, 1043-1049.

Supporting Information

Modular tuning of the supracolloidal interactions between nanocellulose fibrils with genetically engineered protein binding units

Jani-Markus Malho, Suvi Arola, Päivi Laaksonen, Géza R. Szilvay, Olli Ikkala, Markus B. Linder*

Nanofibrillated Cellulose and Bacterial Cellulose

A dilute hydrogel (solid content 1.64%) of nanofibrillar cellulose was used as a starting material. The cellulose was mechanically disintegrated by ten passes through a M7115 Fluidizer (Microfluidics Corp., U.S.A.) essentially according to previous reports[1]. Nanofibrillated cellulose was then used for the films. Bacterial cellulose (Nata de Coco), which had a solid content of 2.55gl^{-1}, was used for the binding studies instead of nanofibrillated cellulose as it can be more readily separated from the dispersion for the binding assay.

Gene Constructs

Three protein constructs, HFBI-DCBD-A, -B, and -C, were designed where all contained an N-terminal hydrophobin HFBI[2] linked to two cellulose binding domains (DCBD)[3], but each had a different sized linker sequence between the two cellulose binding domains (CBD). The constructs were based on the previously published protein HFBI-DCBD described by Linder *et al*. [3-4] The linker sequences between the CBDs were designed so that HFBI-DCBD-B has a linker length of 24 amino acids (linker B) (identical to HFBI-DCBD[3]), HFBI-DCBD-A has a linker length of 12 amino acids (linker A) and is comprised of the first half of linker B, and HFBI-DCBD-C has a linker where the linker B was doubled to 48 amino acids (linker C). The linker between HFBI and DCBDs was identical in all three constructs and contained two protease sites; one for Tobacco Etch Virus protease enzyme (TEV)[5] and one for trypsin. All linker sequences are summarized in Table S1.

Synthetic genes encoding HFBI, DCBD-A, DCBD-B, and DCBD-C flanking with compatible BsaI-sites were ordered from GenScript USA Inc. (NJ, USA) with *Trichoderma reesei* optimized codon usage in BsaI-free pUC57 plasmids. Golden Gate cloning [6] was used for assembling the *T. reesei* transformation cassettes from six pieces into a destination plasmid (pJJJ307, which is based on the pMK-RQ backbone) resulting in plasmids pHFBI-TEV-DCBDa, pHFBI-TEV-DCBDb and pHFBI-TEV-DCBDc. The assembled parts were (in 5'-3' order) i) cbh1 promoter (pJJJ308), ii) HFBI coding sequence with signal sequence for secretion, iii) DCBD (A, B or C) coding sequence, iv) cbh1 terminator (pJJJ311), v) hph hygromycin resistance marker gene under the gdpA promoter for strain selection (pJJJ312), and vi) a 3' flank sequence (pJJJ313) that together with the CBHI promoter serves to guide the gene recombination into the cbh1 locus in *T. reesei*. The ligation products were then transformed into *E. coli* XL1-Blue cells and plasmid containing transformants were selected on kanamycin plates and further selected by blue-white screening for insert-containing clones. Correct assembly of the transformation cassette was verified by restriction enzyme analysis and the correct protein coding sequence was verified by DNA sequencing. The transformation cassettes were then cut from the vectors using PmeI and purified by agarose gel electrophoresis followed by gel extraction using dialysis.

Transformation of *Trichoderma reesei*

Biolistic PDS-1000/He Particle Delivery System (Bio-Rad, CA, USA) was used for the transformation of *T. reesei* M122 spores. The particle bombardment was performed under a helium pressure of 850 psi. Gold microcarrier particles (0.6 µm, Bio-Rad) were coated with the linear transformation cassette DNA according to the instruction manual of Bio-Rad laboratories. Gold particles without DNA were used as a control. After transformation the spores were plated on PD-plates with top-agar containing 1M $MgSO_4$, 1M $CaCl_2$ and 150 µg/ml hygromycin for selection and grown for 3 – 10 days in 28 °C. For selecting transformants several colonies were picked and streaked on PD-Triton plates containing hygromycin and grown for 5 – 8 days in 28 °C. The transformants were then re-streaked to new selective Triton plates and grown as above to ensure growth of only hygromycin resistance containing transformants. Insert containing transformants were identified by direct PCR (Phire® Plant Direct PCR kit, Finnzymes, F-130) using suitable oligonucleotide primers. Correct recombination localization into the cbh1 locus was verified by the absence of an amplicon using cbh1 specific primers.

Protein Production and Purification

The proteins were produced under the following conditions in 50 ml shake flask cultures: *T. reesei* minimal media, 4% lactose , 2% spent grain extract, 100 mM PIPPS (Piperazine-N,N'-*bis*(3-propanesulfonic Acid)) pH 5.5, 2.4 mM $MgSO_4$, 4.1 mM $CaCl_2$, 28°C, 7 days. To identify protein producing strains culture media and biomass extracts from growth time points were analysed by western blotting using rabbit anti-HFBI antibodies. The transformants selected for protein production were VTT-D-133335 (HFBI-DCBD-A), VTT-D-133336 (HFBI-DCBD-B), and VTT-D-133337 (HFBI-DCBD-C). The strains were then cultivated in 7 L bioreactors on media containing 50 vol-% spent grain extract, 60 g/L lactose, 1 g/L yeast extract, 4 g/L KH_2PO_4, 2.8 g/L $(NH_4)_2SO_4$, 0.6 g/L $MgSO_4 \cdot 7H_2O$, 0.8 g/L $CaCl_2 \cdot 2H_2O$, 2 ml/L trace solution. The pH was let to drop from 5 to about 3 during cultivation. At 24 h intervals 48 mg pepstatin A and 28 mg soy bean trypsin inhibitors (both from Sigma-Aldrich) were added to the cultures to minimize protein degradation. The culture supernatants were separated from the biomass by filtration through GF/A filters (Whatman). Protein expression levels were analysed by RP-UPLC and were 0.2 g/L, 0.4 g/L, and 3.0 g/L for HFBI-DCBD-A, -B, and -C, respectively. The proteins were purified using aqueous two phase extraction and reverse-phase high-performance liquid chromatography (RP-HPLC) as described earlier [7] followed by lyophilisation.

Linker digestions

The fusion proteins were cleaved with sequencing grade modified trypsin (Promega) in 25mM Tris-HCl – 150mM NaCl buffer for 2 hours in room temperature. The trypsin digestion reaction was followed by RP-UPLC using a 2.1 x 100 mm, 1.7 µm, C4 Acquity BEH300 prST column and an Acquity I-Class system with a photodiode array detector (Waters, MA, USA). The proteins were eluted in a linear mobile phase gradient from 20 – 60% B using water (A) and acetonitrile (B), both containing 0.1% trifluoroacetic acid. Concentrations of the analysed proteins were determined using standard samples with protein concentrations determined by amino acid analysis (Amino Acid Analysis Lab, Uppsala University, Sweden).

Cellulose Binding Measurements

Bacterial cellulose was diluted to have concentration of $0.425gl^{-1}$ and the NFC to have $0.5gl^{-1}$ in all of the binding measurements. Only trypsin cleaved and HPLC purified DCBD domains (DCBD-A, -B and -C) were used to perform the binding studies. Prior to the binding assay the amount of protein was verified by absorbance at 280 nm (Cary 100 spectrophotometer, Varian Inc., CA, USA). Protein solutions were then mixed with bacterial cellulose and NFC dispersions by brief vortexing and incubated for 2 hours at +21°C.

After incubation the samples were centrifuged for 1 hour with 14000 rpm at +21°C. The supernatants were then removed and analysed by RP-UPLC as described above for quantitation of unbound protein.

Film Preparation and Humidity Control

The NFC concentration was kept at 2.0gl^{-1} in all films. Vacuum filtration was used to prepare films from dispersions mixtures containing NFC and proteins. The dispersions were filtrated using a Durapore membrane (GVWP, 0.22 µm, Millipore, U.S.A.) and an O-ring to define the film diameter. A gentle pressure was applied to the films using a 300 g load for 10 min to prevent wrinkling before oven drying overnight at +65 °C. Samples were then stabilized in a humidity controlled room at 50%RH prior to measurements.

Mechanical Tensile Testing

Tensile testing was performed on 5kN Tensile/compression module (Kammrath & Weiss GmbH, Germany) using 100N load cells. The elongation speed was 0.5 mm/min and the gauge length 10 mm. Samples were stabilized overnight in a humidity controlled room of 50%RH prior to the mechanical tensile testing. All of the tensile tests were performed at 50%RH. At least 4 specimens were measured from each sample. Specimen sizes were 2 cm × 2 mm × 7–13 µm, length, width, and thickness, respectively.

TEM

High resolution transmission electron microscopy imaging was performed using JEM-3200FSC field emission microscope (JEOL), which was operated at 300 kV in bright field mode with Omega-type Zero-loss energy filter. Ultrascan 4000 CCD camera (Gatan) was used to acquire the images of samples that were maintained at 187°C. 3 µl of sample dispersions were vitrified on c-flat grids under 100% humidity with FEI Vitrobot. The sample dispersions were blotted for 1.5 s with a filter paper before vitrification.

Table S1. DNA and amino acid sequences of the linkers in the three fusion proteins HFBI-DCBD-A, -B, and -C.

Linker	Sequence[a]
Linker A	CCCGGCGCAAACCCGCCTGGCACCACCACCACCAGC PGANPPGTTTTS
Linker B	CCCGGCGCAAACCCGCCTGGCACCACCACCACCAGCCGCCCAGCCACTACCACTGGAAGCTCTCCCG GACCT PGANPPGTTTTSRPATTTGSSPGP
Linker C	CCCGGCGCAAACCCGCCTGGCACCACCACCACCAGCCGCCCAGCCACTACCACTGGAAGCTCTCCCG GACCTCCCGGCGCAAACCCGCCTGGCACCACCACCACCAGCCGCCCAGCCACTACCACTGGAAGCTC TCCCGGACCT PGANPPGTTTTSRPATTTGSSPGPPGANPPGTTTTSRPATTTGSSPGP
Linker connecting HFBI and DCBD	GGTGGAGGCTCTGGTGGAGGCTCAGGTGGAGGCAGTGAGAACCTCTACTTCCAGGGCCCGGGCGCGA GCACCAGCACCGGCCGCGGCCCGGGCGGC GGGSGGGSGGGSENLYFQ/GGLQGTPGASTSTGR/GPGG

[a] DNA sequences are shown in black and amino acid sequences in blue. Protease cleavage sites are shown for TEV and trypsin.
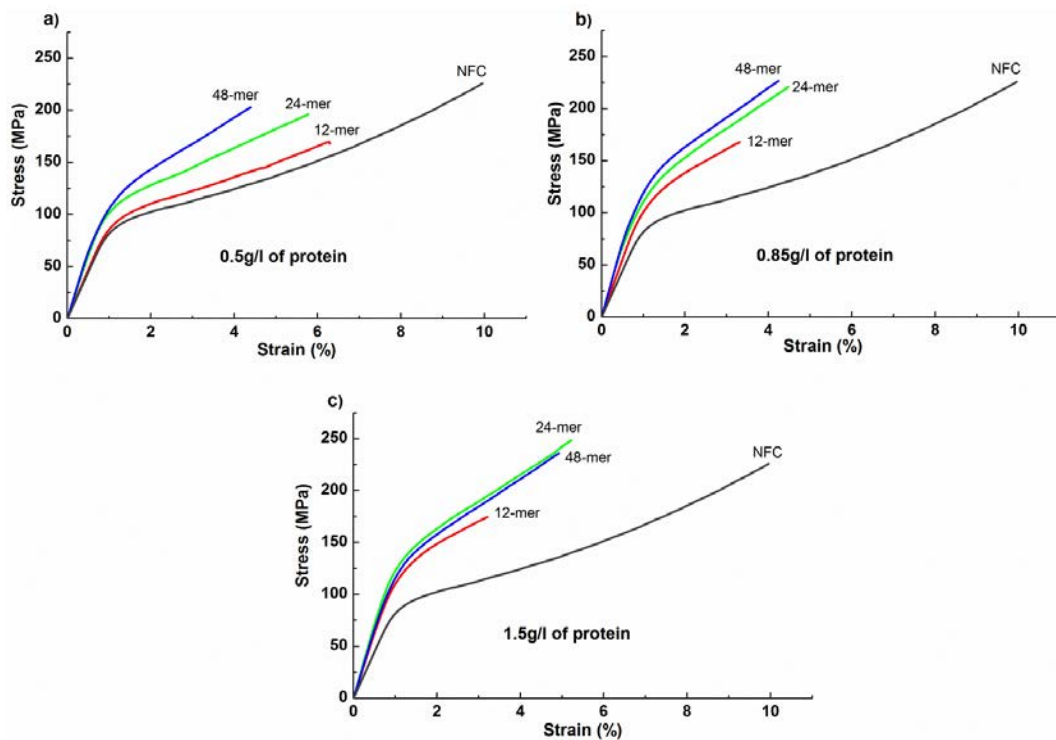
Figure S1. *Representative stress-strain curves of fusion proteins HFBI-DCBD-A, -B and -C in NFC matrix, where the red lines represent HFBI-DCBD-A-NFC (12-mer), green lines HFBI-DCBD-B-NFC (24-mer) and blue lines HFBI-DCBD-C-NFC (48-mer). Unmodified NFC film is drawn with black line. a)-c) exhibit fusion proteins in three concentrations (0.5gl⁻¹, 0.85gl⁻¹ and 1.5gl⁻¹, respectively). The concentration of NFC is kept 2.0gl⁻¹ in all of the films throughout the study.*
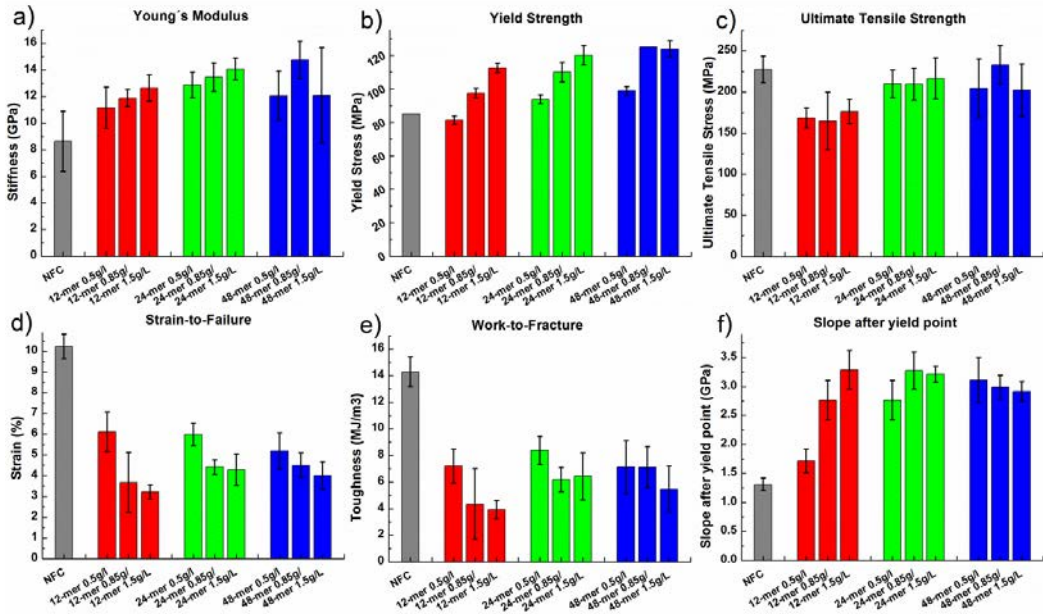
Figure S2. *Mechanical properties of three hybrids in three protein concentrations (0.5gl^{-1}, 0.85gl^{-1} and 1.5gl^{-1}) and an unmodified NFC film as a reference. a) young´s moduli, b) yield strengths, c) ultimate tensile strengths, d) strain-to-failure e) toughness and f) slopes after yield point with standard deviations. Grey bars represent unmodified NFC films, red bars HFBI-DCBD-A-NFC films (12-mer), green bars HFBI-DCBD-B-NFC films (24-mer) and blue bars HFBI-DCBD-C-NFC films (48-mer).*
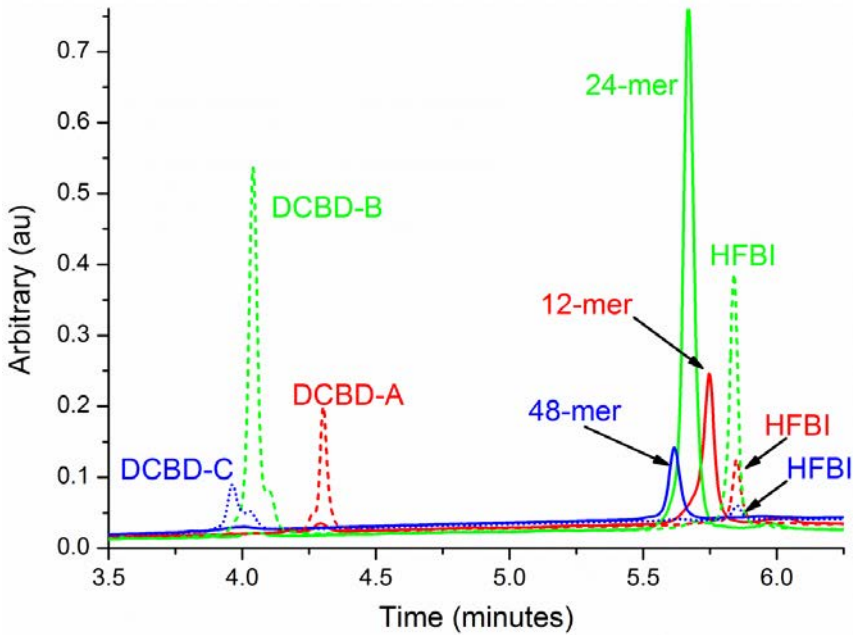
Figure S3. UPLC- chromatograms of the fusion proteins and the trypsin cleaved proteins. Bright red line represents HFBI-DCBD-A peak and the dark red line the trypsin cleaved DCBD-A and the HFBI peaks. Bright green line represents HFBI-DCBD-B and the dark green displays the cleaved DCBD-B and HFBI. Dark blue line is the HFBI-DCBD-C and the lighter blue line the DCBD-C and

HFBI. The concentrations used are not the same across samples and thus the peaks heights vary, whereas the elution times are related to differences between the protein structures. Peaks that are located at 3.80-4.40 minutes are cleaved DCBD-proteins, the fusion protein peaks are located between 5.50 and 5.80 minutes, and the cleaved HFBI-proteins from different constructs around 5.82 minutes. The HFBI-peaks from different fusion proteins elute almost at the same elution time, while the intact fusion proteins and DCBD protein -peaks show variation due to differences in their sequence and structure. The shoulders in the DCBD-peaks are expected to results from slight glycosylation occurring in the linker sequence between the two CBD-domains in the DCBD-structure.
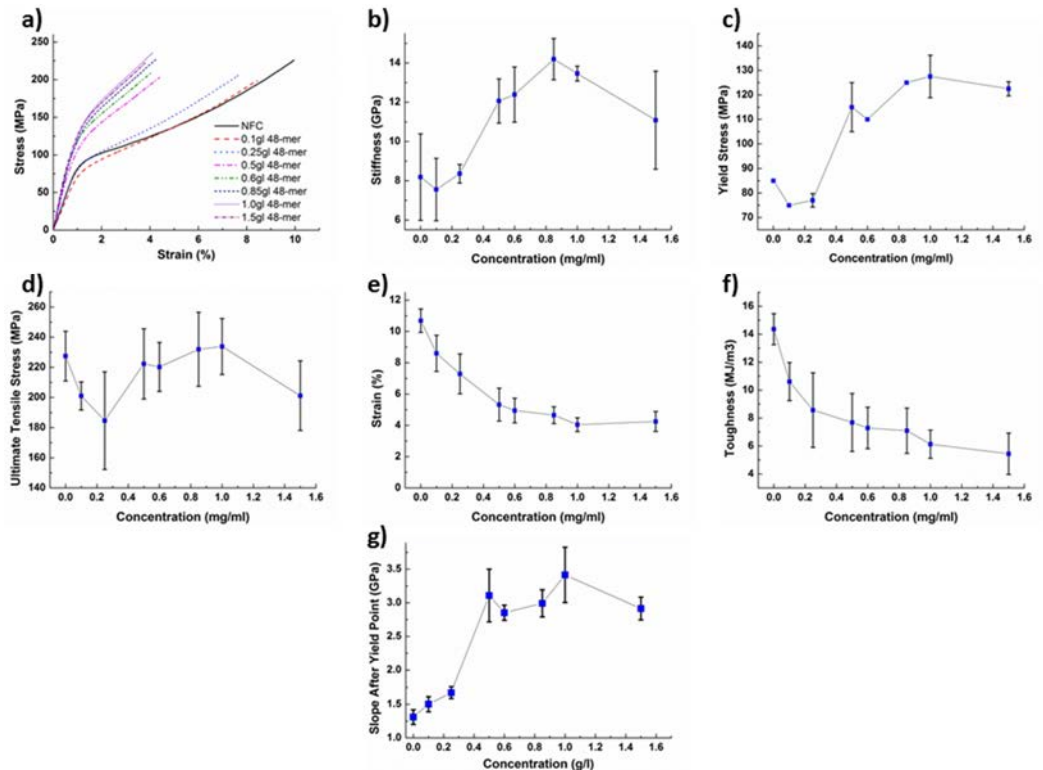
Figure S4 Mechanical properties of HFBI-DCBD-C as a function of concentration. a) Representative stress-strain curves. b) Young´s moduli, e) yield strength, d) Ultimate tensile strength, e) strain-to-failure. f) work-to-fracture and g) slope after yield point. All data is presented with standard deviation.
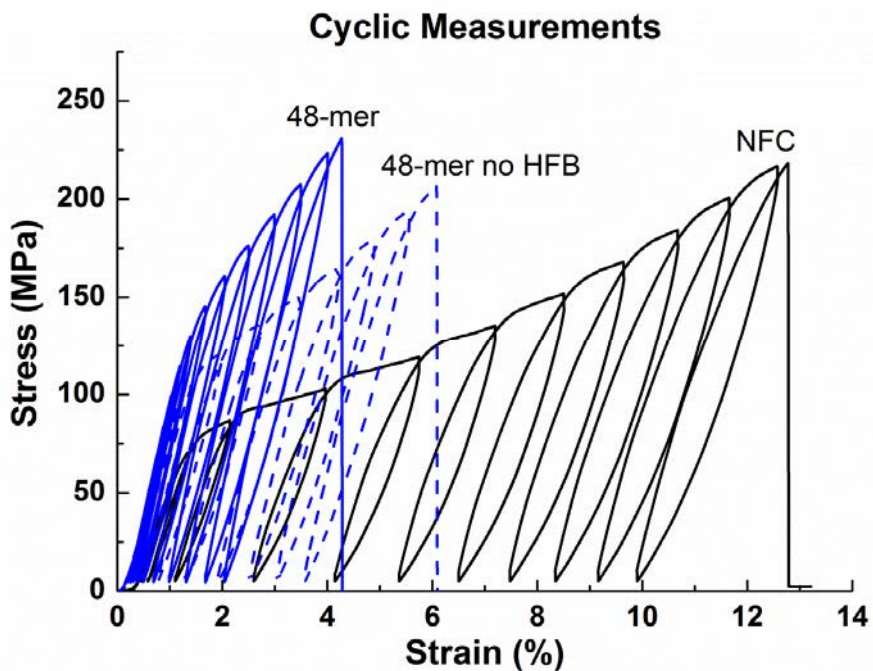
Figure S5. Representative stress-strain curves for HFBI-DCBD-C hybrid (solid blue line), DCBD-C hybrid (dashed blue line) and unmodified NFC film (solid black line) from the cyclic tensile measurements.
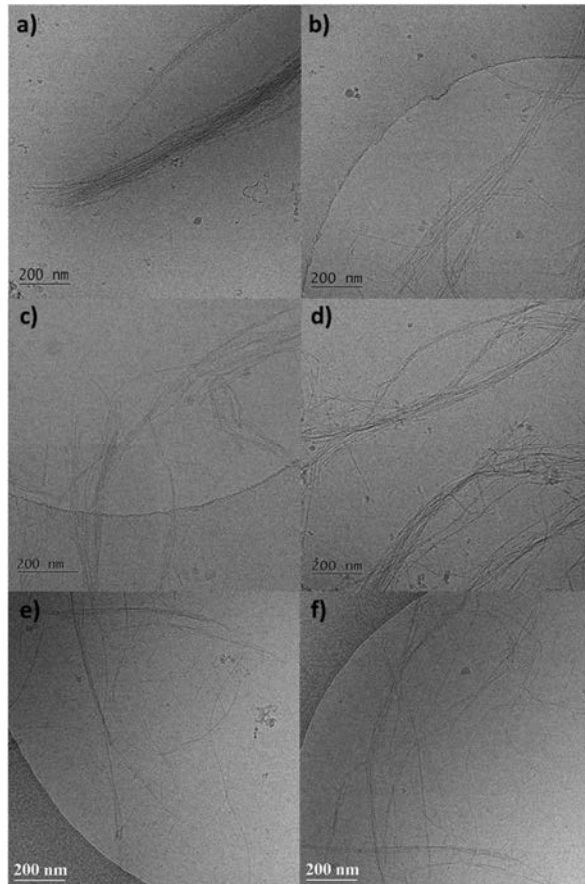
Figure S6. Cryo-TEM images of vitrified HFBI-DCBD-C and DCBD-C -NFC dispersions. a-b) Represent HFBI-DCBD-C-NFC dispersions, c-d) DCBD-C-NFC dispersions and e-f) unmodified NFC dispersions. Parts of individual nanofibers can be seen in all of the dispersions. Yet, in a-d) all of the nanofibers seem to be bound to other nanofibers, which is expected to result from biomolecular crosslinking of NFC nanofibers through HFBI-DCBD-C and DCBD-C proteins. The amounts of HFBI-DCBD-C and DCBD-C are $0.85gl^{-1}$ and the amount of NFC is $2.0gl^{-1}$. The unmodified NFC nanofibers display also aggregations. However, individual nanofibers can be seen were as the protein-containing dispersion were more aggregated with no individually dispersed nanofibers. The results are qualitative as the NFC nanofibers tend to aggregate natively.

[1] M. Pääkkö, M. Ankerfors, H. Kosonen, A. Nykänen, S. Ahola, M. Österberg, J. Ruokolainen, J. Laine, P. T. Larsson, O. Ikkala, T. Lindström, *Biomacromolecules* **2007**, *8*, 1934-1941.

[2] J. Hakanpää, G. R. Szilvay, H. Kaljunen, M. Maksimainen, M. Linder, J. Rouvinen, *Protein Science* **2006**, *15*, 2129-2140.

[3] M. Linder, I. Salovuori, L. Ruohonen, T. T. Teeri, *Journal of Biological Chemistry* **1996**, *271*, 21268-21272.

[4] M. B. Linder, M. Qiao, F. Laumen, K. Selber, T. Hyytiä, T. Nakari-Setälä, M. E. Penttilä, *Biochemistry* **2004**, *43*, 11873-11882.

[5] J. Phan, A. Zdanov, A. G. Evdokimov, J. E. Tropea, H. K. Peters, R. B. Kapust, M. Li, A. Wlodawer, D. S. Waugh, *Journal of Biological Chemistry* **2002**, *277*, 50564-50572.

[6] A. Sarrion-Perdigones, E. E. Falconi, S. I. Zandalinas, P. Juárez, A. Fernández-del-Carmen, A. Granell, D. Orzaez, *PLoS ONE* **2011**, *6*, e21622.

[7] M. Linder, K. Selber, T. Nakari-Setälä, M. Qiao, M. R. Kula, M. Penttilä, *Biomacromolecules* **2001**, *2*, 511-517.

Formation of ceramophilic chitin and biohybrid materials enabled by a genetically engineered bifunctional protein

ChemComm

COMMUNICATION

Formation of ceramophilic chitin and biohybrid materials enabled by a genetically engineered bifunctional protein†

Jani-Markus Malho,[a] Hanna Heinonen,[a] Inkeri Kontro,[b] Ngesa E. Mushi,[c] Ritva Serimaa,[b] Hans-Peter Hentze,‡[a] Markus B. Linder*[ad] and Géza R. Szilvay*[a]

A bifunctional protein composed of a highly negatively charged oyster shell protein and a chitin-binding domain enabled the formation of biohybrid materials through non-covalent surface modification of chitin nanofibres. The results demonstrate that specific biomolecular interactions offer a route for the formation of biosynthetic materials.

Many materials in biological systems have remarkable mechanical properties, yet their material components are held together by weak interactions.[1] Cohesiveness between the components is an essential factor that contributes to the formation of strong materials from relatively weak components.[2] The key to the cohesive role of proteins in materials may be their multifunctionality afforded by multi-domain structures. Protein domain duplication and shuffling is an important mechanism in the evolution of new biological functions.[3] Each domain has a specialized function that can together contribute to the macroscopic material properties. Understanding the role of multifunctional proteins in the materials can provide new important insight into the architecture of biological materials and into the development of synthetic materials inspired by biology.[4]

In Nature, biomineralization is an efficient way to create stiff and tough materials using genetic information.[5] A careful control of the crystal polymorph, size and shape is achieved using multiple weak interactions. In nacre, for example, brittle aragonite $CaCO_3$ platelets are combined with proteins and chitin to form a mechanically superior material.[6] Therein, a number of multifunctional proteins have been identified that

seem to interact with $CaCO_3$ aragonite platelets and an extra-cellular organic matrix, which may lead to cohesion in this material.[7–9] Consequently, multifunctional proteins seem to be contributing to the mechanical properties of natural materials.[2,10]

There is an ongoing effort to mimic these structures for creating novel synthetic materials with already promising results.[11–14] Many recent studies have highlighted approaches to mimic natural materials structurally and mechanically.[15–18] However, mimicking Nature's design principles for guiding the construction of synthetic materials is as important as the final structures and functions. In this work we show how a genetically engineered bifunctional protein can be employed to self-assemble novel biomimetic materials *via* surface functionalization of chitin nanofibres with a mineralization domain. Importantly, our study highlights the direct relationship between specific molecular interactions and the mechanical properties of a material *via* molecular self-assembly and biological interactions.

We engineered a hybrid protein with two separate functionalities, one for binding chitin and one for interacting with cations and minerals. The hybrid protein contains a chitin-binding domain (ChBD) from a bacterial chitinase enzyme[19] and a fragment of aspein, a shell-specific protein from the pearl oyster *Pinctada fucata*.[20] The aspein gene from the pearl oyster was chosen because of its unusually high aspartate residue content and thus highly acidic nature, herein containing a block of 16 (28%) negatively charged residues (Fig. 1a). A synthetic gene encoding a fusion of the ChBD and aspein fragment (residues 20–77) was expressed in *Escherichia coli* and the resulting protein was purified as described in the ESI.†

First the functions of both protein blocks were assessed separately. A chitin-binding assay showed that ChBD–aspein bound to the chitin substrate as expected with a similar association constant as reported for an isolated ChBD (Fig. 1b).[21] For determining the effect of ChBD–aspein on $CaCO_3$ mineralization, a double-jet experiment was performed, where a controlled and simultaneous addition of $CaCl_2$ and Na_2CO_3 solutions resulted in rapid nucleation of homogeneous crystals.[22] The formed crystals where washed and dried, and then imaged using SEM. In the presence of ChBD–aspein,

[a] *VTT Technical Research Centre of Finland, PO Box 1000, 02044 VTT, Finland. E-mail: geza.szilvay@vtt.fi*

[b] *University of Helsinki, Department of Physics, PO Box 64, 00014 HU, Finland*

[c] *Royal Institute of Technology, Fibre and Polymer Technology, SE-100 44 Stockholm, Sweden*

[d] *Aalto University, Department of Biotechnology and Chemical Technology, PO Box 16100, 00076 Aalto, Finland. E-mail: markus.linder@aalto.fi*

‡ Present address: DuPont Nutrition & Health, Edwin Rahrs Vej 38, DK-8220 Brabrand, Denmark.

Chem. Commun.
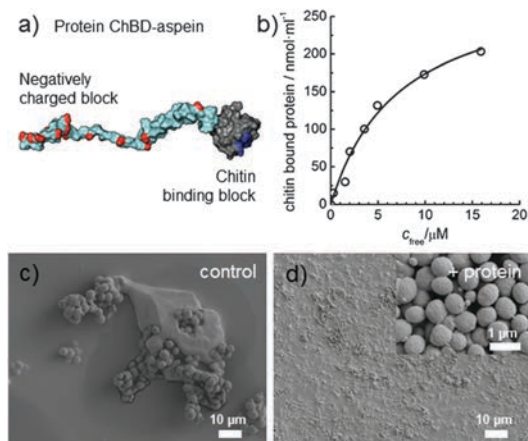
Fig. 1 Interaction of the bifunctional protein ChBD–aspein with chitin and the influence on CaCO₃ mineralization. (a) Molecular model of ChBD–aspein generated using the NMR structure of ChBD and a model structure of the aspein fragment.[23,24] This model should be considered as an aid in visualizing the relative dimensions of the protein and not as a detailed structural view. (b) Chitin-binding isotherm of ChBD–aspein protein. (c, d) CaCO₃ mineralization in the presence (d) and absence of ChBD–aspein (c) observed using SEM.

the mineral particles had a uniform size of about 0.5–1 μm in diameter, in contrast to control samples where the particle size was about an order of magnitude larger (Fig. 1c and d). All the formed crystals were CaCO₃ vaterite according to powder X-ray diffraction analysis. While the crystal polymorph was not affected under these conditions (absence of Mg²⁺-ions), the protein had a clear influence on the morphology of the formed crystals.

ChBD–aspein binding to chitin introduces a net charge of −15 in an area of about 3 nm² to the polysaccharide surface (at pH 8). This very high local negative charge on the chitin surface should attract positive ions and render chitin "ceramophilic". CaCO₃ mineralization was performed in the presence of ChBD–aspein decorated chitin beads and unmodified beads. Optical microscopy showed that in solution the formed crystals were preferentially bound to the ChBD–aspein functionalized beads and not to the unmodified beads (Fig. S3, ESI†). Taken together, the results show that ChBD–aspein binds to chitin and affects CaCO₃ crystal morphology.

Chitin functionalization requires typically covalent chemical modifications that can change the original structure and properties of the fibres. We set out to explore how genetically engineered proteins can be used to non-covalently functionalize chitin nanofibres. ChBD–aspein functionalized and negatively charged chitin should readily interact with cations and especially with Ca²⁺ via aspartate residues. We used lobster shells as the chitin source and produced chitin nanofibres by passing the material several times through a microfluidizer (see ESI†). The chitin dispersion was stable, yet some aggregation was observed as native chitin is hydrophobic in nature (Fig. S4a, ESI†).

Films were created from chitin nanofibre suspensions by vacuum filtration with and without CaCl₂, where the amount of

added ChBD–aspein was 50 wt% in relation to the chitin nanofibres. The presence of bound ChBD–aspein improved the stability of the nanofibre dispersion, likely due to repulsive forces afforded by the high local negative charge on the nanofibre surface. All samples produced a translucent solid film with a thickness of about 3–5 μm.

Tensile testing (see ESI†) showed that the mechanical properties of unmodified chitin nanofibre films were comparable with previously reported chitin and chitin based nanocomposites.[25] Films prepared from nanofibrillated chitin suspensions containing both ChBD–aspein and Ca²⁺ ions showed 80% increased stiffness (7.1 GPa modulus) compared to the unmodified chitin film (4 GPa) (Fig. 2). Moreover, the ultimate tensile strength of these films was 120 MPa which is 70% higher than that of the unmodified chitin films. Interestingly, films that were prepared identically but in the absence of Ca²⁺ ions showed no enhancement in strength and only a minor increase in stiffness as compared to the control.

The presence of Ca²⁺ ions in the films was confirmed by SEM with energy dispersive X-ray spectroscopy (EDX) imaging. The EDX spectrum of a cross section of a chitin film composed of ChBD–aspein and Ca²⁺ shows a clear peak for calcium (Fig. S4b, ESI†). Thus, the results indicate that the observed improved mechanical properties induced by Ca²⁺ ions arise from ionic interactions between the multiple binding sites introduced by ChBD–aspein and divalent ions. Similarly, randomly distributed ionic bonds have previously been suggested to play a role in providing sacrificial bonds in biological and biomimetic materials.[12,26]

Encouraged by the finding that ChBD–aspein could functionalize chitin nanofibres and form modified materials through multivalent ionic interactions, we attempted to form CaCO₃ minerals within the chitin/ChBD–aspein matrix by biomimetic mineralization. Using the double-jet setup, CaCl₂ and Na₂CO₃ solutions were introduced into a suspension of nanofibrillated
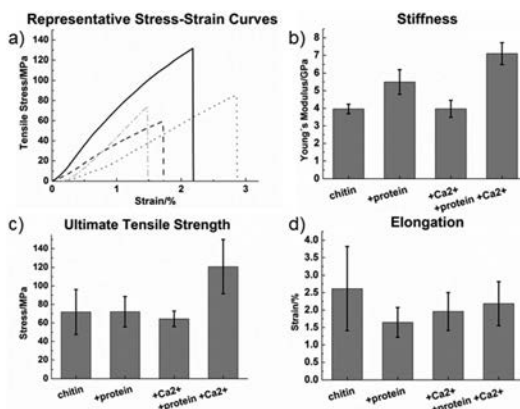
Fig. 2 Mechanical properties of bioinspired materials formed from nanofibrillated chitin and the ChBD–aspein protein in the presence of CaCl₂. Representative stress–strain curves (a) are shown for unmodified chitin nanofibres (dotted grey line), chitin and ChBD–aspein (dash dotted grey line), chitin and Ca²⁺ (dashed grey line), as well as chitin and ChBD–aspein with Ca²⁺ (solid black line) films. Average values with standard deviations of the material stiffness (b), ultimate tensile strength (c) and strain-to-failure (d) are shown.
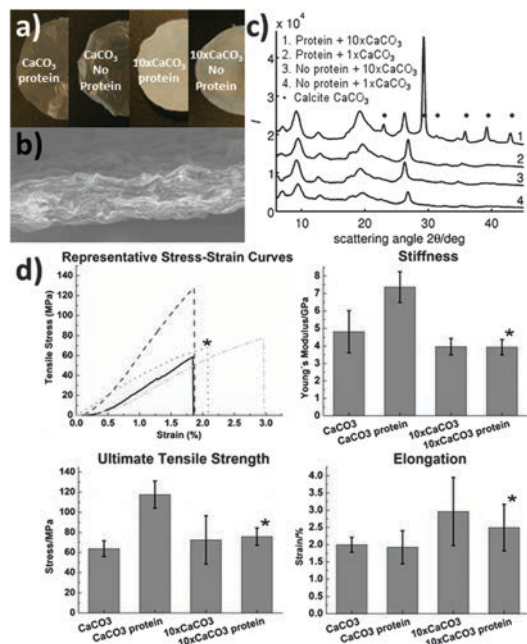
Fig. 3 Biomimetic CaCO$_3$ mineralization within the chitin nanofibre scaffold. (a) Mineralized films formed with or without the ChBD–aspein protein prepared from suspensions containing 0.6 (1×) or 6.0 mM (10×) CaCl$_2$ and Na$_2$CO$_3$. (b) A cross-sectional SEM image of the ChBD–aspein functionalized chitin film prepared with 10× CaCO$_3$. (c) Scattering intensities of the films obtained using WAXS. Characteristic peaks for calcite CaCO$_3$ are marked with black dots. (d) Mechanical properties of the chitin nanofibre-based films. Representative stress–strain curves are for samples prepared with 1× CaCO$_3$ (solid line), 1× CaCO$_3$ with protein (dashed line), 10× CaCO$_3$ (dash-dotted line), and 10× CaCO$_3$ with protein (dotted line). Average values with standard deviations of stiffness, ultimate tensile strength and strain-to-failure are also shown. Films shown to contain mineral crystals are marked with an asterisk.

chitin functionalized with the ChBD–aspein protein. Freestanding films were prepared from the dispersions and analysed for the presence and type of polymorph of CaCO$_3$ minerals by wide angle X-ray scattering (WAXS) and mechanical properties by a tensile tester (Fig. 3).

WAXS peaks for crystalline chitin were observed in all samples as expected. When about an equimolar amount of Ca^{2+} (and CO$_3^{2-}$) in relation to carboxyl groups in the ChBD–aspein functionalized chitin nanofibres was introduced no CaCO$_3$ crystals were observed (Fig. 3c). This indicates that at these low salt concentrations the carbonate ions were outcompeted by the protein carboxyl groups and Ca^{2+} ions preferentially bound to the latter, thus preventing mineralization. As observed earlier in the films prepared without CO$_3^{2-}$ ions (see Fig. 2), it is likely that the bound Ca^{2+} ions form multiple ionic interactions within the matrix. This was observed in the form of enhanced mechanical properties (Fig. 3d). However, using a 10-fold excess of Ca^{2+} and CO$_3^{2-}$ ions resulted in retention of CaCO$_3$ crystals within the matrix when ChBD–aspein was present as shown by the characteristic scattering peaks.
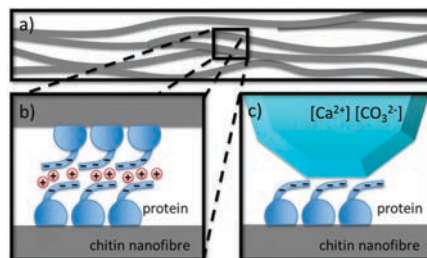

Fig. 4 Schematic presentation of the formed chitin-based nanocomposites. (a and b) The bifunctional ChBD–aspein protein confers negative charge to the chitin nanofibres and thus improves the dispersion stability and attracts Ca^{2+}-ions. The cations provide multiple ionic interactions across the chitin network and thus enhance the mechanical properties through improved and increased interactions in the chitin network. (c) ChBD–aspein protein on chitin provides nucleation sites for CaCO$_3$ crystallization and enables the retention of formed crystals within the chitin nanofibre matrix.

The crystal polymorph was identified as calcite based on the peak pattern and a crystal size of 50.2 ± 1.2 nm in the (104) direction was obtained. The presence of calcium within the film cross section was verified using EDX spectroscopy (Fig. 3b Fig. S5 and S6, ESI†). To verify that the incorporation of CaCO$_3$ within the film was enabled by the ChBD–aspein, a film without the protein was prepared, and, as expected, no detectable CaCO$_3$ peaks were observed in WAXS.

The film that was shown to retain CaCO$_3$ minerals (ChBD–aspein and 10× CaCO$_3$) surprisingly maintained its stiffness and strength as compared to plain chitin films (Fig. 3d). Incorporation of relatively large crystals in the chitin network potentially could have reduced the strength by disturbing the well-percolated fibre network.[27] However, this was not observed in our system, indicating the formation of a well-integrated hybrid material. The results show that biomimetic mineralization via the ChBD–aspein protein enabled the retention of CaCO$_3$ mineral particles within the chitin nanofibre network. The role of ChBD–aspein may be in interfacing the minerals with the chitin network and providing cohesion between the components. The shape and size of mineral particles are likely to have a major influence on the mechanical properties; however, these parameters were not controlled in this study.

In this work we have shown how a genetically engineered protein was used for the construction of two biomimetic hybrid materials. Considerable improvements in mechanical properties of the chitin network were achieved by introducing surface charges and counter ions thereby creating cohesion in the material through multivalent ionic interactions. Furthermore, the high density of charged groups introduced by the engineered protein enabled the formation and retention of biomimetic CaCO$_3$ crystals within the chitin matrix. A schematic view of the functionalized "ceramophilic" chitin is shown in Fig. 4. We believe that a control over the crystal size and shape, and the self-assembly at longer length scales will yield improved mechanical performance in the future.

The work herein demonstrates that simple but specific functionalities found in biology combined with multifunctional proteins can be utilized in the development of novel biohybrid materials for *e.g.* biomedical applications. We anticipate that the highly specific functions found in biology can be applied to self-assembly concepts in supramolecular chemistry yielding future materials that reach and exceed the properties of natural materials.

Notes and references

1 M. J. Buehler, *Nano Today*, 2010, **5**, 379–383.
2 J. W. C. Dunlop, R. Weinkamer and P. Fratzl, *Mater. Today*, 2011, **14**, 70–78.
3 C. Vogel, M. Bashton, N. D. Kerrison, C. Chothia and S. A. Teichmann, *Curr. Opin. Struct. Biol.*, 2004, **14**, 208–216.
4 P. Laaksonen, G. R. Szilvay and M. B. Linder, *Trends Biotechnol.*, 2012, **30**, 191–197.
5 M. A. Meyers, P. Y. Chen, A. Y. M. Lin and Y. Seki, *Prog. Mater. Sci.*, 2008, **53**, 1–206.
6 L. Addadi, D. Joester, F. Nudelman and S. Weiner, *Chem. – Eur. J.*, 2006, **12**, 981–987.
7 J. S. Evans, *Bioinformatics*, 2012, **28**, 3182–3185.
8 G. Falini, S. Albeck, S. Weiner and L. Addadi, *Science*, 1996, **271**, 67–69.
9 M. Suzuki, K. Saruwatari, T. Kogure, Y. Yamamoto, T. Nishimura, T. Kato and H. Nagasawa, *Science*, 2009, **325**, 1388–1390.
10 G. E. Fantner, T. Hassenkam, J. H. Kindt, J. C. Weaver, H. Birkedal, L. Pechenik, J. A. Cutroni, G. A. G. Cidade, G. D. Stucky, D. E. Morse and P. K. Hansma, *Nat. Mater.*, 2005, **4**, 612–616.
11 H. Cölfen and S. Mann, *Angew. Chem., Int. Ed.*, 2003, **42**, 2350–2365.
12 A. Walther, I. Bjurhager, J.-M. Malho, J. Ruokolainen, L. Berglund and O. Ikkala, *Angew. Chem., Int. Ed.*, 2010, **49**, 6448–6453.
13 B. Wicklein and G. Salazar-Alvarez, *J. Mater. Chem. A*, 2013, **1**, 5469–5478.
14 J. D. Hartgerink, E. Beniash and S. I. Stupp, *Science*, 2001, **294**, 1684–1688.
15 P. Laaksonen, A. Walther, J. M. Malho, M. Kainlauri, O. Ikkala and M. B. Linder, *Angew. Chem., Int. Ed.*, 2011, **50**, 8688–8691.
16 A. Walther, I. Bjurhager, J. M. Malho, J. Pere, J. Ruokolainen, L. A. Berglund and O. Ikkala, *Nano Lett.*, 2010, **10**, 2742–2748.
17 M. Gungormus, M. Branco, H. Fong, J. P. Schneider, C. Tamerler and M. Sarikaya, *Biomaterials*, 2010, **31**, 7266–7274.
18 U. O. S. Seker, V. K. Sharma, S. Akhavan and H. V. Demir, *Langmuir*, 2014, **30**, 2137–2143.
19 T. Watanabe, Y. Ito, T. Yamada, M. Hashimoto, S. Sekine and H. Tanaka, *J. Bacteriol.*, 1994, **176**, 4465–4472.
20 T. Takeuchi, I. Sarashina, M. Iijima and K. Endo, *FEBS Lett.*, 2008, **582**, 591–596.
21 M. Hashimoto, T. Ikegami, S. Seino, N. Ohuchi, H. Fukada, J. Sugiyama, M. Shirakawa and T. Watanabe, *J. Bacteriol.*, 2000, **182**, 3045–3054.
22 M. Sedlák, M. Antonietti and H. Cölfen, *Macromol. Chem. Phys.*, 1998, **199**, 247–254.
23 T. Ikegami, T. Okada, M. Hashimoto, S. Seino, T. Watanabe and M. Shirakawa, *J. Biol. Chem.*, 2000, **275**, 13654–13661.
24 K. T. Simons, C. Kooperberg, E. Huang and D. Baker, *J. Mol. Biol.*, 1997, **268**, 209–225.
25 S. Ifuku and H. Saimoto, *Nanoscale*, 2012, **4**, 3308–3318.
26 M. A. Hartmann and P. Fratzl, *Nano Lett.*, 2009, **9**, 3603–3607.
27 Z. R. Min, Q. Z. Ming, X. Z. Yong and M. Z. Han, *Polymer*, 2001, **42**, 3301–3304.

Supporting Information

Ceramophilic chitin and biohybrid materials enabled by a genetically engineered bifunctional protein

Jani-Markus Malho[†], Hanna Heinonen[†], Inkeri Kontro[‡], Ngesa E. Mushi[§], Ritva Serimaa[‡], Hans-Peter Hentze[†⊥], Markus B. Linder[†‖]*, Géza R. Szilvay[†]*

[†] VTT Technical Research Centre of Finland, PO Box 1000, 02044 VTT, Finland
[‡] University of Helsinki, Department of Physics, PO Box 64, 00014 HU, Finland
[§] Royal Institute of Technology, Fibre and Polymer Technology, SE-100 44 Stockholm, Sweden
[‖] Aalto University, Department of Biotechnology and Chemical Technology, PO Box 16100, 00076 Aalto, Finland

Materials and Methods

Gene construct

The aspein gene DNA sequence from *Pinctada fucata* was codon optimized and sequence repetitiveness reduced for *E. coli* expression. A synthetic gene was ordered from GeneArt (Life Technologies) where the sequence for the chitin binding domain[1] was fused to the optimized aspein *via* a linker encoding GGSGGS amino acid sequence. The gene was flanked with BsaI restriction sites for "Golden gate" cloning into the plasmid vector pGBtacLacZ.[2] The insertion replaces the lacZ gene with the synthetic gene under the control of the tac promoter and downstream of pelB signal sequence for periplasmic expression. The sequence of the resulting plasmid pGG-ChBD-aspein20-77 was verified by sequencing (Macrogen, Netherlands). Protein expression levels in various *E. coli* strains were low. Thus, the construct without the pelB signal sequence was inserted as an NcoI/HindIII fragment into pET-28b(+) (Novagen) resulting in plasmid pET-ChBD-asp20-77 where the construct is under the *lac* repressor controlled T7*lac* promoter. The plasmid was then transformed into XL1Blue strain, sequenced and finally transformed into BL21Star(DE3) strain (Invitrogen)[3] that contains the T7 RNA polymerase needed for the expression. The amino acid sequence of ChBD-aspein is shown in Figure S1.

Figure S1. Amino acid sequence of ChBD-aspein. The chitin binding domain, linker and aspein fragment are indicated. Residues that have a negative or positive charge at pH 8 are colored red and blue, respectively.

Protein production and purification

The protein ChBD-aspein was expressed from the plasmid pET-ChBD-asp20-77 by induction using 0.5 mM isopropyl β-D-1-thiogalactopyranoside at 37°C. Pelleted cells were resuspended in 20 mM bis-Tris buffer at pH 5.5 containing protease inhibitors (Complete EDTA-free, Roche). The cells were lysed by passing through a French press and the nucleic acids were removed by addition of nucleases (New England Biolabs). After centrifugation to remove cell debris the solution was applied to a HiTrap DEAE

FF anion exchange column (GE Healthcare) equilibrated to the sample buffer at pH 5.5 and eluted using a linear NaCl-gradient (20 mM bis-Tris buffer at pH 5.5 containing 1 M NaCl). Fractions containing the protein were pooled and further purified with reversed phase chromatography using a Vydac C4 column (Grace). A linear acetonitrile gradient (10 – 65 %) was used to fractionate the sample. Fractions containing the protein were pooled and freeze-dried. The yield of pure protein was about 50 mg per L of culture.

Chitin binding assay

Protein at different concentrations were added to washed chitin beads (New England biolabs) in 20 mM Hepes buffer at pH 8.5 containing 500 mM NaCl and incubated 1 h at room temperature. The unbound protein was separated from the chitin beads by centrifugation and the amount of unbound protein was determined using the BCA-assay (Pierce) and compared to a standard curve.

Chitin production and isolation

Fresh frozen lobsters were obtained from the market in Stockholm (CoopExtra, Sweden) as the starting materials for preparation of chitin nanofibres. The lobsters were washed in water to remove tissues and salts. The exoskeleton shells were freeze dried and crushed to powder in order to increase surface area for further chemical and mechanical treatments.

Chitin nanofibres were disintegrated from lobster exoskeleton. The powder from the lobster exoskeleton shells was demineralized against 2 M HCl for 2 hr. The demineralized powder was soaked overnight in 96% ethanol to remove pigments. Then, treatment to remove protein was performed with 20% concentration of NaOH for 2 weeks. All treatments were carried out at room temperature. The colloidal suspension was blended at pH 3 in the presence of acetic acid by a powerful kitchen blender (VM0105E, USA) and thereafter homogenized by passing 10 times through the microfluidizer (Microfluidics, USA); five times through 400 and 200 μm chambers and then, five times through 200 and 100 μm chambers.

Biomimetic mineralization in solution

Mineral precursors $CaCl_2$ (0.5 M, aq) and Na_2CO_3 (99.5%) as well as NaOH were obtained from Sigma Aldrich and used without purification. Purified MilliQ water (18.2 mΩ) (Millipore) was used for dilutions. The mineralization of $CaCO_3$ was carried out in a glass beaker at room temperature. Aqueous solutions of 0.05 M $CaCl_2$ and 0.05 M Na_2CO_3 were prepared from feedstock. ChBD-aspein proteins were diluted into water with total volume of 45 ml and the pH of the solution was adjusted to pH 8 by using 0.1 M NaOH. $CaCl_2$ and Na_2CO_3 solutions were added into the protein solution simultaneously and slowly by two syringe pumps for measuring accurate volume dosage and to maintain even 40 ml/h flow. The solution was mixed with magnetic stirrer while adding precursor solutions. After addition of precursors the solution was stirred for ten minutes. One droplet of the solution was taken on the microscope glass and analysed using light microscope (Olympus BH-2). Crystals were centrifuged and washed with water three times. Few droplets of washed crystals in water were air dried on carbon tape for SEM measurements. Rest of the washed crystals were air dried overnight for XRD measurements.

Film preparation

For preparing self-standing films CaCO3 mineralization was performed the same way as the mineralization in solution (above), but performed in chitin nanofibre suspension with or without

protein. Chitin nanofibres and proteins were diluted into water with total volume of 5 ml in a glass beaker, where the pH was adjusted to 8. Then 500 Joules was applied to the chitin nanofibre dispersions via tip sonicator (Vibra-Cell VCX 750, Sonics & Materials Inc.) to enhance the dispersity of the nanofibres. The used power was 40 % of the full output power. Varying the concentrations of $CaCl_2$ and Na_2CO_3, the solutions were measured out via syringe pumps keeping the flow at 10 ml/h. The dispersion was kept under magnetic stirring during the salt solution dosing; furthermore the dispersions were allowed to stabilize 10 minutes under magnetic stirring. Vacuum filtration was used to create the films from 5 ml of dispersions by the removal of water and buffer solution. The dispersions were filtrated using a Durapore membrane (GVWP, 0.22 μm, millipore, U.S.A.) and an O-ring, wherein the O-ring was used to determine the diameter of the films. After filtration the films were pressed gently with a 300 g load for 10 min to prevent wrinkling. Films were dried overnight in oven at +40°C.

Preparation of the Ca^{2+}-films was performed as explained above (biomineralized films) with the exception that only $CaCl_2$ was added by pipetting it to the chitin and chitin-protein dispersions after sonication. After addition of the $CaCl_2$ the dispersion was allowed to stabilize before vacuum filtration.

Scanning electron microscopy (SEM)

SEM (JEOL JSM7500FA field emission microscope, Japan) was carried out to image the cross-sections of the films and dried dispersion of $CaCO_3$ crystals using acceleration voltages of 2-15 kV depending on the sample. A thin Pd or Au-Pd layer was sputtered on top of the samples (Emitech K950X/K350, Quorum Technologies Ltd., Kent, UK). JSM-7500FA is also equipped with a JEOL energy-dispersive X-ray (EDX) analysis. Spectra were taken over 2 min using 15 keV electron energy to analyse the composition of samples.

Wide angle X-ray scattering (WAXS)

The measurements were done with the wide angle X-ray scattering (WAXS) set-up of the Laboratory of Electronic structure, University of Helsinki. The X-rays were produced with a conventional copper anode X-ray tube with point focus. Monochromatization was done with collimating Montel optics (Incoatec, Geesthacht, Germany) to obtain Cu-K_α radiation (wavelength λ=1.541 Å). The experiments were carried out in perpendicular transmission geometry with MAR345 image plate as detector (Marresearch, Norderstedt, Germany). The detector-to-sample distance was 8 cm.

The samples were layered two-fold on a sample holder and measured for 45 minutes. The angular calibration was done with lanthanum hexaboride and silver behenate samples. Intensities were corrected for absorption, geometry of the detector and air scattering.

The minimum crystal size s was calculated from the Scherrer formula:

$$s = \frac{0.9\lambda}{\sqrt{(\Delta 2\theta)^2 - (\Delta 2\theta_{inst})^2}\cos\theta} \tag{1}$$

where λ is the wavelength of the radiation, $\Delta 2\theta$ is the full width at half maximum (FWHM) for the diffraction peak, $\Delta 2\theta_{inst}$ is the instrumental broadening determined from the FWHM of the (110) reflection of a thin LaB_6 sample, and θ is half of the scattering angle.

Tensile testing

Tensile testing was performed on 5 kN Tensile/compression module (Kammrath & Weiss GmbH, Germany) using 100 N load cell with a nominal strain rate of 8.35 μm/sec (0.5 mm/min). The gauge length was 10 mm for all of the samples. At least 4 specimens were measured from each sample, with the exception of one sample (1x $CaCO_3$ + chitin), where the absence of protein ChBD-aspein degraded the film forming properties significantly. Thus only two samples could be prepared and measured with precision. Specimen sizes were 2 cm x 2 mm x 3-7 μm, length, width and thickness, respectively. Sample thicknesses were measured using linear gage (LGF-01100L-B transmission-type photoelectric linear encoder with EF-12PRH counter, Mitutoyo), herein at least 6 measurements from each sample was measured to calculate average value for thickness. The widths were measured with digital slide gauge (Digimatic, Mitutoyo). Samples were taken directly from oven into a desiccator from where the samples were transferred and attached to the tensile tester. Desiccator was kept in the relative humidity of ~30% and the tensile tester was held under humidity controlled box, where relative humidity was adjusted to ~30%.

Cryo-Transmission Electron microscopy (CryoTEM)

Chitin nanofibre dispersions were characterized with JEOLS JEM-3200FSC Cryo- Transmission Electron Microscope operating at liquid nitrogen temperature. Specimens were blotted and subsequently vitrified in a mixture of liquid ethane and propane (-180°C) for cryo-imaging using a vitrobot (FEI, U.S.A.). Zero-loss imaging of vitrified samples was carried out with JEOLS JEM-3200FSC 300 keV TEM with an energy filter using slit size of 20 eV.

Figures

Figure S2. Purity of the ChBD-aspein protein. Sodium dodecyl sulphate (SDS) polyacrylamide gel electrophoresis of cytosolically expressed, ion-exchange and reversed-phase purified ChBD-aspein. The identity of the single band was verified by western blot using an anti-ChBD antibody (NEB). The apparent molecular weight of ChBD-aspein is higher than the calculated 11 kDa based on the amino acid sequence. The very hydrophilic and charged nature of aspein may bind less SDS and thus have a non-standard electrophoretic mobility as has been reported before.[4] Molecular weight markers in kDa are indicated on left.
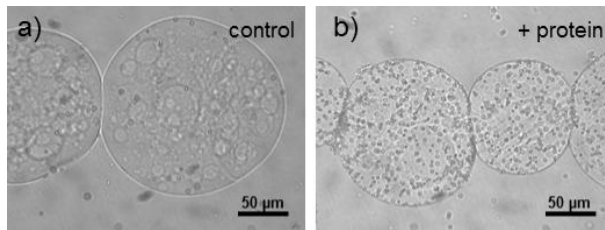
Figure S3. Optical microscopy shows that in solution the formed crystals are preferentially bound to the ChBD-aspein functionalized beads (b) and not to the unmodified beads (a).
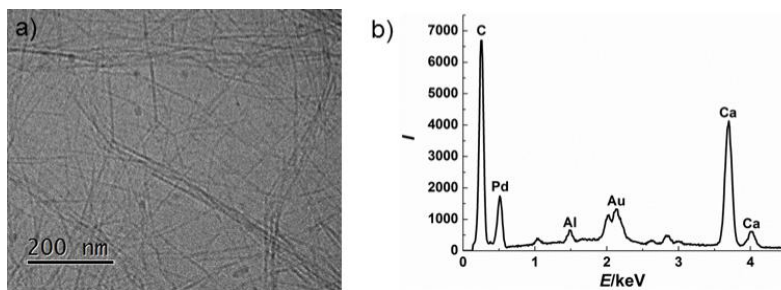
Figure S4. a) Cryo-TEM image of a vitrified dispersion of plain native chitin nanofibres. b) An EDX spectrum showing the presence of Ca^{2+}-ions in a ChBD-aspein modified chitin film formed from a suspension containing $CaCl_2$. X-axis is the energy in keV and y-axis is the intensity.
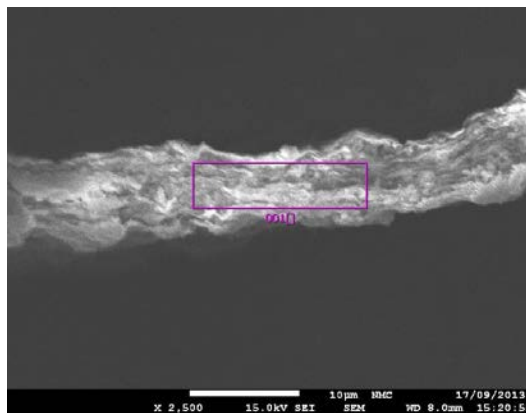
Figure S5. SEM-image of a cross-section from a $10xCaCO_3$-Chitin-ChBD-aspein-film. EDX-spectrum was recorded from the squared area.
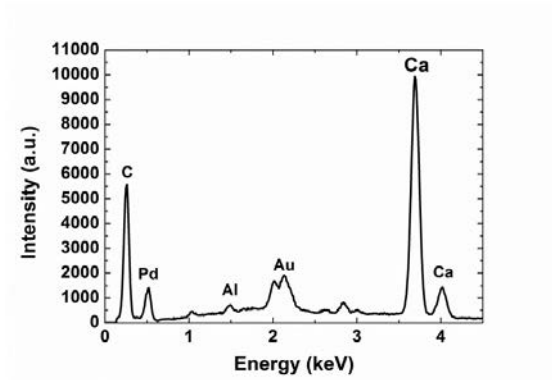
Figure S6. EDX-spectrum from the squared area in Figure S5.

References

[1]   T. Watanabe, Y. Ito, T. Yamada, M. Hashimoto, S. Sekine, H. Tanaka, *J Bacteriol* **1994**, *176*, 4465-4472.

[2]   a) C. Engler, R. Kandzia, S. Marillonnet, *PLoS One* **2008**, *3*, e3647; b) B. Gabryelczyk, G. R. Szilvay, M. Salomäki, P. Laaksonen, M. B. Linder, *Colloids Surf B Biointerfaces* **2013**, *110*, 66-73.

[3]   O. V. Makarova, E. M. Makarov, R. Sousa, M. Dreyfus, *Proc Natl Acad Sci U S A* **1995**, *92*, 12250-12254.

[4]   T. Takeuchi, I. Sarashina, M. Iijima, K. Endo, *FEBS Lett* **2008**, *582*, 591-596.

Facile Method for Stiff, Tough, and Strong Nanocomposites by Direct Exfoliation of Multilayered Graphene into Native Nanocellulose Matrix

Facile Method for Stiff, Tough, and Strong Nanocomposites by Direct Exfoliation of Multilayered Graphene into Native Nanocellulose Matrix

Jani-Markus Malho,[†] Päivi Laaksonen,*[,†] Andreas Walther,[‡] Olli Ikkala,[§] and Markus B. Linder[†]

[†]VTT Technical Research Centre of Finland, Tietotie 2, P.O. Box 1000, FI-02044, Espoo, Finland

[‡]DWI at RWTH, Aachen University, Forckenbeckstr. 50, D-52056, Aachen, Germany

[§]Molecular Materials, Aalto University (formerly Helsinki University of Technology), P.O. Box 15100, FI-00076 AALTO, Espoo, Finland

ABSTRACT: Nanofibrillated cellulose (NFC) is a natural fibrillar material with exceptionally high mechanical properties. It has, however, been exceedingly difficult to achieve nanocomposites with drastically improved mechanical properties by dispersing NFC as random networks to polymer matrices, even using compatibilization. We show nanocomposites consisting of aligned assemblies of multilayered graphene and NFC with excellent tensile mechanical properties without any surface treatments. The optimum composition was found at 1.25 wt % graphene

Dispersion of multi-layered graphene in nanocellulose hydrogel

Nanocomposite films by vacuum filtration

multilayers, giving a Young's modulus of 16.9 GPa, ultimate strength of 351 MPa, strain of 12%, and work-of-fracture of 22.3 MJ m^{-3}. This combines high strength with relatively high toughness and is obtained by direct exfoliation of graphite within aqueous hydrogels of NFC where an optimum sonication power is described. The results suggest the existence of an attractive interaction between multilayered graphene flakes and cellulose. Aligned assemblies are obtained by removal of water by filtration. The concept can be beneficial for applications because it results in high mechanical properties by a simple and environmentally green process.
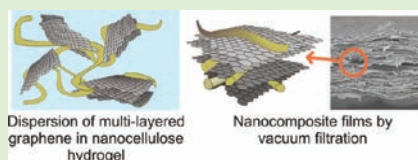
■ INTRODUCTION

Nature shows several types of nanocomposite materials with excellent properties that are difficult to obtain in conventional manmade composites.[1] Representative examples are pearl of nacre and silk, which are based on aligned assemblies of hard reinforcing and soft dissipative domains, leading to unique combinations of stiffness, strength, and toughness. On the other hand, also wood and plant cell wall materials show remarkable multifunctionality and adaptability due to their reinforcing native cellulose nanofibrils (nanofibrillated cellulose, NFC, also called microfibrillated cellulose, MFC) as hierarchically embedded in soft matrix at controlled pitches.[2] By understanding the essential features of biological materials, improved properties may be designed in synthetic materials. This approach of learning from nature is called biomimetics.[3−9] It involves several scientific challenges but can result in technologically promising materials.[10−15]

Toward biomimetic constructs, macroscopic pulp fibers can be mechanically disintegrated into NFC usually also involving pretreatments,[16−20] which have excellent mechanical properties.[2] These nanofibrils have a width of 5−30 nm and total length up to about 5 μm. They consist of mostly native crystalline cellulose regions separated by short amorphous domains according to the fringed fiber model. Upon disintegration from pulp, NFC usually forms hydrogels.[21] Thus, an efficient and economical exploitation of native NFC involves processing in aqueous environment to limit heavy

agglomeration of strongly hydrogen-bonding nanofibrils in nonpolar media. Creating a solid composite from aqueous NFC suspension requires the removal of water, leading to a network structure due to the capillary forces that introduce an attraction between fibrils. Multiple molecular level interactions such as hydrogen bonds bind the nanofibrils together.[22] NFC fibrils are considered one of the most interesting and promising renewable materials for applications such as aerogels,[23,24] nanopaper,[13] fibers,[25,26] composites,[27−30] and other hybrid materials.[31,32]

Graphene[33] is another feasible material for nanocomposites due to its high stiffness and strength.[34,35] Graphene can be produced by micromechanical cleavage,[36] by growth of monolayers of graphene[37,38] or by exfoliation from graphite.[39−42] In addition, some production steps result in graphene derivatives, such as graphene oxide.[43] Production of graphene is still a bottleneck for its efficient large scale utilization, especially for composites. Dispersing graphene effectively in composite materials is expected to enable low-cost solutions[44] for sustainable and lightweight materials. Recently many composites using graphene have been reported, especially with different polymers.[43,45] However, facile and robust techniques

for nanocomposites with superior mechanical properties are still being sought.

We showed recently that graphene can improve the properties of NFC composites.[28] To achieve this, graphene flakes were exfoliated using an adhesive protein called hydrophobin.[46,47] The hydrophobin was genetically modified so that a cellulose binding part was joined to it. In the nanocomposite, the hydrophobin bound to graphene flakes and the cellulose binding part bound to nanofibrillated cellulose, and therefore this bifunctional protein could link the graphene and nanocellulose in the nanocomposite material. The linkage resulted in an increase in especially the stiffness and ultimate strength. The importance of the protein linkage to cellulose was shown by using also hydrophobin without the cellulose binding part, which resulted in much weaker materials.

Here we show that a strong, stiff, and tough sheet/fiber-nanocomposite based purely on graphene multilayers and NFC using a sonication process can be made. The work was based on the serendipitous finding that multilayers of graphene can be exfoliated directly from graphite to aqueous environment by using only NFC as the dispersing agent. Our lightweight nanocomposite introduces superior mechanical properties by some forms of physical interaction between NFC fibrils and graphene flakes, to be discussed later. The resulting aqueous suspensions were then vacuum filtrated to form solid composite materials. For simplicity, the dispersions of single or multi-layered graphene flakes are referred here as graphene dispersions, although there may be a range of flake thicknesses present. Remarkable improvements were observed in the mechanical properties in comparison to previous results reported on nanopaper and graphene nanocomposite materials.[21,29,48,49] We suggest that the physical interaction between NFC and graphene multilayers generates the basis for the excellent mechanical properties and highlights a novel way for graphene exfoliation.

■ EXPERIMENTAL SECTION

Material and Methods. *Exfoliation of Graphene Flakes.* A dilute hydrogel (solid content 1.9%) of UPM Fibrillar Cellulose (NFC; UPM-Kymmene Corporation, Finland) was used for graphene exfoliation. The sample preparation was done using mechanical disintegration of birch pulp by ten passes through a M7115 Fluidizer (Microfluidics Corp., U.S.A.) essentially according to previous reports.[19]

Powder of Kish graphite (Natural Kish Graphite (Grade 50), Graphene Supermarket, U.S.A.) was directly exfoliated to graphene flakes using a tip sonicator (Vibra-Cell VCX 750, 2 mm stepped microtip, Sonics and Materials Inc., U.S.A.). Sonication time was based on the amount of energy lead to the sample, which was monitored during the sonication using 60% of the full output power. Graphite granules were predispersed into a NFC solution (2.0 g L^{-1}), creating dispersion with relatively high concentration of graphene flakes, from which smaller amounts of graphene flakes could be dosed for further sonication. Thus, the amount of graphene that is reported, means the whole range of flakes containing single or several layers of graphene.

Preparation of Films. All of the suspensions and diluted dispersion were less than 3.5 mL in volume, because of the high viscosity of NFC lead to inefficient sonication of larger volumes. Graphene suspension having 1.0 g L^{-1} concentration of graphene and 2.0 g L^{-1} of NFC was first exfoliated with 6 kJ of energy. After exfoliation, the desired proportions of graphene/NFC dispersions were prepared by mixing with NFC suspension using sonication energy of 2.5 kJ. The NFC concentration was kept 2.0 g L^{-1} throughout the manufacturing process. Vacuum filtration was used to create the films from dispersions containing NFC and graphene multilayers. The dispersions were filtrated using a Durapore membrane (GVWP, 0.22 μm,

Millipore, U.S.A.). After filtration of the films a gentle press was applied to them using a 300 g load for 10 min to prevent wrinkling. Films were dried overnight in +65 °C.

Mechanical Testing. A mini tensile tester (Deben, UK) was used to perform mechanical tests. A 20 N load cell was used with a nominal strain rate of 0.5 mm/min, because of its optimal data range. At least 4 specimens were measured from each sample. Specimen sizes were 2 cm × 2 mm × 7–10 μm, length, width, and thickness, respectively. Mechanical testing was done in ambient conditions.

Characterization of the Samples. Micrometer slide calliper and optical microscope (LEO1560, Carl Zeiss Inc., U.S.A.) were used to determine the widths of the samples. The thicknesses were measured using scanning electron microscope (JEOL JSM-7500F FEG, Japan), where acceleration voltages of 1–15 kV were applied and varied depending on the sample. Samples for SEM imaging were sputtered with Pd to enhance imaging conditions and prevent the charging of a sample. Films were aligned perpendicular to the electron beam. The thickness of a film was determined by taking at least eight measures from different places of a film cross section. Graphene multilayers/NFC dispersions were characterized with JEOLS JEM-3200FSC Cryo-Transmission Electron Microscope. Specimens were vitrified on c-flat grids for cryo-imaging using a vitrobot (FEI, U.S.A.). Electron diffraction was measured with a TEM using a selected area aperture at diffraction mode (Tecnai 12, U.S.A.) instrument operating at a 120 kV accelerating voltage.

Raman Microscopy on the Composite Films. Composite films were characterized by confocal Raman microscopy (WITec Alpha 300 RA, Germany) with a 532 nm laser. By monitoring the intensity of the G band at 1544–1649 cm^{-1} or the D' band at 2644–2812 cm^{-1}, pieces of multilayered graphene and graphite could be easily located. Weak Raman bands at 1097 and 1107 cm^{-1} were associated with crystalline cellulose.[50]

■ RESULTS

NFC Matrix and Exfoliation of Graphene. The effect of the ultrasonication of NFC was studied first to see whether sonication causes the degradation of NFC fibrils. Therefore cellulose hydrogels were sonicated with different sonication energies, water was removed by filtration to prepare nano-papers and nanopaper mechanical properties were investigated using the sample size of about 2 mL aqueous suspension of NFC using a concentration of 2.0 g L^{-1}. A small sonication energy, ca. 6 kJ, was needed to open the NFC aggregates to reach a sufficient homogeneity of the NFC dispersion which resulted in rather high stiffness of 11.2 GPa and strength of 287 MPa. However, sonication energies higher than 6 kJ, (tested with 12 kJ and 18 kJ) did lead to a lower tensile strength and modulus values, 6.9 GPa and 190 MPa respectively.

It was serendipitously found that if graphite was added in the above-described procedure, the NFC did promote exfoliation of the graphite. A range of nominal amounts of graphite was used up to weight fraction of 50 wt % versus the weight of NFC. Sonication by 6 kJ was sufficient to disperse the graphite as an apparently homogeneous aqueous suspension into the NFC matrix. The suspensions of multilayered graphene flakes exfoliated in NFC hydrogels were found to be relatively stable, regardless of the amount of graphene, as no clear sedimentation was observed even after few months. A cryogenic transmission electron microscopy (cryo-TEM) image of a multilayered graphene flake embedded in a NFC matrix is shown in Figure 1a. The image was taken from a thin film of a vitrified suspension in cryogenic conditions, thus, the native state of the NFC fibrils and the multilayered graphene flakes were essentially preserved without further aggregation. The micrograph shows that graphite is indeed exfoliated to thin flakes consisting of only a few layers of carbon. In addition, the NFC
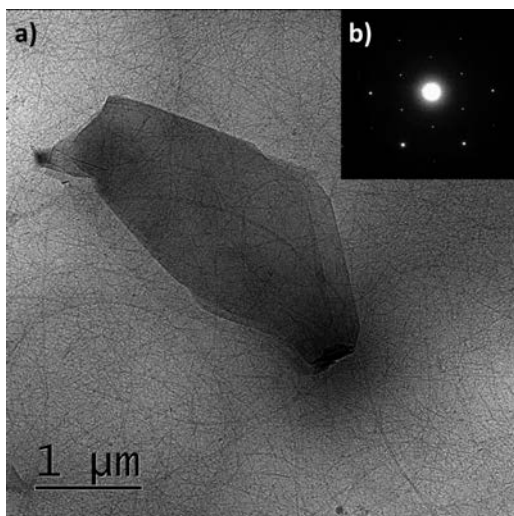
Figure 1. (a) Cryo-TEM image of exfoliated multilayered graphene flake embedded in NFC hydrogel. (b) Electron diffraction pattern of a typical multilayered graphene flake in a NFC matrix.

fibrils are spread homogeneously around the flakes, showing no aggregation due to the presence of the graphitic material. In Figure 1b, a typical electron diffraction pattern, showing the characteristics of a multilayered graphene is presented.

Characterization of NFC/Multilayered Graphene Nanocomposites. Solid composite materials from the aqueous suspensions containing different mass fractions of graphene were formed by removing water from suspensions by vacuum filtration. SEM images of the resulting nanocomposite

materials are presented in Figure 2a,b. A cross-sectional image of a nanocomposite containing 50 wt % of graphene is shown in Figure 2b, wherein platelets of multilayered graphene are observed. Figure 2a shows the cross-section of a pure NFC nanopaper, where homogeneous structure of NFC fibrils was observed. In Figure 2b, the composite containing multilayered graphene flakes, shows slightly rougher and more porous structure. The NFC fibrils standing out at one side of the NFC nanopaper are a result of the vacuum filtration. The translucency of the nanocomposite of 1.25 wt % of graphene is shown in Figure 2c, a colored pattern can be seen relatively clearly from beneath of an approximately 10 μm nanocomposite. Figure 2d exhibits the flexibility of the nanocomposite (1.25 wt % graphene) where tweezers were used to fold the nanocomposite without any visible damage or signs of defects.

The thickness and distribution of the graphene flakes were studied by mapping the composite surfaces by Raman microscopy (Figure 3). A random assembly of thin graphite and multilayered graphene flakes was observed. Raman spectra measured at several spots on the composite surface show the characteristic bands of crystalline graphite and graphene multilayers, verifying that graphite was indeed dispersed as thin flakes having lateral dimensions in the micrometer scale.[51] Examples of Raman maps of the graphite main bands measured from the surface are presented in Figure 3b,c. In Figure 3b, a map showing the intensity of the G band is presented, whereas Figure 3c shows the intensity of the D′ band at the same area. The maps show slightly different patterns, indicating differences in flake thickness along the studied region. Example spectra measured at selected spots are presented in Figure 3d. A Raman signal of cellulose near 1095 cm^{-1} was also observed.

Mechanical Properties of NFC/Multilayered Graphene Nanocomposites. Nanocomposites with different amounts of graphene were prepared and their mechanical properties were investigated in tensile mode to find the optimum combination
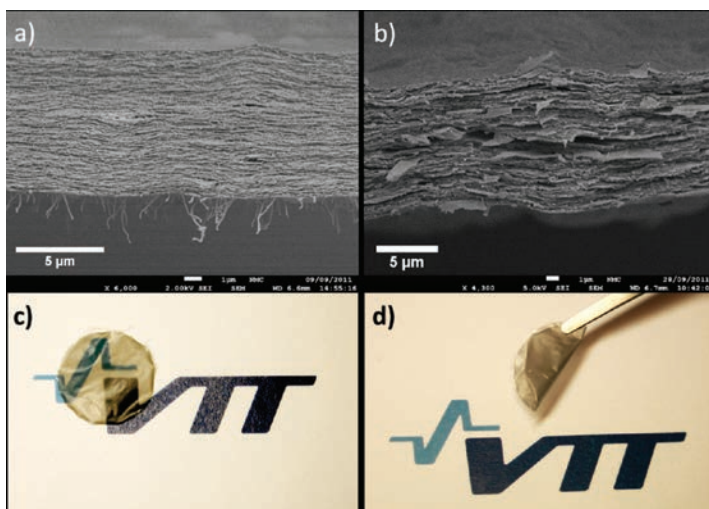

Figure 2. (a) Cross-sectional SEM image of a pure NFC-nanopaper film. (b) Cross-sectional SEM image of graphene/NFC nanocomposite with 50 wt % graphene multilayers. (c) Translucent 1.25 wt % graphene/NFC film on top of a colored pattern. (d) The flexibility of the 1.25 wt % of multilayered graphene nanocomposite shown by folding.
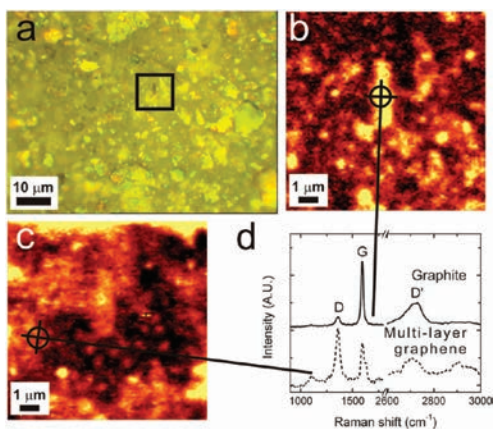
Figure 3. Optical and Raman microscopy images from surface of a film containing 10 wt % of graphene multilayers and NFC. (a) An optical image of the film surface showing flakes of different sizes and thicknesses. (b) Raman map from the highlighted 10 μm × 10 μm area where the intensity of the G band was integrated. (c) Raman map from the highlighted 10 μm × 10 μm area where the intensity of the D′ band was integrated. Raman spectra measured at indicated locations showing characteristic features of graphite (solid line) and a multilayered graphene (dotted line).

of NFC and multilayered graphene. The graphene content (weight percentage, wt %) is given in relation to the amount of NFC. The Young's modulus (Figure 4b), ultimate and yield tensile strength (Figure 4c,d), strain and toughness (Figure 4e,f) obtained from the stress−strain curves show that the optimal performance of the nanocomposite occurred when content of graphene multilayers was 1.25 wt %. At this composition, the properties go through a maximum and beyond this content they start to weaken. At contents of graphene of 5 wt % or more, the properties are even slightly poorer than of pure NFC paper.

Addition of 1.25 wt % of graphene multilayers to NFC results in a significant increase of modulus when compared to pure NFC paper: The measured Young's modulus for 1.25 wt % nanocomposite was 16.9 GPa, while pure NFC paper had a value of 11.2 GPa. Figure 4c,d show the measured ultimate tensile stress and yield stress. In both cases, similar trend as a function of the graphene content could be observed. The highest measured values were 351 MPa for the ultimate tensile strength and 107 MPa for the yield strength. Yield strength was determined from the point at the stress−strain curves where the slope drastically changes and is a measure of the strength that the material can take before plastic deformations start to occur. Changes in the ultimate tensile strength were more drastic than in the yield strength. Yield strength of the composites containing more than 5 wt % of graphene multilayers remained close to the value of pure NFC.

The strain values of the composites containing different amounts of graphene are presented in Figure 4e. The results show that the relative strain did not change much when the graphene content was increased and remained between 10 and 11%. Work-of-fracture, a measure of toughness, is shown for composites having different graphene content in Figure 4f. Again, the highest value was observed at the 1.25 wt % of

graphene multilayers, in which the work of fracture reaches 22.3 MJ m^{-3}.

■ DISCUSSION

By choosing sonication energy properly, NFC nanopaper with remarkably high mechanical performance was first obtained. The tensile strength and work-of-fracture of the pure NFC paper, 287 MPa and 18.9 MJ m^{-3}, respectively, as a combination were among the highest ever reported for nanopaper made from native NFC.[48] Cellulose nanopapers have been reported already before[21] showing tensile strength of 232 MPa and Young's modulus of 13.4 GPa.[29] Our results highlight the importance of optimized conditions for sonication to suppress aggregation to allow thorough fibrillation of NFC. However, the use of excessive mechanical homogenization should be avoided because the properties were clearly deteriorated when sonication was prolonged. Deterioration of the mechanical properties was probably a result of the shortening of fibrils under intensive sonication. The lowering of the degree of polymerization has been shown to significantly affect the mechanical properties of NFC nanopapers.[17,48,52]

We found that NFC hydrogels allow direct exfoliation of graphite without further surface active compounds when using an optimized sonication protocol. The thickness measured for the exfoliated flakes by cryo-TEM, SEM, and Raman microscopy varied from material characterized as bulk graphite to the range of multilayered graphene. Even though bulk graphite was observed by Raman microscopy (Figure 3b), a large fraction of the material embedded in the composite structures showed a relatively strong D′ band, which indicates a material thinner than bulk graphite (Figure 3c).[51] Because the graphene flakes most probably restacked during film formation and compression, localization and identification of single-layer graphene by Raman microscopy was not possible.

Direct ultrasound-assisted dispersion of graphite flakes into NFC matrix is an efficient method for the fabrication of stable and homogeneous dispersions of graphene multilayers in aqueous environment. At low contents, such as 1.25 wt %, the graphene flakes could not be observed from the cross-section of the nanocomposite materials by SEM. The process resulted in an efficient reinforcement of the cellulose nanopaper by a small amount of graphene multilayers. The optimum was observed to be as low as 1.25 wt % of graphene multilayers in a NFC matrix. At higher contents, a more uneven distribution of graphene within the composite structures was observed (Figure 2b), which might also play a role in the deterioration of the mechanical properties.

The combination of multilayered graphene and NFC in a nanocomposite resulted in a superior combination of stiffness (50% increase), toughness (work of fracture 18% increase), and strength (22% increase) compared to the corresponding pristine NFC nanopapers. These remarkable properties suggest that the mechanical strength of the composite is improved through interactions that are mediated by binding between graphene and NFC. This type of interaction has not been described before, but we suggest that our data indicate the existence of such interactions. It has been shown earlier that NFC has an amphiphilic nature, which might explain its behavior with hydrophobic graphene in aqueous environment.[53] Use of aqueous NFC hydrogel as dispersant for graphene flakes shows that these interactions occur also in aqueous environment suggesting that coassembly of graphene layers and NFC might be, at least partly, driven by hydrophobic
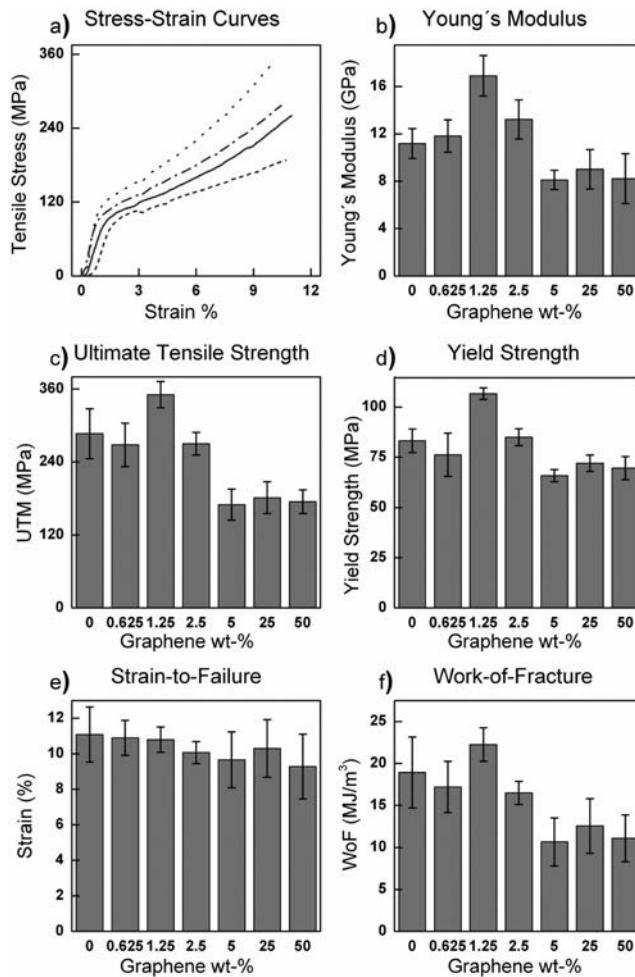
Figure 4. (a) Stress−strain curves of nanocomposites containing NFC and multilayered graphene. The dotted line represents the nanocomposite containing 1.25 wt % of graphene, the dash-dotted line represents the composite containing 2.5 wt % of graphene, the solid line represents pure NFC film and the dashed line represents the nanocomposite containing 25 wt % of graphene multilayers. (b) Young's modulus, (c) ultimate tensile strength, (d) yield strength, (e) strain-to-failure, and (f) work-of-fracture of nanocomposites containing NFC and different amounts of graphene multilayers in relation to the mass of NFC. The presented error bars were calculated from the standard deviation of parallel measurements.

interactions. We also suggest that the attachment of graphene and cellulose could be stabilized by π-interactions.[54] Stacking between π-electron systems and carbohydrates have been observed in several protein-carbohydrate interactions including those of binding domains of cellulose degrading enzymes being able to bind to the (110) crystalline face of cellulose I in the ultrasound.[55] Stacking of π-electrons and cellulose chains have also been observed in the binding of cellulose chains in hydrolytic enzymes.[56,57] This, and the large accessible area of both graphene and flexible nanocellulose fibrils, would explain the enhanced mechanical properties.

The composite had a promoted toughness, appearing especially as high strain-to-failure value even when the composite was stiffened by a significant amount of graphene. The high strain values are likely due to noncovalent bonding between multilayered graphene flakes and the NFC fibrils, allowing them to slide against each other also while NFC fibrils are allowed to slide against each other. During the sliding, the energy could be dissipated by regeneration of hydrogen bonds between NFC fibrils. The sliding of the long fibrils may also lead to their reorientation, which was observed as slight tensile stiffening (Figure 4a). Relative strain values, which were around 10−11% for all of the samples, can be considered as rather high values for composite materials having also high strength and stiffness, since often composite materials become brittle, when they turn stiffer and stronger. Thus, our nanocomposite highlights superior toughness in combination with high strength and stiffness and shows an example of synergistic composite properties.

We previously showed that a protein that binds to both graphene and cellulose could be used to mediate the binding between graphene flakes and NFC and thereby strengthen a nanocomposite material.[32] A comparison between the previous and the present work reveals that the different ways of allowing NFC and graphene interact resulted in materials with distinctly different properties. Most notably the protein aided binding between NFC and graphene flakes led to higher stiffness (20.2 GPa vs 16.9 GPa obtained here) but lower strain to failure (3.1% vs 11% obtained here), and thus lower toughness. The results are easily compared because the same type of NFC was used in both sets of experiments, thus the surface chemistry and surface area were similar, despite the changes in the ultra sound assisted treatment that may have had an effect on the fiber length. We note that using only multilayered graphene and cellulose resulted in a notable increase in stiffness and strength with a largely unaffected strain to failure. Using the protein gave a still markedly higher stiffness, but a clear decrease in strain to failure. The different ways of forming the nanocomposite thus result in very different characteristics in the materials. Apparently the protein is more efficient in forming cohesive binding and may also allow larger parts of the NFC to interact because of the flexible polypeptide linking region in the protein. However, the protein mediated binding seems to allow less flexibility as seen by the lower strain to failure of the protein based material.

CONCLUSIONS

We have shown that graphene multilayers can be directly exfoliated within aqueous hydrogels of native cellulose nanofibrils using sonication without any further additives. Aligned graphene multilayers/NFC nanocomposite assemblies with high modulus, high strength, and work-of-fracture can be achieved by removing water by filtration. The fabrication of the nanocomposite is simple, fast and consumes relatively little energy without production of harmful waste streams, thus it is scalable and supports green pathways. The nanocomposite is generally highly flexible and in the case of 1.25 wt % graphene content it is also partially transparent. An interaction between graphene and NFC is also suggested, showing a rather surprising compatibility of these nanomaterials and their efficient interplay.

AUTHOR INFORMATION

Corresponding Author
*E-mail: paivi.laaksonen@vtt.fi. Fax: +358 20 722 7071. Tel.: +358 20 722 4611.

Notes
The authors declare no competing financial interest.

ACKNOWLEDGMENTS

REFERENCES

(1) Meyers, M. A.; Chen, P.-Y.; Lin, A. Y.-M.; Seki, Y. *Prog. Mater. Sci.* **2008**, *53*, 1.
(2) Klemm, D.; Kramer, F.; Moritz, S.; Lindström, T.; Ankerfors, M.; Gray, D.; Dorris, A. *Angew. Chem., Int. Ed.* **2011**, *50*, 5438.
(3) Tang, Z.; Kotov, N. A.; Magonov, S.; Ozturk, B. *Nat. Mater.* **2003**, *2*, 413.
(4) Fratzl, P.; Burgert, I.; Gupta, H. S. *Phys. Chem. Chem. Phys.* **2004**, *6*, 5575.
(5) Deville, S.; Saiz, E.; Nalla, R. K.; Tomsia, A. P. *Science* **2006**, *311*, 515.
(6) Munch, E.; Launey, M. E.; Alsem, D. H.; Saiz, E.; Tomsia, A. P.; Ritchie, R. O. *Science* **2008**, *322*, 1516.
(7) Bonderer, L. J.; Studart, A. R.; Gauckler, L. J. *Science* **2008**, *319*, 1069.
(8) Bratzel, G. H.; Cranford, S. W.; Espinosa, H.; Buehler, M. J., *J. Mater. Chem.* **2010**, *20*, 10465−10474.
(9) Antonietti, M.; Fratzl, P. *Macromol. Chem. Physic.* **2010**, *211*, 166.
(10) Takai, O. *Ann. N.Y. Acad. Sci.* **2006**, *1093*, 84.
(11) Sarikaya, M. *Proc. Natl. Acad. Sci. U.S.A.* **1999**, *96*, 14183.
(12) Teeri, T. T.; Brumer, H. 3rd; Daniel, G.; Gatenholm, P. *Trends Biotechnol.* **2007**, *25*, 299.
(13) Andreadis, S. T.; Geer, D. J. *Trends Biotechnol.* **2006**, *24*, 331.
(14) Kowalczyk, S. W.; Blosser, T. R.; Dekker, C. *Trends Biotechnol.* **2011**, *29*, 607.
(15) Walther, A.; Bjurhager, I.; Malho, J.-M.; Pere, J.; Ruokolainen, J.; Berglund, L. A.; Ikkala, O. *Nano Lett.* **2010**, *10*, 2742.
(16) Turbak, A. F.; Snyder, F. W.; Sandberg, K. R. *J. Appl. Polym. Sci.* **1983**, *37*, 815.
(17) Herrick, F. W.; Casebier, R. L.; Hamilton, J. K.; Sandberg, K. R. *J. Appl. Polym. Sci.* **1983**, *37*, 797.
(18) Saito, T.; Kimura, S.; Nishiyama, Y.; Isogai, A. *Biomacromolecules* **2007**, *8*, 2485.
(19) Pääkkö, M.; Ankerfors, M.; Kosonen, H.; Nykänen, A.; Ahola, S.; Österberg, M.; Ruokolainen, J.; Laine, J.; Larsson, P. T.; Ikkala, O.; Lindström, T. *Biomacromolecules* **2007**, *8*, 1934.
(20) Henriksson, M.; Henriksson, G.; Berglund, L. A.; Lindström, T. *Eur. Polym. J.* **2007**, *43*, 3434.
(21) Berglund, L. A.; Peijs, T. *MRS Bull.* **2010**, *35*, 201.
(22) Nakagaito, A. N.; Yano, H. *Appl. Phys. A: Mater. Sci. Process.* **2004**, *78*, 547.
(23) Pääkkö, M.; Vapaavuori, J.; Silvennoinen, R.; Kosonen, H.; Ankerfors, M.; Lindström, T.; Berglund, L. A.; Ikkala, O., *Soft Matter* **2008**, *4*, 2492−2499.
(24) Korhonen, J. T.; Hiekkataipale, P.; Malm, J.; Karppinen, M.; Ikkala, O.; Ras, R. H. *ACS Nano* **2011**, *5*, 1967.
(25) Iwamoto, S.; Isogai, A.; Iwata, T. *Biomacromolecules* **2011**, *12*, 831.
(26) Walther, A.; Timonen, J. V. I; Díez, I.; Laukkanen, A.; Ikkala, O. *Adv. Mater.* **2011**, No. 23, 2924.
(27) Yano, H.; Sugiyama, J.; Nakagaito, A. N.; Nogi, M.; Matsuura, T.; Hikita, M.; Handa, K. *Adv. Mater. (Weinheim, Ger.)* **2005**, *17*, 153.
(28) Nakagaito, A. N.; Yano, H. *Appl. Phys. A: Mater. Sci. Process.* **2005**, *80*, 155.
(29) Sehaqui, H.; Liu, A.; Zhou, Q.; Berglund, L. A. *Biomacromolecules* **2010**, *11*, 2195.
(30) Wang, M.; Olszewska, A.; Walther, A.; Malho, J. M.; Schacher, F. H.; Ruokolainen, J.; Ankerfors, M.; Laine, J.; Berglund, L. A.; Osterberg, M.; Ikkala, O. *Biomacromolecules* **2011**, *12*, 2074.
(31) Czaja, W. K.; Young, D. J.; Kawecki, M.; Brown, R. M. Jr. *Biomacromolecules* **2007**, *8*, 1.
(32) Laaksonen, P.; Walther, A.; Malho, J. M.; Kainlauri, M.; Ikkala, O.; Linder, M. B. *Angew. Chem., Int. Ed.* **2011**, *50*, 8688.
(33) Novoselov, K. S.; Geim, A. K.; Morozov, S. V.; Jiang, D.; Zhang, Y.; Dubonos, S. V.; Grigorieva, I. V.; Firsov, A. A. *Science* **2004**, *306*, 666.
(34) Stankovich, S.; Dikin, D. A.; Dommett, G. H.; Kohlhaas, K. M.; Zimney, E. J.; Stach, E. A.; Piner, R. D.; Nguyen, S. T.; Ruoff, R. S. *Nature* **2006**, *442*, 282.
(35) Geim, A. K.; Novoselov, K. S. *Nat. Mater.* **2007**, *6*, 183.
(36) Novoselov, K. S.; Jiang, D.; Schedin, F.; Booth, T. J.; Khotkevich, V. V.; Morozov, S. V.; Geim, A. K. *Proc. Natl. Acad. Sci. U.S.A.* **2005**, *102*, 10451.

(37) Berger, C.; Song, Z.; Li, X.; Wu, X.; Brown, N.; Naud, C.; Mayou, D.; Li, T.; Hass, J.; Marchenkov, A. N.; Conrad, E. H.; First, P. N.; De Heer, W. A. *Science* **2006**, *312*, 1191.

(38) Kim, K. S.; Zhao, Y.; Jang, H.; Lee, S. Y.; Kim, J. M.; Ahn, J. H.; Kim, P.; Choi, J. Y.; Hong, B. H. *Nature* **2009**, *457*, 706.

(39) Viculis, L. M.; Mack, J. J.; Kaner, R. B. *Science* **2003**, *299*, 1361.

(40) Chen, G.; Weng, W.; Wu, D.; Wu, C.; Lu, J.; Wang, P.; Chen, X. *Carbon* **2004**, *42*, 753.

(41) Li, X.; Wang, X.; Zhang, L.; Lee, S.; Dai, H. *Science* **2008**, *319*, 1229.

(42) Hernandez, Y.; Nicolosi, V.; Lotya, M.; Blighe, F. M.; Sun, Z.; De, S.; Mcgovern, I. T.; Holland, B.; Byrne, M.; Gun'ko, Y. K.; Boland, J. J.; Niraj, P.; Duesberg, G.; Krishnamurthy, S.; Goodhue, R.; Hutchison, J.; Scardaci, V.; Ferrari, A. C.; Coleman, J. N. *Nat. Nanotechnol.* **2008**, *3*, 563.

(43) Kim, H.; Abdala, A. A.; Macosko, C. W. *Macromolecules* **2010**, *43*, 6515.

(44) Li, D.; Kaner, R. B. *Science* **2008**, *320*, 1170.

(45) Kim, H.; Miura, Y.; Macosko, C. W. *Chem. Mater.* **2010**, *22*, 3441.

(46) Laaksonen, P.; Kainlauri, M.; Laaksonen, T.; Shchepetov, A.; Jiang, H.; Ahopelto, J.; Linder, M. B. *Angew. Chem., Int. Ed.* **2010**, *49*, 4946.

(47) Linder, M. B.; Szilvay, G. R.; Nakari-Setälä, T.; Penttilä, M. E. *FEMS Microbiol. Rev.* **2005**, *29*, 877.

(48) Henriksson, M.; Berglund, L. A.; Isaksson, P.; Lindstrom, T.; Nishino, T. *Biomacromolecules* **2008**, *9*, 1579.

(49) Jalal Uddin, A.; Araki, J.; Gotoh, Y. *Biomacromolecules* **2011**, *12*, 617.

(50) Zhbankov, R. G.; Firsov, S. P.; Grinshpan, D. D.; Baran, J.; Marchewka, M. K.; Ratajczak, H. *J. Mol. Struct.* **2003**, *645*, 9.

(51) Ferrari, A. C.; Meyer, J. C.; Scardaci, V.; Casiraghi, C.; Lazzeri, M.; Mauri, F.; Piscanec, S.; Jiang, D.; Novoselov, K. S.; Roth, S.; Geim, A. K. *Phys. Rev. Lett.* **2006**, *97*, 187401/1.

(52) Iwamoto, S.; Abe, K.; Yano, H. *Biomacromolecules* **2008**, *9*, 1022.

(53) Johansson, L.-S.; Tammelin, T.; Campbell, J. M.; Setala, H.; Osterberg, M., *Soft Matter* **2011**, *7*, 10917−10924.

(54) Quiocho, F. A. *Biochem. Soc. Trans.* **1993**, *21*, 442.

(55) Lehtiö, J.; Sugiyama, J.; Gustavsson, M.; Fransson, L.; Linder, M.; Teeri, T. T. *Proc. Natl. Acad. Sci. U.S.A.* **2003**, *100*, 484.

(56) Nand, K, V. *Curr. Opin. Struct. Biol.* **1991**, *1*, 732.

(57) Divne, C.; Ståhlberg, J.; Teeri, T. T.; Jones, T. A. *J. Mol. Biol.* **1998**, *275*, 309.

IV/7

Title	**Bioinspired materials**
	Non-covalent modification of nanofibrillated cellulose and chitin via genetically engineered proteins and multilayered graphene
Author(s)	Jani-Markus Malho
Abstract	Biological nanocomposites such as nacre, bone and wood synergistically combine strength, stiffness and toughness with lightweight structure, whereas most man-made engineering materials with higher densities follow the rule-of-mixtures, according to which strength and toughness are mutually exclusive properties. Biomimetic approaches study and mimic nature's concepts and material structures with the aim of developing high-performance bioinspired materials. Recent studies have shown that many of the properties of natural nanocomposites arise from their hierarchical structures from multiple length scales. Molecular level control and design are known to be crucial for the performance of the natural materials especially at the interfaces of the softer matrix and the harder reinforcing elements. In this work, examples of biopolymer matrices were studied from the mechanical perspective in order to understand how biological components, such as genetically engineered proteins and graphene flakes, could be used to design an organic matrix at the molecular level and to control its macroscopic material properties. The results indicated that the biopolymer networks can be functionalized non-covalently in aqueous and mild conditions directly via self-assembly in order to influence the mechanical properties. In publications I and II, genetically engineered fusion proteins, incorporating hydrophobin - double cellulose binding domain or plain double cellulose binding domain, were used to tune the nanofibrillar cellulose network under conditions of controlled humidity. In publication III, another genetically engineered fusion protein, chitin binding domain - aspein, was used to modify nanofibrillated chitin matrix through ionic interactions and biomimetic mineralization of calcium carbonate. In publication IV, multilayered graphene flakes were exfoliated directly into native nanofibrillated cellulose networks in order to create nanocomposites with improved mechanical properties. Non-covalent modification of the colloidal biopolymer matrices is an efficient route to construct and study multifunctional nanocomposite materials by engineering the interfaces between the soft and hard phases. Importantly, genetically engineered proteins could pave the way towards new functional components for biomimetic structural nanocomposite materials while Nature's materials continue to provide the constructing principles and inspiration for the development of biomimetic materials.
ISBN, ISSN	
Date	April 2015
Language	English, Finnish abstract
Pages	72 p. + app. 53 p.
Name of the project	
Commissioned by	
Keywords	self-assembly, biopolymer, biomimetics, nanocomposite, genetically engineered proteins, graphene, materials science, colloids
Publisher	VTT Technical Research Centre of Finland Ltd P.O. Box 1000, FI-02044 VTT, Finland, Tel. 020 722 111

Nimeke	**Bioinspiroidut materiaalit** Nanofibrilloidun selluloosan ja kiitinin ei-kovalenttinen muokkaus käyttäen hyväksi geneettisesti luotuja proteiineja sekä monikerroksista grafeiinia
Tekijä(t)	Jani-Markus Malho
Tiivistelmä	Luonnon nanokomposiittimateriaalit, kuten helmiäissimpukan kuori, luu ja puu, omaavat synergisiä mekaanisia ominaisuuksia, joissa yhdistyvät jäykkyys, vahvuus ja sitkeys kevyessä rakenteessa. Suurin osa ihmisen tekemistä synteettisistä materiaaleista noudattaa "rule-of-mixtures"-sääntöä, jossa jäykkyys ja sitkeys ovat toisen pois sulkevia ominaisuuksia. Biomimeettiset lähestymistavat tutkivat ja pyrkivät jäljittelemään luonnon luomia konsepteja ja materiaalirakenteita tavoitteena kehittää uusia biomimeettisia ja parempia ominaisuuksia omaavia materiaaleja. Viime vuosien tutkimukset ovat osoittaneet, että monet toivottavat materiaaliominaisuudet perustuvat useiden eri kokoluokkien yli ulottuviin itsejärjestäytyneisiin hierarkkisiin rakenteisiin. Molekyylirakennetason suunnittelun ja hallinnan tiedetään olevan erityisen tärkeää luonnon nanokomposiittimateriaalien rajapinnoilla, joissa pehmeämpi matriisi yhdistyy jäykempien vahvistavien rakenteiden kanssa. Tässä työssä tutkittiin, kuinka biopolymeerimatriiseja voidaan suunnitella ja muokata molekyylitasolla käyttäen hyväksi geneettisesti luotuja proteiineja sekä grafeiinihiutaleita. Tavoitteena on makroskooppisten mekaanisten ominaisuuksien molekyylitason hallinta. Tulokset osoittavat, että biopolymeeriverkostoja voidaan funktionalisoida ei-kovalenttisesti miedoissa vesipohjaisissa ympäristöissä mekaanisiin ominaisuuksiin vaikuttaen. Julkaisuissa I ja II käytettiin geneettisesti luotuja fuusioproteiineja. Fuusioproteiinit muodostuivat joko hydrofobiinista yhdistettynä kaksinkertaiseen selluloosasitoutumisdomeeniin tai pelkästä kaksinkertaisesta selluloosasitoutumisdomeenista. Fuusioproteiineilla muokattiin nanofibrilloituja selluloosan verkostoja eri kosteustiloissa. Julkaisussa III muokattiin nanofibrilloitua kitiiniverkostoa ei-kovalenttisesti geneettisesti luodun fuusioproteiinin avulla. Kyseinen proteiini sisälsi kitiinisitoutumisdomeenin ja aspeiinin, joka mahdollisti ionisten vuorovaikutusten hyödyntämisen sekä kalsiumkarbonaatin kiteyttämisen. Julkaisussa IV kuorittiin monikerroksisia grafeiinihiutaleita suoraan nanofibrilloituun selluloosamatriisiin, josta valmistetuilla nanokomposiittimateriaaleilla oli parannettuja mekaanisia ominaisuuksia. Ei-kovalenttinen ja kolloidaalinen biopolymeerimatriisien modifiointi on tehokas menetelmä tutkia ja luoda uusia monitoiminnallisia nanokomposiittimateriaaleja muokkaamalla pehmeiden ja vahvistavien rakenteiden rajapintoja. Geneettisesti muokattuja proteiineja voidaan pitää lupaavina toiminnallisina komponentteina tulevaisuuden biomimeettisiin ja rakenteellisiin materiaaleihin. Luonnon materiaalit ja systeemit tulevat jatkossakin toimimaan inspiraation lähteenä sekä tarjoamaan toimintaperiaatteita uusien biomimeettisten materiaalien luomiseen.
ISBN, ISSN	ISBN 978-951-38-8233-4 (nid.) ISBN 978-951-38-8234-1 (URL: http://www.vtt.fi/publications/index.jsp) ISSN-L 2242-119X ISSN 2242-119X (Painettu) ISSN 2242-1203 (Verkkojulkaisu)
Julkaisuaika	Huhtikuu 2015
Kieli	Englanti, suomenkielinen tiivistelmä
Sivumäärä	72 s. + liitt. 53 s.
Projektin nimi	
Rahoittajat	
Avainsanat	itsejärjestyminen, biopolymeeri, biomimetiikka, nanokomposiitti, geneettisesti luodut proteiinit, grafeeni, materiaalitiede, kolloidit
Julkaisija	Teknologian tutkimuskeskus VTT Oy PL 1000, 02044 VTT, puh. 020 722 111

Bioinspired materials
Non-covalent modification of nanofibrillated cellulose and chitin via genetically engineered proteins and multilayered graphene

VTT SCIENCE 81

Bioinspired materials